Structural and Chemical Characterizations of Mo–Ti Mixed Oxide Layers

D I S S E R T A T I O N

zur Erlangung des akademischen Grades

doctor rerum naturalium
Dr. Rer. Nat.
im Fach Chemie

eingereicht an der
Mathematisch-Naturwissenschaftlichen Fakultät I
Humboldt-Universität zu Berlin

von
Osman Karslıoğlu M.S.

Präsident der Humboldt-Universität zu Berlin:
Prof. Dr. Jan-Hendrik Olbertz

Dekan der Mathematisch-Naturwissenschaftlichen Fakultät I:
Prof. Stefan Hecht, Ph.D.

Gutachter:
1. Prof. Dr. Hans-Joachim Freund
2. Prof. Dr. Klaus Rademann
3. Prof. Dr. Hans Börner
4. Prof. Dr. Erhard Kemnitz
5. Prof. Dr. Michael Linscheid

eingereicht am: 28.3.2013
Tag der mündlichen Prüfung: 26.6.2013

to my father

Acknowledgements

The four years, during which this work has been pursued, has become the most special part of my life in many respects. This page is the best I can do to express my gratitude to those who will always be remembered.

I'm of course indebted to Prof. Hans-Joachim Freund for giving me the opportunity to be a part of the world's one of the most prestigious scientific institutions. I'm also grateful to Prof. Klaus Rademann for supervising the thesis at the Humboldt University. They have always been very kind and supportive in a way that I truly appreciate.

Dr. Helmut Kuhlenbeck has been the person who mentored me and guided this work on a daily basis. Countless times he presented me new perspectives (a physicist's perspectives) on my data. I not only benefited immensely from his invaluable knowledge but also learned from him how proper science should be done. Management of the lab has been so smooth thanks to his approachable character (which, of course, has manifested itself with his unforgettable jokes).

Matthias Naschitzki has provided valuable technical assistance for the equipment. I have learned so much from him about UHV. He has been dedicated to his job to an extent that I have never witnessed before. To him, my appreciation and respect know no bounds.

In nontechnical matters, be it about administrative issues or private problems, Manuella Misch and Gabi Mehnert have provided prompt and effective assistance with great courtesy. They both deserve my humble appreciation.

Among the early stages of the project, I had the pleasure of working with Dr. Anastassia Pavlovska and Dr. Daniel Göbke. Daniel was the one who introduced the equipment to me and helped me with my baby steps into the world of UHV. He has not only been a helpful colleague but also a great friend. Dr. Pavlovska has always had an inexhaustible motivation for science which is truly rare. My scientific discussions with her taught me a lot and our private conversations became moments of joy during our time together.

I have met so many wonderful friends at the Fritz Haber Institute. Each of them deserves my sincere gratitude for their friendships which were essential for me. Anibal Boscoboinic, Rhys Dowler, John Uhlrich, Elena Primorac, Hengshan Qiu, Ashi Savara, Bo-Hong Liu, Emre Emmez, Leonid Lichtenstein, Yuichi Fujimori, Alessandro Sala, Matthias Peter, Huifeng Wang, Christin Büchner, Bill Kaden, Xin Song, Felix Feiten, Steffi Stuckenholz, and the list goes on and on. Those that are named and those that are not, each one of them has been nothing less than a honest, helpful, friendly fellow. I sincerely apologise from those that I didn't mention, yet I'm sure they know that they are valued.

I have also met some wonderful Turks outside the institute's social sphere. My small Türkiye has been a family to me in Berlin. It would not be the same without them. I present my heartfelt appreciation to Özlem, Şafak, Erol, Ümit, Agne, Seda, Deniz, Özkan and Nuray for their beautiful friendships.

For the first time in my life, I have been away from my family for such a long time. Their endless love and support has made me achieve what I have today. It is impossible for a man like me, incompetent in expressing his true feelings, explain how important they are to me. “Anne, Ozan ve sevgilim Aydan, her şey için teşekkürler”.

In my last year, I went through the most disconsolate state of my life. My father passed away at the age of 61. His loss taught me how deep sorrow can penetrate and what the love of the family actually is. It was a bitter lesson that was unwillingly taken. I offer my sincerest gratitude to all those who has been there for me and my family. This thesis is dedicated to the man who left me a moral legacy of utmost value, to my father.

Abstract

Heterogeneous catalysts are materials with a high degree of complexity. Studies of these complex materials have been performed for many decades. The use of model systems with reduced complexity has been an important part of this endeavour. The simplest materials which have the capability of mimicking the function of a catalyst are single crystals and ordered layers which can be grown on single crystals. These systems can be studied under UHV conditions where many spectroscopic techniques are applicable and the structure and cleanliness of surfaces can be controlled to a great extent. In this work, this approach has been taken to study a mixed oxide system, namely Mo–Ti mixed oxides.

The work focuses on the preparation of thin oxide layers that contain Mo and Ti. Although the aim was to achieve mixing on the atomic scale, the term "mixed oxide" is used in the text in a more general sense where Ti and Mo coexist in one or more oxide phases. Different preparation procedures were employed in the study and these are presented in six categories.

The layers were prepared on TiO_2(110) single crystals by evaporating the metals in an O_2 atmosphere or in UHV and post treating the deposited material. When Mo and Ti were co-deposited in O_2, most of the molybdenum stayed at the surface with only a small Mo concentration in deeper layers. Mixing of Mo into TiO_2 was very limited, consistent with the phase diagram of MoO_2 and TiO_2. Mo^{6+} and Mo^{4+} were the dominant oxidation states in most of the layers and Mo^{6+} was always nearer to the surface than Mo^{4+}. Layers where Mo was completely mixed into TiO_2 could be prepared by depositing metals in UHV and post-oxidizing the deposited material. Inside the TiO_2 lattice, Mo had an oxidation state of 4+. Depositing Mo in O_2 at room temperature and post annealing in UHV led to the formation of two types of features in the STM images. These features were stable in UHV up to at least 1000 K. The layers with high Mo concentrations appeared patchy in the STM images but they still exhibited the TiO_2(110)–(1×1) LEED pattern.

The increase in Mo concentration led to the blocking of the bridging oxygen vacancies (BOVs) as evidenced by STM and water TPD. The reactivities of the layers were tested by methanol and ethanol TPD. An unprecedented high temperature (∼650 K) formaldehyde/methane formation channel was observed in the methanol TPD of clean TiO_2(110) and was associated with BOVs. The increase in the Mo concentration led to the vanishing of this channel as well as the ethylene formation channel (∼600 K) in the case of ethanol TPD. In both ethanol and methanol TPD, new reaction channels towards ethylene and methane formation at ∼500 K appeared.

Zusammenfassung

Heterogene Katalysatoren sind Materialien mit hoher Komplexität. Studien dieser komplexen Materialien werden seit Jahrzehnten durchgeführt. Die Verwendung von Modellsystemen mit reduzierter Komplexität ist ein wichtiger Teil dieser Bemühungen. Die einfachsten Materialien zur Modellierung eines Katalysators sind Einkristalle und geordnete Schichten, die auf Einkristallen aufgebracht werden können. Diese Systeme können im UHV untersucht werden, wo viele spektroskopische Techniken anwendbar sind und die Struktur und Reinheit der Oberflächen kann in hohem Maße gesteuert werden. In dieser Arbeit wurde dieser Ansatz gewählt um ein Mischoxid-System, nämlich die Mo–Ti Mischoxide studieren.

Die Arbeit konzentriert sich auf die Herstellung von dünnen Oxidschichten, welche Mo und Ti enthalten. Obwohl das Ziel eine Mischung auf der atomaren Skala war, wird der Begriff "Mischoxid" im Text im allgemeineren Sinn vervendet, da Ti und Mo in einem oder mehreren Oxid Phasen koexistieren. Verschiedene Präparationen wurden in der Studie untersucht und diese werden in sechs Kategorien dargestellt.

Die Schichten wurden auf TiO_2(110) Einkristallen durch Verdampfen der Metalle in einer O_2 Atmosphäre und in UHV und Nachbehandlung der Filme vorbereitet. Wenn Mo und Ti in O_2 gemeinsam aufgedampft wurden, wurde das meiste Mo an der Oberfläche abgeschieden mit einer nur geringen Mo-Konzentration in tieferen Schichten. Eine Mischung von Mo in TiO_2 war sehr begrenzt, und die stimmt mit dem Phasendiagramm MoO_2 und TiO_2 überein. Mo^{6+} und Mo^{4+} sind die dominierenden Oxidationsstufen in den meisten der Schichten, wobei Mo^{6+} stets näher an der Oberfläche war als Mo^{4+}. Schichten, in denen Mo vollständig in TiO_2 gelöst ist, konnten durch Abscheidung von Metallen in UHV und Post-Oxidation der Filme erstellt werden. Im Inneren des TiO_2 Gitters hat Mo die Oxidationsstufe 4+. Aufdampfen von Mo in O_2 bei Raumtemperatur und anschließendes Tempern in UHV führte zur Bildung zweier Arten von Merkmalen in den STM-Bildern. Diese waren im UHV stabil bis mindestens 1000 K. Die Schichten mit hoher Mo-Konzentrationen erschienen uneinheitlich in den STM-Bildern aber sie zeigte das TiO_2(110)–(1×1) LEED-Muster.

Der Anstieg in der Mo-Konzentration führte zur Blockierung der Überbrückung Sauerstoffleerstellen (BOVs), was durch STM und Wasser-TPD nachgewiesen wurde. Die Reaktivitäten der Schichten wurden mit Methanol- und Ethanol-TPD getestet. Eine unerwartete Formaldehyd/Methanbildung bei hohen Temperaturen (∼650 K) wurde bei der Methanol-TPD von reinem TiO_2(110) beobachtet und mit BOVs in Verbindung gebracht. Der Anstieg der Mo-Konzentration unterdrückte diesen Effekt sowie die Ethylenbildung (∼600 K) beim Durchführen von Ethanol-TPD. Sowohl in Ethanol als auch Methanol-TPD wurden neue Reaktionswege zu Ethylen und Methan-Bildung bei ∼500 K beobachtet.

Contents

1 INTRODUCTION

Industrial catalysis is key to the standard of living that we take for granted in today's world. Many essential commodities such as fertilizers, plastics, pharmaceuticals and clean liquid fuels are produced via catalytic processes. An example is the synthesis of ammonia which has colossal importance due to the fact that the population of the world today can not be sustained without the use of synthetic fertilizers. The value of all the chemicals produced by catalytic reactions annually is estimated to be US$ 2–4 trillion [1]. Catalysis continues to be an attractive area of research despite the great progress that was made in the last century.

Catalysts can be classified into two main categories: homogeneous and heterogeneous catalysts. Catalysts that are in a separate phase (generally solid) from the reactants are termed "heterogeneous" whereas catalysts that are in the same phase with the reactants are termed "homogeneous" catalysts. In many industrial processes, heterogeneous catalysts—such as the iron based catalysts that are used for ammonia synthesis—are preferred over homogeneous catalysts due to the technically demanding and costly separation processes associated with the latter. Heterogeneous catalysts may be in different forms, like a bulk material (e.g. Pt gauze for ammonia oxidation [2]) or a finely dispersed active material on a porous solid (e.g. Pt/Al_2O_3 for naphta reforming [3]). Catalysts of the latter type are called "supported" catalysts and they usually have complex chemical compositions. The two most common components of supported catalysts are metals and metal oxides.

Oxides are generally stable compounds which can be produced in a form that possesses a high surface area. This makes them appealing as catalyst "support" since the active phase has to be dispersed on such a material in order to increase its contact surface with the reactants. The stability of oxides is also an advantage, given the harsh conditions present in industrial reactors—e.g. high temperature, high pressure, corrosive chemicals. However, they are not only important as supports, but also as active phases. Oxides are used as catalysts in a number of industrial processes such as selective oxidation and oxidative dehydrogenation of organic compounds [4–6].

Almost all the heterogeneous catalysts contain some kind of modifier that increases their activity, selectivity and/or stability. The ability to fine tune a catalyst provides great potential for controlling these properties. Modifying oxide catalysts by doping is one of the ways to achieve fine tuning. Doping means introducing a small amount of foreign atoms (dopant) into the matrix of the main component (host). This kind of mixing can in principle lead to significant changes in the catalytic properties with a small change in the composition—these changes are preferred to be desirable changes, but nevertheless they may as well turn out to be otherwise. As a result, understanding the effect of doping on the catalytic properties of oxides is a challenge worthwhile to be undertaken. In recent years, theoretical works on the catalytic properties of doped oxides have appeared in the

literature [7–11]. Metiu and co-workers have performed systematic studies on doped oxides using DFT calculations and also compiled results from similar studies in the literature [10, 12, 13]. The model systems that they investigated were oxides with a dopant metal atom substituting a metal atom from the surface layer of the "host" oxide. The findings were explained using the concept of Lewis acidity–basicity. In the case of low-valence doping (LVD) where the dopant atom has a lower valence than the metal atom of the host oxide, lowering of oxygen vacancy formation energies was observed for all the systems that were investigated [12]. The ease of oxygen vacancy formation is critical for the reactions that proceed via a Mars–van Krevelen type mechanism, where a lattice oxygen atom is used up to oxidize a reactant molecule and the vacancy is replenished by an oxidant (O_2, NO, etc.) from the reactant mixture. The optimum catalyst would be one for which the vacancy formation is neither too "easy" nor too "hard". This type of "fine-tuning" can in principle be accomplished by changing the dopant type, adding other dopants, and varying dopant concentrations. Low-valence doped oxides were also found to be promising for methane activation. The dissociative adsorption of methane is energetically more favourable and the activation barrier of the C–H bond breaking step is lower for LVD oxides as compared to undoped oxides [12]. Activation of methane is a topic that is closely related to the global energy economy since utilizing the cheap natural gas, which is mainly composed of methane, to produce liquid fuels or valuable chemicals is extremely rewarding economically. The processes that convert methane to such products would be much simpler and economic if robust heterogeneous catalysts—such as oxides—are used, and doping may provide a means to achieve the desired activity and possibly selectivity for these catalysts. High-valance dopants (HVD) create different effects when they are added to reducible and non-reducible oxides. The extra electron(s) may be transferred to the host metal ion in the case of reducible oxides, which makes the situation more complex. This is not possible for non-reducible oxides. The addition of a HVD makes the system basic in any case. If the oxide becomes too basic, under reaction conditions it may bind one or more oxygen atoms and become acidic. The dopant is then not a metal atom (M) but a metal oxide moiety (MO or MO_2). These dopants are LVDs and alter the chemical properties accordingly.

All the aforementioned studies assume that the dopant atom is in the surface layer, which makes the direct interaction between the dopant and the gas phase possible. A recent study by Andersin et al. investigated an HVD system (Mo doped CaO) using DFT calculations and reached the conclusion that the redox reaction between the dopant and the adsorbate is the major contribution to the adsorption energy of a Lewis acid (i.e. a Au atom in that case) on the surface. This suggests that the dopant does not have to be in the surface layer in order to affect catalytic properties. A theoretical work which implicitly supports this view was published by Garcia-Mota et al. [8]. They investigated the effect of transition-metal doping on the electrochemical properties of the rutile–TiO_2(110) surface. Some dopants, such as Mo, prefer to occupy a substitutional site in the layer below the surface layer and yet they lower the overpotential required for the oxygen evolution reaction.

It is clear that quantum chemical calculations are useful for predicting the effect of doping on the catalytic properties of oxides and finding some guiding principles for catalyst

design. It goes without saying that the predictions made by using theory must be checked experimentally. However, experiments investigating the effects of doping are not always straightforward. A preparation of a mixture of two (or more) metal oxides may not always produce a homogeneous mixture. Small amounts of unmixed dopant on the surface can also change the catalytic properties. It is not easy to prove whether the two components are mixed completely and homogeneously or whether they are mixed partially and the unmixed dopant is dispersed on the surface of the doped host. Disentangling different effects may be easier if simple model systems are used for the investigation of doped oxides.

Working with model catalysts has many advantages over working with real catalysts. The model catalysts that are specifically meant in this context are single-crystalline metals/oxides and epitaxial layers prepared on top of single crystals. These systems have well defined surfaces which can be modified relatively easily in terms of structure and composition. The investigations of such model surfaces are mostly carried out by keeping the samples in ultra-high vacuum (UHV), which ensures surface cleanliness and makes the use of several surface science techniques possible. Scanning probe microscopy techniques are particularly useful since they provide real-space information at an atomic scale.

Taking a model catalyst approach for studying doped oxides is promising. In the Chemical Physics Department of the Fritz Haber Institute, where this thesis work has been pursued, some doped oxides have already been studied with a focus on their physical, rather than chemical properties [14–19]. An example is the preparation of Au nano-particles on doped CaO layers [16]. It was shown that doping CaO with Mo led to a change in the morphology of the Au particles. Au islands became flat (i.e. "wetted" the surface) on the doped CaO layer in contrast to the 3-dimensional structures that they had on the undoped CaO layer. Charge transfer from the Mo atoms to the Au particles was identified as the underlying mechanism of the phenomenon.

In this study the system under investigation is Mo containing TiO_2—more precisely the rutile phase of TiO_2. Mo and Ti oxides are components of several catalysts some of which are industrially important—these are mentioned explicitly in a following chapter. An important property of the oxides of these two metals is that they are reducible, meaning that the metal ions can have different oxidation states. Although this makes the system potentially more complicated than any combination of two non-reducible oxides, it also makes it catalytically more promising.

In this work, ultra-thin layers of mixed oxides were prepared on a rutile–TiO_2(110) substrate. The using of this substrate provided two advantages. Firstly, the layers had a good lattice match with the substrate, eliminating any complications that could have resulted from lattice strain such as structural defects. Secondly, the vast literature on the surface science of TiO_2(110) became available for interpreting the results. The simplest possible approach was taken for the preparation of the layers. Ti and Mo were evaporated from pure metals. The evaporations were carried out either in UHV conditions or in an O_2 atmosphere with a pressure in the range of 10^{-8}–10^{-6} mbar. Post-annealing treatments were applied in the final stages of the preparations. Complete mixing, which is required for doping, was difficult and could not be obtained in most of the cases. Consequently, a

more general investigation of different mixed systems containing Mo and Ti was pursued. In future studies, the prepared layers can be used as model systems for TiO_2 supported MoO_x catalysts as well as Mo-doped TiO_2 catalysts.

The rest of this thesis has been structured in the following way. In the second chapter, an overview of the experimental setup is given, explaining the UHV setup, apparatuses, sample holder design and substrate. The theoretical background of the employed techniques is also presented in this chapter. In the third chapter, the focus is on the properties of materials that are relevant for this work. These are TiO_2, MoO_2 and MoO_3. The properties of rutile–TiO_2(110) are covered in length. A section is devoted to the MoO_2–TiO_2 binary system. The results of the structural characterizations are presented in the fourth chapter. After an overview of the different procedures that were used to prepare mixed layers, each procedure and the associated results are presented in a separate section. The fifth chapter is on the reactivities of the prepared surfaces, which have been studied mostly via temperature-programmed desorption experiments using water, methanol and ethanol as the probe molecules.

2 EXPERIMENTAL

The experimental work that is presented in this thesis was carried out, almost exclusively, with a commercial UHV instrument, manufactured by Omicron NanoTechnology GmbH. A small part of the work was carried out at the UE52–PGM beamline of the BESSY II electron storage ring in Berlin. The aim of this chapter is to introduce the experimental setup and present the basic principles of the employed techniques.

2.1 The Experimental Setup — Overview

The setup is a UHV chamber with the following instruments/parts:

- A room temperature scanning tunnelling microscope (RT–STM), which is used for imaging surface structures.
- An x-ray gun and an electron energy analyser for x-ray photoelectron spectroscopy (XPS), which is used for chemical analysis of the surface.
- A low-energy electron diffraction (LEED) apparatus, which is used for identifying the degree of surface crystallinity and measuring the periodicity of ordered surface structures.
- A quadruple mass spectrometer (QMS), which is used for temperature-programmed desorption (TPD) experiments, monitoring concentrations of residual gases and detection of leaks through connections.
- A sample manipulator with xyz translation and axial rotation capability, equipped with a tungsten filament for electron-beam heating of the sample, and a copper block (that can be cooled with flowing gaseous or liquid nitrogen) as a thermal reservoir.
- Two commercial electron-beam evaporators (Focus–EFM 3), which are used for preparation of the oxide films that are to be investigated.
- A high-pressure cell, which is used for sample treatment at high pressures and high temperatures, as well as an intermediate chamber for transferring samples and STM tips in and out.
- A quartz-crystal microbalance that is integrated into the copper thermal reservoir of the manipulator, which is used for calibration of the metal deposition rates .
- A sputter gun, which is used for cleaning the sample surface (and occasionally STM tips) by shooting a high-energy argon-ion beam.

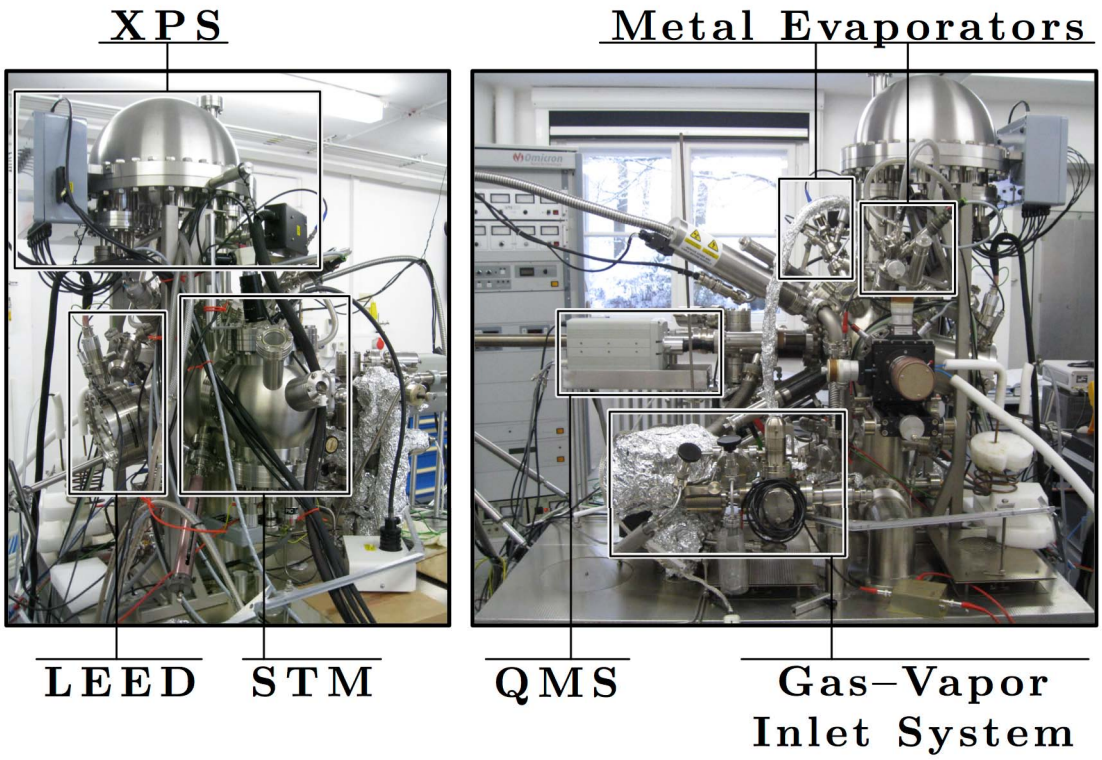

Figure 2.1: The Omicron UHV system that was used in this study.

- A tubular gas doser with 10 mm inner diameter and a 20 μm pinhole, which is used for dosing gases and liquid vapours of controlled amount onto the sample surface.

- A leak valve, which is used for back-filling the chamber with a gas, keeping precise control on the pressure within several orders of magnitude.

Photographs of the setup, with the main instruments enclosed in rectangles, are presented in Figure 2.1.

The vacuum in the chamber is generated and maintained by several pumps. In the first stage, a turbomolecular pump (turbo pump) backed by a rotary pump brings the pressure from 1 bar to 10^{-6}–10^{-5} mbar. A bake-out procedure at 140 °C for ∼40 hours is applied to remove the adsorbed water on the chamber walls. After bake-out, the turbo pump and/or the ion pump brings the pressure down to the 10^{-10} mbar range. Reducing the pressure even further, down to the 10^{-11} mbar range, can be achieved with the help of the titanium sublimation pump (TSP). Nevertheless, typical pressures in the chamber were in the range of 1–3×10^{-10} mbar, due to the frequent use of oxygen gas.

2.2 The Substrate and Sample Holder Design

The substrate used in this study is rutile–TiO_2(110), which will henceforth be called TiO_2(110). TiO_2(110) has become "the" model system for the surface science of oxides, due to its high stability, sufficient electrical conductivity for surface science techniques (when the bulk of the crystal is slightly reduced), and the wide range of applications of TiO_2.

Working with TiO_2 crystals requires the consideration of a couple of important points. The first point is the brittleness of the crystal. A small scratch that remains from the preparation (i.e. cutting and polishing) may grow in the presence of mechanical or thermal stress and lead to fracture. This is a point of concern especially because the thermal conductivity of TiO_2 ($\sim$10 W/(m·K)) is lower than that of metals (10–400 W/(m·K)), meaning that heating them fast will produce large temperature gradients within the crystal, in turn creating thermal stress. Thus large temperature gradients and mechanical stress should be eliminated, to the extent possible.

The second point is the low electrical conductivity. Although slight chemical reduction renders a TiO_2 crystal reasonably conducting (ρ = 10–100 Ω cm) stoichiometric TiO_2 is electrically insulating (ρ = 2000 Ω cm) [20]. Care should be taken in order to keep the surface of a crystal reduced, since oxidation starts there and one can suffer from electrical charging due to surface oxidation.

Our sample holder design takes into account the aforementioned points. Side and top views of a sample–sample holder assembly with a mounted TiO_2(110) sample can be seen in Figure 2.2. There are tantalum plates on the sides which are slid into the grooves machined to the sides of the crystal. They press the TiO_2 crystal to the backing plate. The titanium screws, which go all the way down to the sample plate, are used to adjust the pressing force.

The crystal is heated by a tungsten filament that sits in a partially closed cylindrical tube just behind the sample holder. The filament is electrically isolated from the sample and the manipulator. Heating is achieved via two effects: radiative heat transfer and bombardment of the sample with high energy electrons. For the second mechanism, the sample is held at a positive potential (U_h = 500–1200 V), creating an electric field which strips electrons from the heated filament. These electrons are accelerated towards the backing plate by the voltage difference, and heat the plate up with their impact. In order for the electrons to reach the backing plate, a hole (4×5 mm^2) is machined in the sample plate.

In the earlier experiments of the thesis, another sample holder with the same design but made completely out of platinum, was used. The switching to tantalum was motivated by the poor stability of thermal contact that manifested itself in TPD experiments. The thin platinum foil behind the crystal, which was buckling due to its thinness, was thought to be responsible for the effect. Most of the data has been obtained using the tantalum sample holder. Tantalum is the material of choice for its stability at high temperatures. The oxide layer that forms on the surface of tantalum is not volatile, thus it does not contaminate the TiO_2 surface. One should however be careful not to let the oxide layer

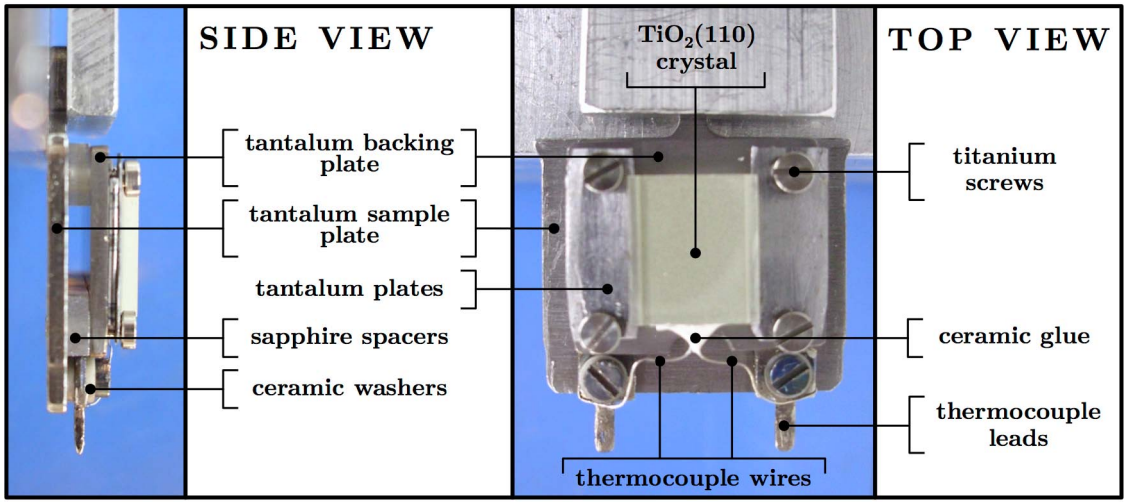

Figure 2.2: The sample holder construction that was used in most of the experiments in this study.

grow too thick, which would then lead to poor electrical conductivity. Some implications of such over-oxidation have been observed at the latter stages of the experiments.

The sample plate forms the main body of the holder assembly and its shape is standard for many Omicron instruments. The sapphire spacers help to isolate the crystal from the rest of the system thermally, allowing higher temperatures at the sample without heating the manipulator too much and also preventing sharp temperature changes. A backing plate is then required for the crystal. This is a tantalum plate which is relatively thick (1 mm) to prevent deformation at high temperatures and preserve a flat surface for good thermal contact.

A K-type (alumel–chromel) thermocouple is glued to the bottom side of the crystal using a ceramic glue. The wires are spot-welded to leads which are made of the corresponding thermocouple materials and are electrically insulated from the sample holder by being placed between two ceramic washers. There is a hole made in each lead which allows the titanium screw to go through. The type of washer used extends into this hole, preventing electrical contact between the screw and the thermocouple. The leads go into their sockets, when the sample holder is put into its position in the manipulator. The sockets and the rest of the wires that are connected to the thermocouple in UHV are also made of alumel/chromel wires in order to prevent generation of additional thermal voltage in the presence of a temperature gradient.

2.3 Preparation of the Substrate

The crystals have been provided from two companies. MaTecK GmbH and Crystal GmbH. Initially, a cylindrical rod of rutile–TiO_2 had been purchased from MaTecK. This rod was cut into rectangular ($7 \times 8 \times 2$ (or $7 \times 8 \times 3$) mm^3) crystals, and polished on one side by

using standard methods. Crystal orientation was determined using Laue back-scattering. Processing of the cylindrical rod into a polished, rectangular single crystal has been carried out by the crystal-lab of the Fritz Haber Institute. After a certain period of working with these crystals, it has been realized that their surfaces possessed a significant number of micro-scratches, which were by-products of the polishing procedure. Since these scratches resulted in small terrace size and high step density, which is not desired, already-cut and polished crystals ($7\times8\times2$ mm^3) without such micro-scratches were purchased from Crystal GmbH from that time on and the previous procedure was abandoned. The majority of the data that is presented in this thesis was obtained from the latter type of crystals.

A new TiO_2 crystal has to be treated in UHV before using, for two main reasons. First, as every fresh single crystal, TiO_2 contains impurities in its bulk. Although their concentrations are relatively small ($< 0.1\%$), those which diffuse fast enough and segregate at the surface may accumulate there in significant amounts when the sample is heated. The most common impurity that is observed in TiO_2 single crystals is calcium. Other than calcium we observed small amounts of magnesium and potassium in our crystals. The amount of magnesium was greater in the crystals supplied by MaTecK. These impurities have to be removed to the extent that the surface is clean enough for STM imaging. In our case, as as a rule of thumb, a surface coverage above 0.1% is not desired for impurities. This is because the coverages of the surface structures that we are interested in can be as little as $\sim$1%. The second reason that the TiO_2 crystals must be treated is that the stoichiometric crystals are electrically insulating. By creating a small amount of defects in its bulk, a TiO_2 crystal can be made conductive enough for the application of the techniques of interest (i.e. LEED, XPS and STM).

In order to clean our crystal, and also render it conductive, a series of sputtering and annealing cycles was applied. The crystal was sputtered with argon ions of 1000 eV energy, and then annealed in UHV at 850–950 K for 10–30 minutes. Sputtering removes the impurities at the surface and since lighter atoms are removed more efficiently than heavier atoms, the oxygen to titanium ratio after sputtering is less than 2 (i.e. the surface region becomes reduced). During annealing, the surface stoichiometry is restored by diffusion of atoms between surface and bulk. The diffusion of defects at the surface region into the bulk gives TiO_2 n-type conductivity and a colour well visible to the naked eye. While stoichiometric rutile–TiO_2 is transparent with a pale yellow tint, as the concentration of bulk defects increases, the colour of a crystal changes from azure to darker shades of blue and finally becomes black. It should be noted that just annealing TiO_2 in UHV, without any prior sputtering, also leads to the formation of bulk defects and to the reduction of the crystal. In that case however, the surface defects that diffuse to the bulk are generated thermally, by loss of oxygen from the surface at high temperature. This mechanism of reduction becomes more dominant as the annealing temperature and duration is increased.

The aforementioned sputtering–annealing cycle was applied several times until the impurity concentrations were near or below the detection limit of XPS. Although this procedure cleans the surface nicely and renders the crystal electrically conductive, the average terrace size of the surface becomes smaller with sputtering. Large terraces are preferred for STM imaging and in order to obtain this, a different procedure was applied before preparing a

mixed-oxide layer. Once the old layer on the substrate was removed by sputtering, the crystal was annealed to 970 K in 1×10^{-7} mbar oxygen ambient for 10–20 minutes (sample was positioned in front of the gas doser for obtaining a higher effective pressure at the surface). The temperature and pressure used in this treatment favour the growth of existing terraces instead of formation of new terraces [21]. After annealing in oxygen, the sample was first cooled to 850 K in UHV and annealed at that temperature for 10–15 minutes (also in UHV). Then it was cooled down to room temperature. Annealing in UHV was required to create atomically flat terraces. Details of why this is required will be explained in the next chapter.

2.4 X-Ray Photoelectron Spectroscopy (XPS)

The photoelectric effect was first observed by Heinrich Hertz in 1887 during his experiments which were dealing with fast electrical oscillations. After the key experimental findings of Philip Lenard [22, 23], demonstrating the nature of the phenomenon, came Einstein's classic paper [24], explaining the observations based on a discontinuous distribution of light in space. X-ray photoelectron spectroscopy (XPS) exploits the photoelectric effect to analyse the chemical composition of surfaces. XPS relies on the fact that different elements have significantly different core level electron energies. The energy resolution of the technique is even high enough to differentiate an element in different chemical environments.

Electrons which are typical for XPS experiments (having 100–1000 eV kinetic energy) can only travel very short distances in matter without losing energy. This so-called inelastic mean free path (IMFP) is in the order of nanometres in solids, which makes XPS a surface sensitive technique. In order to get an IMFP in the order of meters outside the solid (which is required for the analysis of the kinetic energy distribution of electrons), the experiment has to be performed under UHV conditions. However, with the recent advances, XPS can also be performed at higher pressures [25–27].

2.4.1 Theory of Photoemission: What is Actually Measured in XPS?

Photoemission is the process where an electron bound to an atom is ejected out via absorption of a photon. As a result of photoemission, a free electron with a certain kinetic energy is released, and a half-empty orbital is left behind, which is called a "hole". A schematic representation of the photoemission process is shown in Figure 2.3.

The energy conservation equations for a photoemission process can be written in different forms for the cases of a free atom (or molecule) and a solid. For an atom, the equation can be written as:

$$E_{kin} = h\nu - (E_f^{N-1} - E_i^N) \tag{2.1}$$

Equation 2.1 gives the kinetic energy of the photoelectron (E_{kin}) in terms of photon energy ($h\nu$) and initial (E_i^N) and final (E_f^{N-1}) total energies of the atom/molecule. The superscripts of the energy terms indicate that the initial state contains N and the final state contains $N-1$ particles, due to the removal of one electron from the atom/molecule.

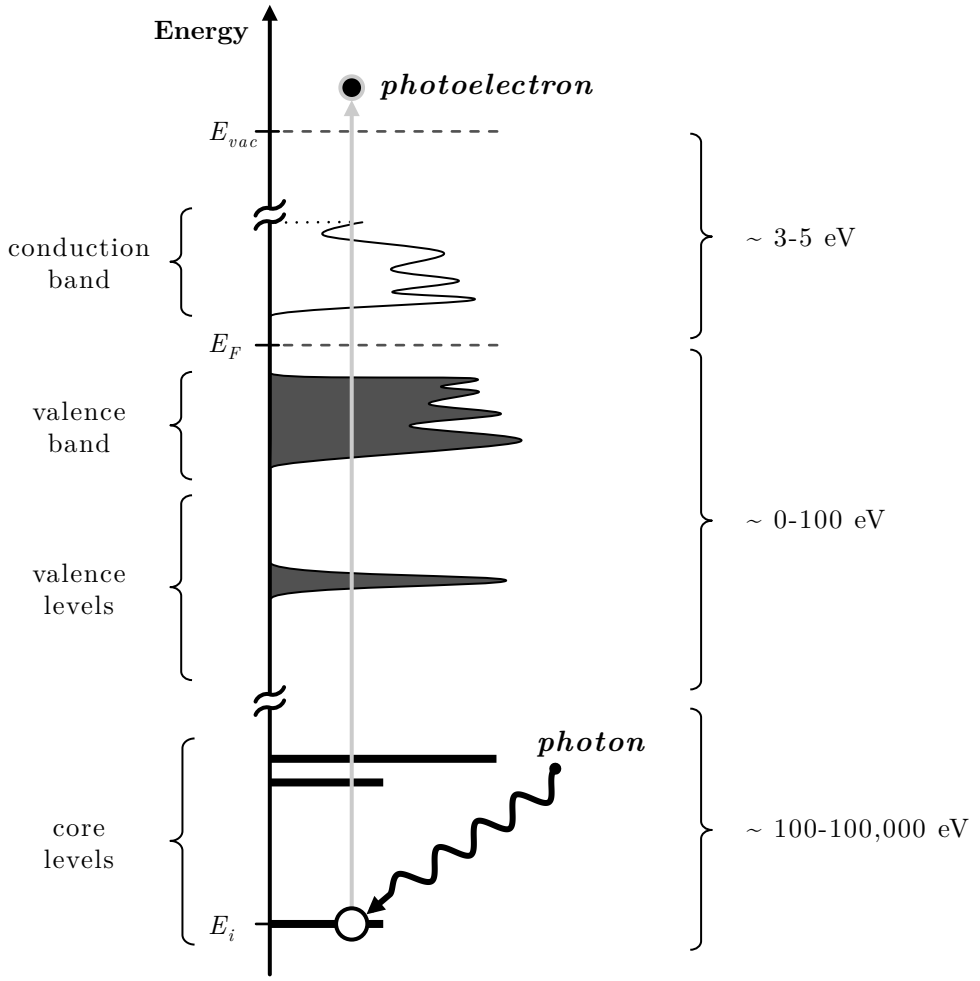

Figure 2.3: A schematic representation of the photoemission process from an insulator (or semi-conductor). In this particular case, a high energy photon ($\sim 10^2$–10^3 eV) ejects a core-electron into vacuum. Energy levels are drawn based on the state of the system before photoemission. Order of magnitude of energies of valance and core orbitals are indicated on the right.

One should keep in mind that, in this case, zero orbital energy corresponds to the vacuum level. For a solid, which is more relevant for our experiments, equation 2.1 is modified to:

$$E_{kin} = h\nu - (E_f^{N-1} - E_i^N) - \phi \tag{2.2}$$

Equation 2.2 is for a solid, where one can talk about a Fermi level. Different from the case of a free atom, in this case, zero energy is defined as the energy of the Fermi level. Because of this, the additional "work function" term is added (ϕ).

At this point, a brief definition of work function is appropriate. Work function is defined as "the energy difference between two states of a crystal, the states defined such that one is the ground state, and the other is a state where one electron is removed from inside the bulk, from a state directly at the Fermi level and brought outside the crystal to a certain distance (typically 10^4 Å) through a certain facet" [28]. The mentioned distance is such that it is large enough, so the force due to image charge can be neglected, but small enough, so the effect of the certain facet, which the electron is removed through, can be observed. This definition is required to be able to assign different work functions to different facets of a crystal.

One of the most common terms used in XPS literature (if not the most) is "binding energy" (E_b), which is defined as:

$$E_b = E_f^{N-1} - E_i^N \tag{2.3}$$

and thus equation 2.2 becomes:

$$E_b = h\nu - E_{kin} - \phi \tag{2.4}$$

With this equation, the binding energy, which is defined relative to the Fermi level, is given in terms of known ($h\nu$) and measurable (E_{kin}, ϕ) quantities in XPS experiments.

The simplest approach to the calculation of binding energies is Koopmans' theorem (KT). In this scenario, Hartree–Fock (HF) orbitals are assumed to be "frozen" during photoemission and the difference in energies is calculated. In this calculation the difference ($E_f^{N-1} - E_i^N$) equals the HF orbital energy of the removed electron ($-\varepsilon_k$, k denoting the orbital of the ejected electron).

$$E_b^{KT} = -\varepsilon_k \tag{2.5}$$

Although this energy can be calculated very precisely, the problem is the weakness of the initial frozen orbital (FO) assumption. Core-level binding energies calculated using this scheme are typically 10–50 eV higher than the experimentally measured binding energies. The difference between the real situation and the FO approximation is that once a core hole is generated, there is a rearrangement of electron density (relaxation) which reduces the final state energy.

2.4.2 Factors Affecting the Binding Energy

The definition of binding energy, as given in equation 2.3, is the difference between the initial and final states of a system. This system may be anything from a single atom to a complex solid. The complexity of the system increases the complexity of the theoretical treatment as one would expect. Nevertheless, the original definition is important for understanding the origin of binding energy shifts.

The final state of a photoemission event in which full relaxation is achieved has the lowest energy among the possible final states and thus produces the line with the lowest binding energy. The other final states exhibit higher energies and produce lines at higher binding energies.

Two extreme cases are considered in photoemission. The first one is the so-called adiabatic limit where the photoelectron leaves the system sufficiently slowly so full relaxation is achieved before the photoelectron leaves the atom. The fully relaxed final state gives rise to the line with the lowest binding energy. The second case is the "sudden limit" where the photoemission process is so fast (i.e. the photoelectron has high kinetic energy) that the other electrons can not reorganize (relax) before the photoelectron leaves the system. In this case, there are often other electronic excitations accompanying the photoemission event such as shake-up (excitation of a valence electron to an unoccupied state) and shake-off (removal of a valence electron from the system). An excited final state has a higher energy and gives rise to a line at a higher binding energy. The energy loss processes that take place after photoemission during the travel of a photoelectron through the solid are termed "secondary processes", and such a process may also lead to a distinct feature in a spectrum, without being named as a final-state effect.

The change in the binding energy due to a change in the chemical environment of an element is called chemical shift. Chemical shift is strongly correlated with initial state energies, thus examples in the literature which incorrectly treats it as a purely initial-state effect are not uncommon. It is worth emphasizing that in theory binding energy itself and its change due to the chemical environment are functions of both the initial and final state energies of a system.

In estimating chemical shifts, types, numbers and distances of neighbouring atoms are relevant. The most practical (thus common, but potentially unreliable) use of chemical shifts is assigning each to a certain formal oxidation state. The charge potential model, which is a rather old and oversimplified one, can also be used to predict the shift from a reference binding energy. It is expressed in atomic units as:

$$E_b^i = E_b^{ref} + kq_i + \sum_{j \neq i} \frac{q_j}{r_{ij}} \tag{2.6}$$

E_b^i is the binding energy of atom i and E_b^{ref} is a reference binding energy appropriate for that atom. q_i is the charge on atom i and q_j the charge on the neighbouring atom j. r_{ij} is the distance between atoms i and j. k is a proportionality constant for atom i. It is a measure of the interaction between the valance and core electrons, which determines the strength of screening of the core hole. k is fixed for a certain element.

Based on this model, it can be seen that as the oxidation state of an element increases, the binding energy also increases (q_i is more positive with increasing oxidation state). The third term, which accounts for the field of the displaced charge from the central atom, counteracts the second one because the sign of q_j is opposite to that of q_i, at least in the next atomic shell.

2.4.3 Experimental Aspects of XPS

An XPS system basically consists of an x-ray source and an electron energy analyser, where x-rays knock off electrons from the sample and the analyser counts them as a function of their kinetic energy. Typical lab sources generate x-rays by accelerating electrons emitted from a hot filament to a metal anode. Two basic processes generate x-rays: bremsstrahlung and fluorescence. Bremsstrahlung is the light generated due to the deceleration of the electron beam very near to the surface and has a broad spectral distribution. The sequence of events that leads to fluorescence starts when the beam eventually hits the anode and electrons are ejected from the metal, leaving behind holes in the electronic levels. These holes are filled by other electrons from higher energy levels and the extra energy is either released as radiation (fluorescence) or transferred to another electron to eject it out of the atom (Auger process). Fluorescent radiation has a characteristic energy which corresponds to the energy difference between the initial and final states of the atom. This energy typically falls in the range of x-rays for holes created in core levels and ultraviolet (UV) for holes created in valance levels.

A typical XPS instrument has two anode materials in its x-ray gun, namely aluminium and magnesium. The $K\alpha$ line, which is a result of electron transitions from 2p orbitals ($2p_{1/2}$ and $2p_{3/2}$) to 1s orbital, becomes the most intense line at the typical operation conditions and has an energy of 1486.6 eV for Al and 1253.6 eV for Mg. These sources however emit not only at these characteristic energies, but also at 8–70 eV higher energies with significantly lower intensities, which consequently produce small satellite peaks at lower binding energies in an XPS spectrum. Such issues are removed if technically and economically more demanding sources with monochromators are used. Synchrotron radiation is the ultimate monochromatic source which can be tuned in energy, polarisation, intensity and spot size.

The standard electron energy analyser for XPS systems nowadays is the hemispherical electrostatic analyser equipped with an electrostatic lens system at the entrance. Figure 2.4 shows such an arrangement. The analyser operates such that only electrons with a kinetic energy equal to the so called "pass energy" (E_p) can reach the detector at the end. There are two modes of operation for the analyser. In the first mode, the pass energy, which is set by the experimenter, is kept constant during a scan. Having a fixed kinetic energy in the analyser ensures a fixed energy resolution throughout the spectrum. This mode of operation is called "constant analyser energy" (CAE) mode. A higher pass energy provides a higher signal to noise ratio, in the expense of energy resolution. Conversely, decreasing the pass energy improves the resolution in the expense of signal intensity. The other operation mode of the analyser is the "constant retard ratio" (CRR) mode. In this mode, the electrons are retarded by a constant proportion of their kinetic energy, so the

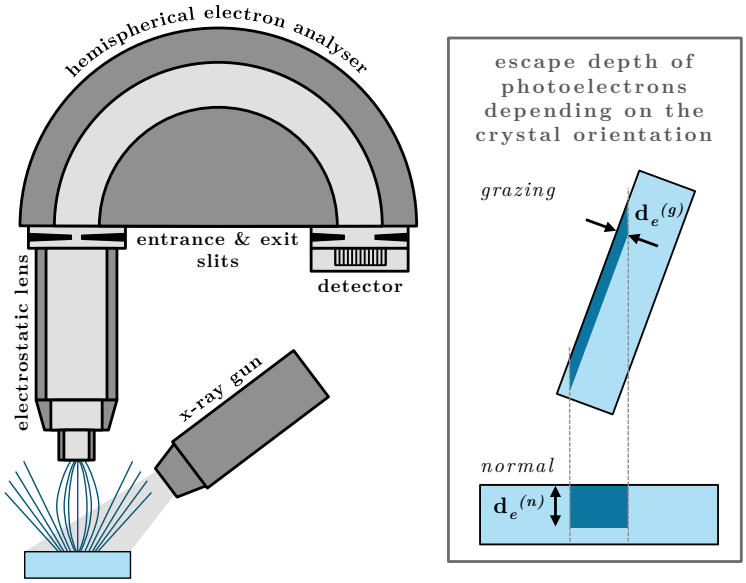

Figure 2.4: Components of an x-ray photoelectron spectrometer and illustration of how the surface sensitivity of the measurement depends on the orientation of the sample relative to the analyser.

pass energy has to be varied automatically during a scan. The advantage of the CRR mode is that the cone that the electrons are collected from is almost unchanged throughout the spectrum.

The hemispherical part of the analyser consists of two concentric hemispheres. A potential difference is applied between the two which forms a radial electric field. In this field, only the electrons having a kinetic energy E_{pass} are deflected into the detector, whereas those with higher or lower kinetic energies hit the analyser walls before reaching it. The electrons which reach the exit of the analyser are counted by means of an electron multiplier since the current at this point (and even earlier) is too weak to be measured directly. In modern analysers, there is almost always more than one multiplier and even spatial resolving can be made using a microchannel plate detector.

The electrostatic lens system at the entrance decelerates the photoelectrons, reducing their kinetic energy by E_{ret}. In the CAE mode, the energy of retardation (E_{ret}) is the only quantity that is varied by the computer during a scan. Once the parameters are set, an XPS scan is essentially recording the detector signal while varying E_{ret}. The important part of the analysis is converting E_{ret} to binding energy, which is explained next.

As already mentioned, the calculation of the binding energy requires the knowledge of the sample work function and the kinetic energy of the electron just outside the sample. The problem with this scheme is that the sample work function has to be known in every measurement. Fortunately, in practice, the situation can be simplified by putting the sample and the analyser in electrical contact. In that case, their Fermi levels come to the

same energy and then the energy conservation equations can be expressed as:

$$h\nu - E_b = \phi_s + E_{kin,s} = \phi_a + E_{kin,a} = \phi_a + E_{ret} + E_{pass} \tag{2.7}$$

$E_{kin,s}$ is the kinetic energy of electron just outside the sample and $E_{kin,a}$ near the analyser. ϕ_s and ϕ_a are the work functions of the sample and the analyser respectively. Since the Fermi levels are the same at the analyser and the sample, the energy of the electron above that level ($h\nu - E_b$) is conserved while moving from the grounded sample to the grounded analyser (more precisely to the lens entrance). Thus from an experimental point of view, the relation:

$$h\nu - E_b = \phi_a + E_{ret} + E_{pass} \tag{2.8}$$

is used to calculate the binding energy, and there is no need to know the work function of the sample but the one of the analyser.

The function of the lens system is not only changing the kinetic energies of the electrons but also focusing the emitted electrons into the entrance of the hemisphere. Focusing parameters (i.e. the voltages at different parts of the lens system) can be altered by the experimenter in order to define the analysed area on the sample. In addition to the lens voltages, the two slits at the two ends of the hemisphere and the size of the x-ray beam also contribute to the size and shape of the analyzed region.

As already mentioned earlier, the surface sensitivity of XPS stems from the short inelastic mean free path (IMFP) of electrons in solids (λ). 95% of the measured photoelectron intensity comes from a surface region of 3λ thickness. Practical ways of further increasing the surface sensitivity exist, one of which is illustrated in Figure 2.4. The usual positioning of a sample in an XPS experiment is such that the angle between the surface normal of the sample and the axis of the analyser is 0° (normal). If this angle is increased to θ (grazing) then the electrons also have to travel parallel to the surface in order to leave the solid in the direction of the analyser. The mathematical relationship between the angle of rotation and the escape depth is straightforward.

$$d_e = \lambda \cos(\theta) \tag{2.9}$$

According to this relationship, if the sample is rotated by 70°, the surface sensitivity would increase by ∼3 times. Another important consequence of such a configuration would be the widening of the analysed area by about the same factor, as shown in Figure 2.4.

Another method for increasing surface sensitivity in an XPS experiment is using a photon energy that would create photoelectrons with a kinetic energy in the range of 50–100 eV. At this range, the IMFP of electrons in solids goes through a minimum, hence λ is minimized. Although such photon energy tuning can only be performed in a synchrotron, the surface sensitivity obtained, when combined with grazing angle detection, is very significant.

2.4.4 Quantification in XPS

In XPS, peak intensities are affected by intrinsic and extrinsic contributions. In the first category is the photoemission cross-section (σ), which is the probability of electron emission for a given photon flux. σ depends on the type of atom and the electronic level from which the electron is ejected from as well as on the frequency and the polarization of ionizing light. In order to obtain a better signal to noise ratio, core levels with higher cross-sections are preferred in atomic quantification whenever possible. Furthermore, the angular distribution of photoelectrons is not uniform. In an isotropic medium, where the ionizing light is unpolarized, the relationship is:

$$\frac{\mathrm{d}\sigma}{\mathrm{d}\Omega} = \frac{\sigma}{4\pi}\left[1 - \frac{\beta}{4}\left(3\cos^2(\theta_\sigma) - 1\right)\right] \tag{2.10}$$

θ_σ is the angle between the direction of light propagation and the direction of photoelectron ejection. $\mathrm{d}\Omega$ represents a differential solid angle. β is an asymmetry parameter and depends on the photon energy, type of atom and the type of orbital that the electron is ejected from [29, 30]. σ and β are tabulated for different photon energies, elements and orbitals [31, 32]. For $\theta_\sigma \approx 54.7°$ (the magic angle), the term in parentheses (i.e. $(3\cos^2(\theta_\sigma) - 1)$ becomes zero and the total cross-section can be used without the need for the asymmetry parameter. For most commercial spectrometers, 54.7° is the design angle between the x-ray source and the analyser.

Theoretically, photoemission cross-section is a measure of the overlap between the initial and final state wavefunctions of the system under the influence of the electric field of the incoming electromagnetic radiation (x-rays here). The so-called Fermi's golden rule, which describes the transition probability between two states of a system, can be adapted to the present case as:

$$\sigma \propto |\,\langle \Phi_f \,|\, \boldsymbol{A}\cdot\boldsymbol{p} \,|\, \Phi_i\rangle\,|^2\ \delta(h\nu - E_i - E_f - E_{kin}) \tag{2.11}$$

where $\boldsymbol{A}$ is the vector potential associated with the electromagnetic field of the radiation and $\boldsymbol{p}$ is the momentum operator. Φ_i and Φ_f are the wavefunctions of the system in the initial and final state respectively. The Dirac delta function (δ) is present to account for the energy conservation.

Extrinsic factors that contribute to peak intensities can be listed as, x-ray flux (F), transmission function of the analyser (T), atomic concentration (number per volume) of the element in question (n_i) and attenuation of photoelectrons while passing through the solid. The signal due to element i coming from an infinitesimally thin layer of thickness $\mathrm{d}z$ is proportional to:

$$n_i\,\mathrm{d}z \tag{2.12}$$

The attenuation factor for electrons originating from depth z can be expressed based on the Beer–Lambert law, and using the IMFP for the electron (λ) as:

$$e^{-\frac{z}{\lambda\cos(\theta)}} \tag{2.13}$$

where θ is the angle between the surface normal and the analyser axis. When the attenua-

tion factor is introduced and the signal is integrated through the overall sample thickness, we get:

$$\int_0^\infty n_i \; e^{-\frac{z}{\lambda \cos(\theta)}} \, \mathrm{d}z \tag{2.14}$$

If we assume that the transmission function contains all the factors related to the analyser (angular acceptance, analyzed area of the sample, detector efficiency), the intensity of the photoemission peak of level j of atom i (I_{ij}) can be expressed as:

$$I_{ij} = F \; T \; \sigma_{ij} \int_0^\infty n_i \; e^{-\frac{z}{\lambda \cos(\theta)}} \, \mathrm{d}z \tag{2.15}$$

It is important to keep in mind that T and λ are functions of photoelectron kinetic energy (E_{kin}), and σ_{ij} is a function of photon energy. The intensity may deviate from this equation when a single-crystalline sample is used because of the diffraction of the photoelectrons by the sample itself. The effect can be minimized by using a large acceptance solid angle ($> 20°$) [33].

The contribution from deep layers ($z > 3\lambda \cos(\theta)$) to the integral in equation 2.15 is negligible ($< 5\%$) for most practical cases. In the case where n_i is not a function of z (at least for $z < 3\lambda \cos(\theta)$), the expression can be analytically integrated to give:

$$I_{ij} = F \, T \, \sigma_{ij} \, n_i \, \lambda \cos(\theta) \tag{2.16}$$

In quantification, the aim is usually to get the unknown quantity n_i from the measured quantity I_{ij}. Although the absolute values for the transmission function and the x-ray flux are rarely available, these are not needed in practice since the aim is usually to calculate relative concentrations. X-ray fluxes cancel out for different elements. The dependence of the transmission function to the photoelectron kinetic energy is available for different analysers and T for each element can be calculated relative to the others.

In the case where the sample is not a homogeneous mixture, a structural model has to be assumed for the surface layers (if not already known), and the relations for quantification have to be derived.

2.5 Low-Energy Electron Diffraction (LEED)

LEED is a surface sensitive technique for the analysis of crystalline surface structures. The technique is based on the back-scattering of an electron beam from surface atoms. Information about the surface is obtained from the shape of the pattern, and the intensity and the profile of the spots. In the toolbox of the surface scientist, it is usually the first and easiest way of checking surface cleanliness and order by observing the sharpness of the diffraction spots and the intensity of the background. In a quantitative way, it can be used to determine the periodicity of an adsorbate layer. It can also be performed in the LEED–IV or SPA–LEED (Spot Profile Analysis) modes, where the instrumentation is more advanced. In LEED–IV, the intensities (I) of some diffraction spots are measured as a function of electron beam energy (V). The resulting curves have to be reproduced

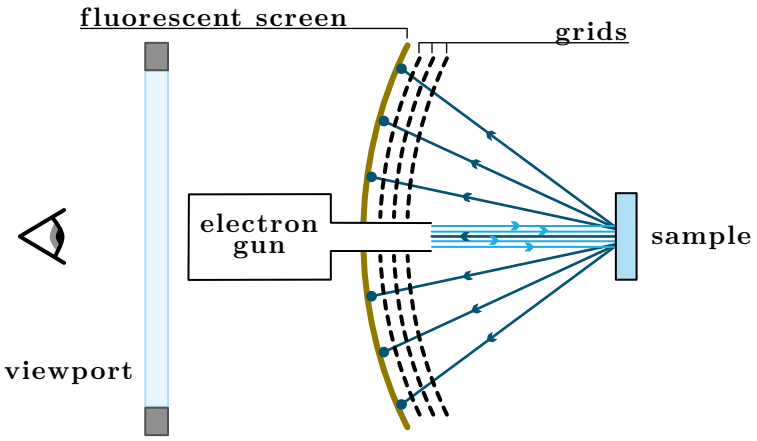

Figure 2.5: Main components of a LEED system. In this type of construction, the pattern that forms on the fluorescent screen can be viewed through the viewport and recorded by an external device, such as a digital camera. Note that the electron gun remains in view and thus part of the pattern is not visible.

by theoretical calculations to a certain degree of accuracy. Calculations take multiple scattering of electrons from the first few layers of the surface into account. The calculation process requires an initial guess for the structure and proceeds iteratively to find the correct structure. IV–LEED is one of the most powerful methods for surface structure determination [34]. In SPA–LEED, shapes of diffraction spots are measured. From the broadening and sharpening of the spots, information regarding the density of defects and processes like surface phase transitions can be extracted.

The most commonly used LEED system can be illustrated in a simplified form as in Figure 2.5. In this arrangement, electrons are sent perpendicularly to the sample surface and back-scattered electrons form a diffraction pattern on the fluorescent screen. The first and the last grid are kept at ground potential and the second grid is biased negatively. The grounded grids function as shielding to the electric field generated by the second grid (which often consists of two grids for practical purposes). The function of the negatively biased grid is to repel the inelastically scattered slow electrons ("secondaries") which actually constitute a significant part of the total back-scattered electrons. The fluorescent screen is biased positively at a few kilovolts for accelerating the electrons before strike, in order to create a visible fluorescence. The pattern that forms on the screen can be viewed through the viewport and recorded by a camera.

The wave nature of matter is responsible for the diffraction of electrons from an ordered surface. According to the deBroglie relation, the wavelength of a particle (electron in this case, λ_e) depends on its kinetic energy (E_{kin}) as:

$$\lambda_e = \frac{h}{\sqrt{2\, m_e\, E_{kin}}} \tag{2.17}$$

h being the Planck's constant, and m_e the mass of electron. When the constants are introduced in appropriate units, the equation becomes:

$$\lambda_e \cong \frac{12.3}{\sqrt{E_{kin}}} \tag{2.18}$$

where kinetic energy and wavelength terms are in eV and Å units respectively. That means electrons with 50–200 eV kinetic energy have wavelengths of 1.7–0.9 Å, which is comparable to interatomic distances.

In a one dimensional lattice, and with an incident beam that comes perpendicular to it, the condition for diffraction is satisfied when the below equation holds.

$$d\sin(\theta) = n\lambda_e \tag{2.19}$$

Here, d is the distance between two neighbouring lattice points (which act as scatterers), θ is the scattering angle (the angle between the scattered beam and the incoming beam—which is the surface normal in this case), n is the order of diffraction ($n = 0, 1, 2, \ldots$) and λ_e is the wavelength of the incoming electron. The distance between the diffraction spots on the fluorescent screen (i.e. the periodicity of the LEED pattern) is proportional to $\sin(\theta)$. Since the right hand side of the equation is constant, the periodicities of the lattice and the LEED pattern are inversely proportional.

A real 2D lattice which is represented by base vectors $\boldsymbol{A_i}$ and $\boldsymbol{A_j}$ has a reciprocal lattice with base vectors $\boldsymbol{a_i}$ and $\boldsymbol{a_j}$ which satisfies the equation:

$$\boldsymbol{A_i} \cdot \boldsymbol{A_j} = 2\pi\delta_{ij} \tag{2.20}$$

where δ_{ij} is the Kronecker delta. The equation translates to:

$$|\boldsymbol{A_1}||\boldsymbol{a_1}|\cos(\alpha_{\boldsymbol{A_1},\boldsymbol{a_1}}) = 2\pi \tag{2.21}$$

$$|\boldsymbol{A_2}||\boldsymbol{a_2}|\cos(\alpha_{\boldsymbol{A_2},\boldsymbol{a_2}}) = 2\pi \tag{2.22}$$

$$|\boldsymbol{A_1}||\boldsymbol{a_2}|\cos(\alpha_{\boldsymbol{A_1},\boldsymbol{a_2}}) = 0 \tag{2.23}$$

$$|\boldsymbol{A_2}||\boldsymbol{a_1}|\cos(\alpha_{\boldsymbol{A_2},\boldsymbol{a_1}}) = 0 \tag{2.24}$$

where $\alpha_{\boldsymbol{K},\boldsymbol{L}}$ is the angle between vectors $\boldsymbol{K}$ and $\boldsymbol{L}$.

An example for the transformation of a real lattice into its reciprocal lattice is presented in Figure 2.6. The pattern at the top left is a real lattice with hexagonal symmetry, and the corresponding reciprocal lattice is seen on its right. The base vectors of these lattices are given in the middle, in black colour. At the bottom, drawn in red colour is another lattice, which is superimposed on the previous one, with its base vectors given in the middle together with the black vectors. The lengths of the vectors are given in parentheses. In

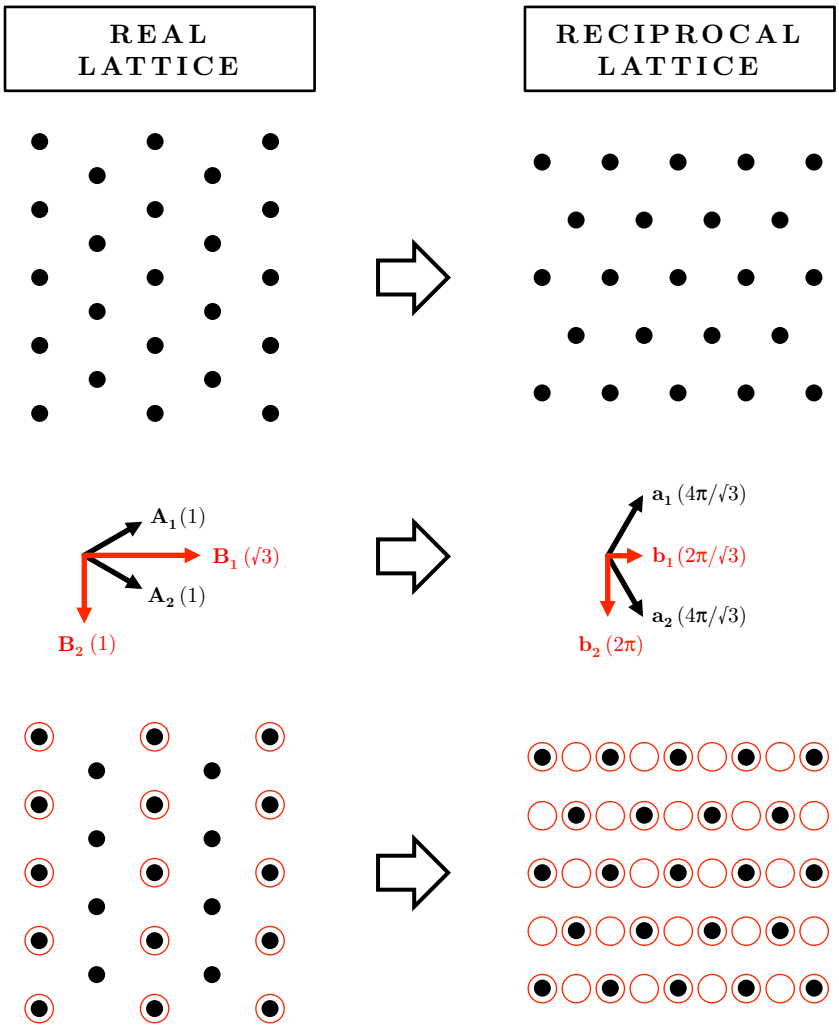

Figure 2.6: An example for the transformation of a real lattice into its corresponding reciprocal lattice. The black dots represent the periodicity of a bare surface and the red circles represent the periodicity of an overlayer on this surface. The vectors represent the lattice vectors for the bare surface (black) and the overlayer (red). The numbers in parentheses are the lengths of the vectors. The extra red circles in the reciprocal lattice are due to the adsorbate layer and some of them overlap with the original spots.

this example, the black lattice can be thought as a bare metal surface with closed packed atoms and the red lattice as an adsorbate layer with the given periodicity. It is worth noting that the adsorbate layer, which is more loosely spaced than the metal atoms, leads to a LEED pattern where the extra spots are denser than the substrate spots.

2.6 Scanning Tunnelling Microscopy (STM)

Scanning tunnelling microscopy (STM) is a surface imaging technique, which is based on the tunnelling of electrons between a sample and a probe. The probe, which is a metal wire with a very sharp tip, is mounted on a computer controlled 3–piezo (x, y, z directions) system and is driven on the sample surface with 10–1000 nm/s speed (in some setups, the sample is mounted on the piezos instead of the tip). The sample has to be conductive in order for STM to work. A small voltage bias (ΔU) is applied between the sample and the tip, which supplies the driving force for a steady current. When the tip is brought very near to the surface (few Å), the so-called "tunnelling current" (I_t) develops. This tunnelling current is completely a quantum mechanical phenomenon, that doesn't have a classical analogue. It is the principal variable in the imaging process.

In a typical STM scan, the mode that is preferred is called the "constant current mode". In this mode, the tunnelling current is kept constant by an electronic feedback-loop system. If the tunnelling current increases due to decreasing tip-sample distance, the tip is retracted by the z-piezo and the current decreases back to the set value. In the reverse case, the tip is approached to obtain the set current, as one would expect. The dependence of the tunnelling current on the tip-sample separation is exponential and can be derived from a one-dimensional model [35] as:

$$I_t \propto e^{-2\kappa z} \tag{2.25}$$

where κ is typically around 1 Å^{-1}, which means that the tunnelling current increases one order of magnitude for each Å that the tip approaches the surface. Although the assumed model is a relatively simple one, the result is semi-quantitatively accurate for most STM experiments.

The fundamental phenomenon from which relation 2.25 stems is the overlapping of the wavefunctions of the sample and the tip. The overlap increases with decreasing distance, ultimately giving the exponential dependence. Furthermore, the tunnelling current is higher when the local density of states is higher at the same energy on different sides of the tunnelling gap. Therefore, taking the electronic structure of the tip fixed, the tunnelling current (to a first approximation) maps the local density of states of a surface. As a consequence, biasing the sample positively or negatively can yield different images. In the case where the sample is biased positively, electrons must flow from the tip to the sample, and tunnelling will be favoured if there is a high density of empty states on the sample side. In the reverse case, where the sample is biased negatively, electrons will flow from the sample to the tip and tunnelling is favoured in case there is a high density of filled states at the sample.

A more accurate model for calculating the tunnelling current has been developed by

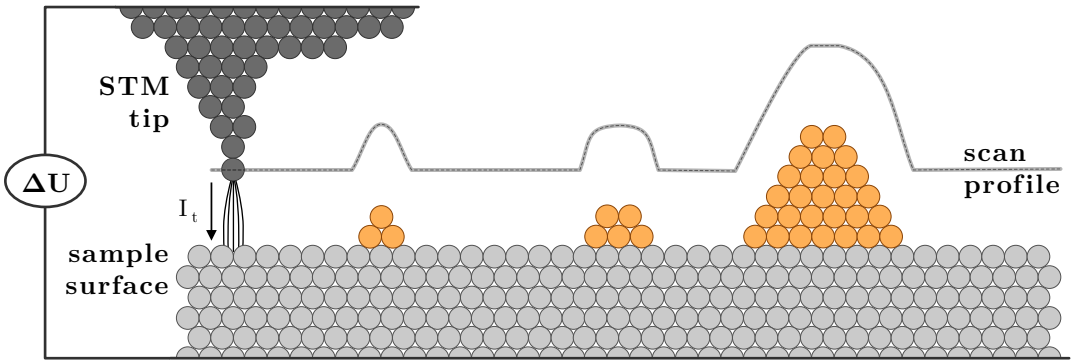

Figure 2.7: Cartoon representing the tip–sample interaction in a scanning tunnelling microscope (STM) operating in constant-current mode. A steady tunnelling current (I_t) is obtained by the application of a voltage bias (ΔU) between the tip and the sample, and kept constant by an electronic feedback loop. The obtained scan profile is dependent on the tip shape as well as on the surface morphology. As the features on the surface get higher, the shape of the tip is convoluted more into the profile.

Tersoff and Hamann [36]. Many assumptions are involved in the derivation like a small ΔU (∼20 meV), a locally spherical tip, and equal work functions for the surface and the tip. Other assumptions can be found in the original work. Under these conditions, the tunnelling current is approximated as:

$$I = \Delta U \; \frac{32\pi^3 \; e^2 \; \phi^2 \; D_t(E_F) \; R^2}{\hbar \; \kappa^4} \; e^{2\kappa R} \; \sum_{\nu} |\psi_\nu(\boldsymbol{r_0})|^2 \; \delta(E_\nu - E_F) \tag{2.26}$$

where

$$\kappa = \frac{\sqrt{2 \, m_e \, \phi}}{\hbar} \tag{2.27}$$

The subscripts μ and ν represent the tip and the surface respectively. ϕ is the work function, D_t is the density of states per unit volume of the tip, R is the radius of the tip curvature and $\boldsymbol{r_0}$ is the position of the center of the tip curvature. The summation is over all the surface states and $\psi_\nu(\boldsymbol{r_0})$ is the value of a surface wavefunction at position $\boldsymbol{r_0}$, which essentially causes the the exponential decay of the current with increasing tip–surface distance.

On the practical side of STM experiments, one point is worth mentioning. Figure 2.7 shows a cartoon of a tip–sample arrangement, with nanoparticles of different sizes on the surface. Since tunnelling can occur practically from every part of the tip that is close enough to the surface, the shape of the tip may result in different observed profiles when the sizes of the protrusions are large. Small protrusions are imaged relatively reliably, whereas the asymmetric shape of the tip gives an asymmetric profile for a larger particle.

For larger particles, the effect can be even more dramatic, producing an image of the tip itself instead of the particle.

2.7 Temperature-Programmed Desorption (TPD)

Temperature-programmed desorption (TPD), which is also sometimes referred to as thermal desorption spectroscopy (TDS), is a technique for studying surface–adsorbate interactions. In TPD, a sample with adsorbed molecules on its surface, is heated up with a constant heating rate and the desorption products are monitored by a mass spectrometer. The output of the experiment is a plot of mass signals (which are measures of gas partial pressures) versus temperature.

The basic components of a TPD setup is shown schematically in Figure 2.8. The signal from the thermocouple is fed to a temperature control unit, which controls the power of heating through a feedback loop. This arrangement increases the crystal temperature linearly as a function of time. The crystal is placed at the entrance of the mass spectrometer housing, which is commonly referred to as "Feulner cup". The Feulner cup has a small opening which allows desorption products to come almost exclusively from the sample and not from the surrounding surfaces. It is usually pumped differentially by a separate pump. Pumping is critical for getting high-quality spectra, since inefficient pumping leads to broadening of the peaks. The temperature and mass signals from the mass spectrometer are recorded with a computer and plotted into a spectrum.

Information that can be obtained from TPD are the kinetic parameters related to desorption like activation energy (E_d), the pre-exponential factor for desorption (ν) and the order of desorption (n). Qualitatively, TPD can be used to get an idea about the homogeneity of the surface as well, such that a relatively inhomogeneous surface will result in broader peaks than a relatively homogeneous surface.

The activation energy for desorption is an important quantity in TPD because it can be related to the heat of adsorption relatively easily. If the adsorption process proceeds without an activation barrier, then the activation energy of desorption is equal to the energy of adsorption. A more exact expression of the relationship is:

$$q_{st} \approx E_d + \frac{RT}{2} \tag{2.28}$$

where q_{st} is the isosteric heat of adsorption, R is the ideal gas constant and T is temperature. q_{st} is the difference of the molar enthalpy of the molecule in the gas phase (h_s) and the partial molar enthalpy of the molecule at the surface ($\bar{h}_s$), and is a positive quantity.

$$q_{st} = (h_g - \bar{h}_s) \tag{2.29}$$

The fundamental relationship in TPD, from which other relationships are derived, is the Polanyi–Wigner equation [37]. It gives the relationship between the rate of desorption and the kinetic parameters of desorption. It is essentially an n^{th} order rate equation, where the concentration is represented by "surface coverage" θ. The pumping is assumed to be

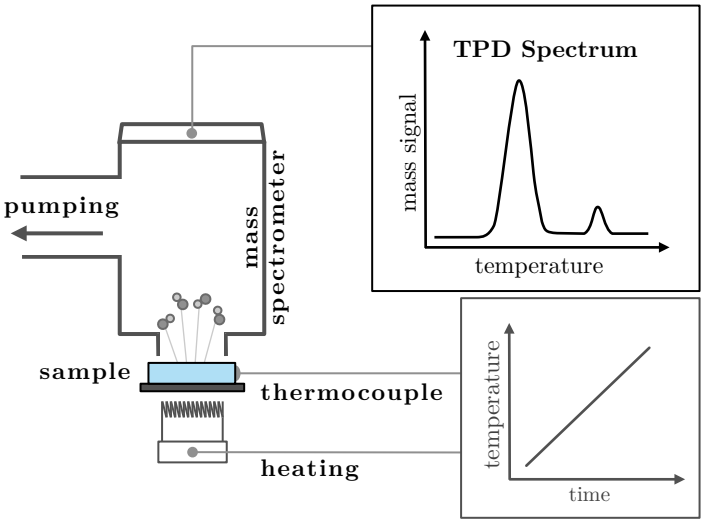

Figure 2.8: Basic scheme of a temperature programmed desorption experiment. A control loop is used to increase the sample temperature linearly and the desorption of the previously adsorbed species is monitored by a mass spectrometer.

infinitely fast so that the readsorption term vanishes.

$$r_d = -\frac{\mathrm{d}\theta}{\mathrm{d}t} = k_d\,\theta^n = \nu\,\theta^n\,e^{-\frac{E_d}{RT}} \tag{2.30}$$

In general, the pre-exponential factor (ν) is a function of coverage and temperature whereas the activation energy (E_d) is only a function of coverage. Nevertheless, these dependencies may not always be significant. Since the temperature is increased linearly, the rate of change of temperature is a constant (β).

$$\frac{\mathrm{d}T}{\mathrm{d}t} = \beta \tag{2.31}$$

Equation 2.30 takes the form:

$$-\frac{\mathrm{d}\theta}{\mathrm{d}T} = \frac{\nu}{\beta}\,\theta^n\,e^{-\frac{E_d}{RT}} \tag{2.32}$$

Equation 2.32 itself however does not provide a simple tool for extracting the parameters of interest from a TPD spectrum. The most popular relationship that is derived from equation 2.32 is the Redhead formula [38], which gives E_d as a function of the peak maximum temperature (T_{max}). It is obtained by differentiating both sides of the equation

with respect to temperature and inserting the values for peak maximum temperature.

$$E_d = RT_{max}\left[\ln\left(\frac{\nu T_{max}}{\beta}\right) - ln\left(\frac{E_d}{(RT_{max}}\right)\right] \tag{2.33}$$

In deriving this relation, the order of desorption is taken as 1 and the pre-exponential factor and activation energy are assumed to be independent of coverage. The second term in brackets is much smaller than the first one and can be approximated without affecting the end result too much:

$$\ln\left(\frac{E_d}{RT_{max}}\right) \approx 3.64 \tag{2.34}$$

Equation 2.33 then becomes:

$$E_d = RT_{max}\left[\ln\left(\frac{\nu T_{max}}{\beta}\right) - 3.64\right] \tag{2.35}$$

Equation 2.35 is a good approximation, given the value of ν/β is between 10^8 and 10^{13} K^{-1}. However convenient this formula might be, the value of the pre-exponential has still to be assumed and this is the major source of error in this calculation. A typical value to assume for ν is 10^{13} s^{-1}.

Another method which is worth mentioning is the leading-edge analysis [39]. This one is valuable because of the fact that a minimum number of assumptions is made. In this case, only the "leading edge" part of the spectrum is utilized, where the coverage is high but decreasing very slowly, which allows for the "constant coverage assumption". Since the leading edge is only a small temperature window, the obtained parameters can be assigned to that temperature. Taking the logarithm of equation 2.30, we obtain:

$$\ln(r_d) = \ln(\nu) + n\ln(\theta) - \frac{E_d}{RT} \tag{2.36}$$

A plot of $\ln(r_d)$ .vs. $(1/T)$ gives a straight line with the slope $-E_d/R$. The intercept can be used to calculate the pre-exponential factor. The only disadvantage of the leading edge analysis is the requirement of high quality data.

3 OXIDES OF TITANIUM AND MOLYBDENUM

In this chapter, oxides of titanium and molybdenum are introduced. Phase diagrams are presented as composition .vs. temperature plots. The rutile–TiO_2(110) surface is dwelt on, since it is the most relevant surface to this study. TiO_2 (rutile, $P4_2/mnm$) and MoO_2 (monoclinic, $P21/c$, can be considered as "distorted" rutile) have similar structures and mixing of compounds with similar crystal structures may be, at least to a certain extent, be expected. Studies regarding the mixing of these two oxides are summarized in the last part.

3.1 The Titanium–Oxygen System

The titanium–oxygen binary system has a rich phase diagram, which is plotted in Figure 3.1.

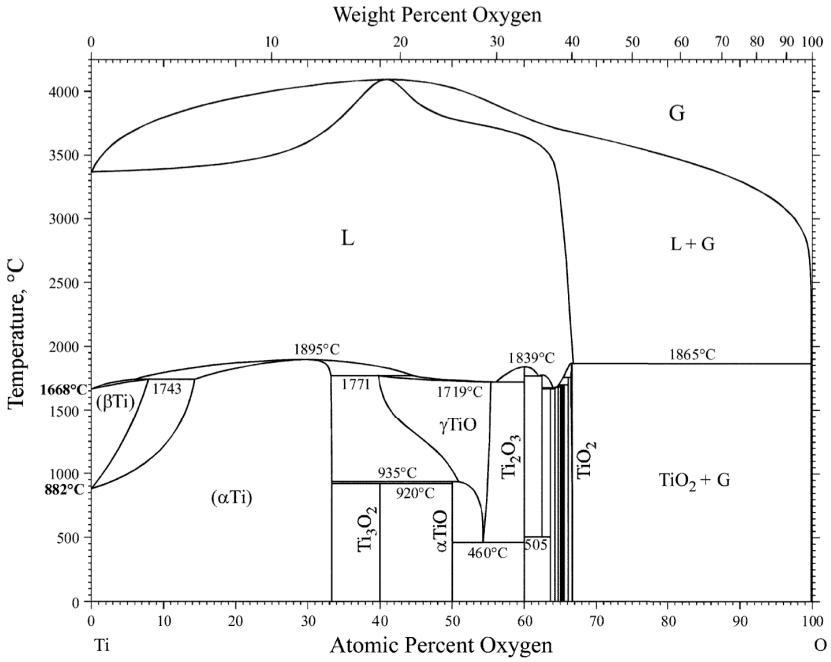

Figure 3.1: Phase diagram for the Ti–O system [40].

The most commonly cited sub-oxides of titanium are Ti_2O_3 and TiO [41–44]. Ti_2O_3 crystallizes in the corundum structure whereas TiO crystallizes in the rock-salt (NaCl) structure at high temperatures. At lower temperatures, there is another form of TiO which has equal numbers of ordered Ti and O vacancies in the parent NaCl structure.

As the O to Ti ratio approaches 2, there is a series of phases with the general formula Ti_nO_{2n-1}. These are usually referred as the Magnéli phases and are modifications of the rutile structure [45]. They contain a series of plane defects, so-called CSPs (crystallographic shear planes), which cause the oxygen deficiency.

The highest oxide of titanium is the dioxide, TiO_2. Three phases that possess this composition exist, namely rutile, anatase and brookite. Brookite is a metastable phase that can be formed at low temperatures, but transform irreversibly to rutile at around 700 °C [46]. Anatase is a metastable phase for particles larger than ∼14 nm [47]. Below this size, due to lower surface free energy, anatase becomes the stable phase. Some fundamental properties of the three phases are summarized in Table 3.1.

Table 3.1: Some physical properties and crystal structural parameters of rutile, anatase and brookite phases of TiO_2 [20]

	Rutile	**Anatase**	**Brookite**
Unit Cell	Tetragonal	Tetragonal	Orthorhombic
Space Group	$P4_2/mnm$	$I4_1/amd$	$Pbca$
TiO_2 per Unit Cell	2	4	8
Lattice Parameters (Å)			
a	4.584	3.733	5.436
b			9.166
c	2.953	9.37	5.135
Band Gap (eV) [48]	3.01	3.20	3.13
Density (g/cm^3)	4.27	3.83	4.17

Although it is a metastable phase, anatase is technologically important, being more active than rutile in catalytic [49, 50], photocatalytic [51–53] and dye-sensitized solar cell applications [54, 55]. Nevertheless, the photocatalytically most active form of TiO_2 is a mixture of anatase and rutile [56], which has been found to consist of 60% anatase. Practical photocatalytic applications of TiO_2 are in the fields of waste water treatment, air purification, and self-cleaning windows. In dye-sensitized solar cells, a porous layer of TiO_2 nanoparticles coated on conducting glass becomes one of the electrodes. A light absorbing dye is adsorbed on its surface for harvesting visible light, since TiO_2 itself absorbs only in the UV region due to the large band gap. Photocatalytic and photovoltaic

applications of TiO_2 have more to do with the stability of the material rather than with its absorptivity of visible light.

Rutile has a broad range of applications, mostly related to its optical properties [20]. Due to its high refractive index, stability, non-toxicity and low cost, fine powders of TiO_2 are used as white pigments in paints and many other products. As single crystals, it is used in applications in optics, where a high refractive index and high transmission is desired.

In catalytic applications, TiO_2 is mostly employed as catalyst support rather than active phase. In the selective catalytic reduction (SCR) of NO_x with NH_3, which is utilized to reduce NO_x emissions from stationary power sources, a vanadium oxide catalyst that is supported on anatase is used [49]. WO_3 is added as a structural promoter to hinder the transformation to rutile at operation temperatures, which can be as high as 450 ℃ [49]. In the production of phthalic anhydride by oxidation of *o*-xylene, a similar catalyst composition is used (V_2O_5/TiO_2) where anatase is again the phase of the TiO_2 support [50].

3.2 Rutile–TiO_2(110)

3.2.1 Fundamental Issues Concerning the Experiments

Rutile is the thermodynamically stable phase over a broad range of temperatures and oxygen pressures. The equilibrium oxygen pressure at 1200 K for the $Ti_{20}O_{39}$(s)/rutile transition is around 10^{-20} atm [57].

In surface science studies, usually, rutile crystals which are slightly non-stoichiometric are utilized (TiO_{2-x} where $x \ll 0.1$ [20]). In such crystals, the imperfections are in the form of point defects rather than shear planes. The most abundant bulk defects in a slightly reduced rutile crystal are titanium interstitials, oxygen vacancies and titanium vacancies, which their relative equilibrium concentrations depend on the temperature and the oxygen partial pressure, as well as the concentration of impurities [20, 58, 59].

As already mentioned in the previous chapter, the use of slightly reduced rutile crystals in surface science experiments is a consequence of the need for conductive samples. While a stoichiometric crystal can be considered insulating for all practical purposes, slight reduction renders the crystal conductive enough for the techniques which require sample conductivity. Sputtering-annealing sequences, which are typically applied to clean the samples and make them conductive, increases the extent of reduction with each cycle, unless annealing is carried out in an oxygen ambient instead of UHV. Annealing in oxygen for long enough time can in principle oxidize the crystal to full stoichiometry, which is not desired. The oxidation and reduction of samples should be balanced if a crystal is preferred to have roughly constant non-stoichiometry.

An important issue regarding reoxidation of TiO_2 crystals is the following. It has been shown that the surface reoxidation of an ion-sputtered surface during UHV annealing is a result of Ti cations diffusing into the bulk, rather than O anions diffusing to the surface [60]. Shortly after that finding, STM images taken during annealing in O_2 ambient,

revealed that the reoxidation mechanism in O_2 is the diffusion of Ti cations from the bulk to the surface and their oxidation to form new layers of TiO_2 [61]. Such a reoxidation mechanism involves growth of partial layers, which may be quenched, and hence stabilized at room temperature, if cooling is fast enough in UHV. A similar result would be obtained if cooling is slow but is performed in oxygen ambient. TiO_x islands that form as a result of such a treatment have been investigated in the literature [62, 63]. Flat terraces that are free of such TiO_x structures are preferred in most cases, especially for STM experiments. For this reason, the final annealing treatment of a TiO_2(110) crystal is usually performed in UHV.

Clean surfaces of UHV annealed and slightly reduced TiO_2(110) crystals are non-polar and have a bulk-like termination [64, 65]. A bulk terminated space filling model, which for many purposes is a good representation of the real surface, is shown in Figure 3.2(a). Geometrically, the surface is flat except for the protruding bridging oxygen atoms. At the surface, there are 2 types of under-coordinated sites: i) 5 fold coordinated titanium atoms (5cTi), which form a row in the [001] direction, ii) bridging oxygen atoms, which are two-fold coordinated (2cO) and form rows also in the [001] direction. Chemically, 5cTi atoms are Lewis acids and 2cO atoms are Lewis bases.

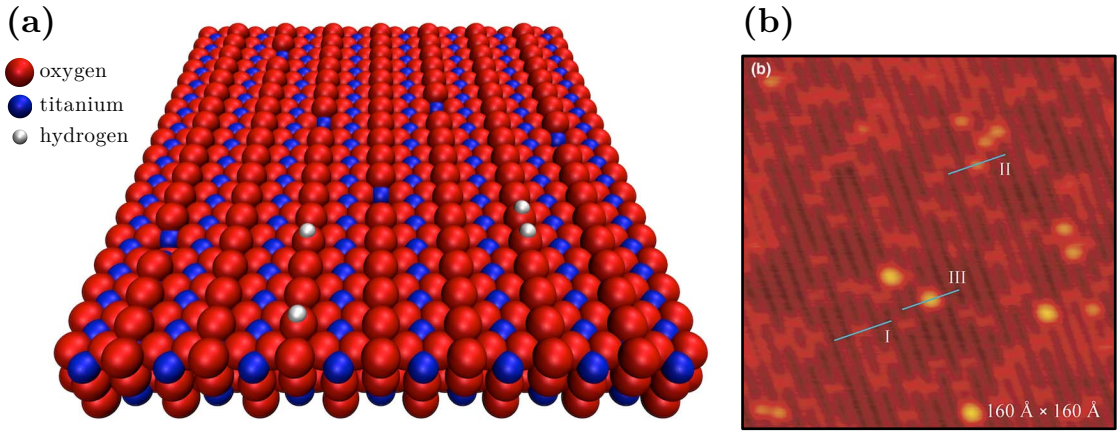

Figure 3.2: TiO_2(110) surface: (a) space filling model based on bulk termination, showing bridging oxygen vacancies and hydroxyl groups (that form as a result of water adsorption). (b) STM image from [66] where oxygen vacancies (I), hydroxyls (II) and double-hydroxyls (III) are identified. Image size is 160×160 Å^2, ΔU = +1.25 V, I_t = 0.1 nA.

On a typical, slightly reduced, TiO_2(110) surface 2–10 % of the bridging oxygen atoms are missing, depending on the degree of reduction of the bulk of the crystal. These vacant sites are named bridging oxygen vacancies (BOV) and they are active sites for dissociative water adsorption at room temperature [66–69]. In the adsorption of water at BOVs, the oxygen atom fills the vacancy and one hydrogen atom is transferred to a neighbouring bridging oxygen. The final structure is a pair of hydrogen atoms adsorbed

onto two neighbouring oxygen atoms, which is usually termed as a “hydroxyl” pair. At room temperature, diffusion of these hydrogen atoms is relatively fast, such that isolated hydroxyls are formed. In Figure 3.2(a), BOVs, isolated hydroxyls and hydroxyl pairs are illustrated in the surface model, whereas Figure 3.2(b) shows how these species typically appear in STM images. STM scanning of TiO_2(110) surfaces are usually performed in constant-current mode, with a gap voltage between +1.2 and +1.5 V and a tunnelling current in the range of 0.1 nA. The images acquired using these parameters show the rows of 5-fold coordinated titanium atoms as bright lines extending in the [001] direction, whereas the bridging oxygen rows as dark lines. Oxygen vacancies are imaged as bright features connecting two bright rows. Isolated hydroxyls are also imaged as bright features at the same position but brighter than BOVs. Hydroxyl pairs usually canÕt be resolved, thus they appear like larger and brighter hydroxyls.

3.2.2 Experimental Data of the TiO_2(110) Substrate

The starting point for each mixed layer preparation was a clean TiO_2(110) surface. In this section, typical data collected from a clean surface with our experimental setup are presented.

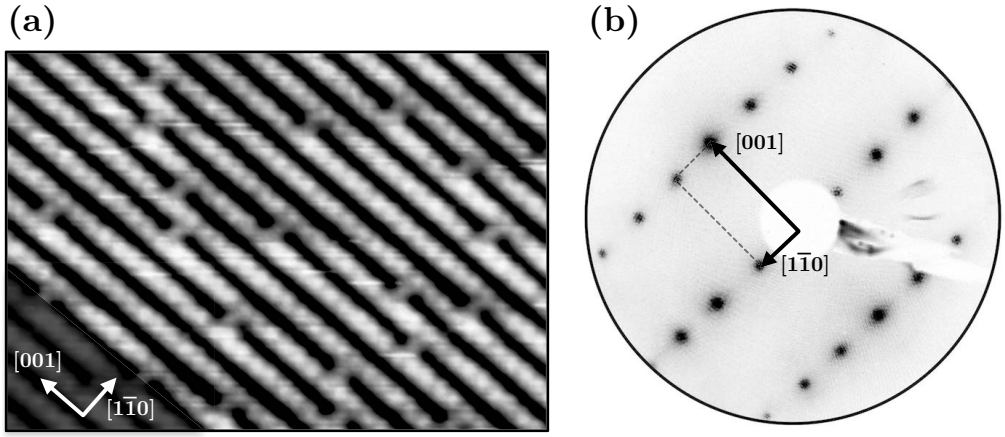

Figure 3.3: (a) STM image of a clean TiO_2(110) surface, showing a region of 95 × 66 Å^2 size. The acquisition parameters are: $\Delta U = +1.3$ V, $I_t = 0.1$ nA. (b) LEED pattern from a clean TiO_2(110) surface, acquired with a primary electron beam energy of 100 eV.

Figure 3.3(a) is an STM image of a clean TiO_2(110) surface which was acquired with our system. The scanned area contains bridging oxygen vacancies but is free of hydroxyls. Figure 3.3(b) shows the LEED pattern of a clean TiO_2(110) surface from a different crystal. The orientations of the LEED pattern and the STM image are consistent with each other.

Figure 3.4 shows a survey XPS spectrum of a clean TiO_2(110) surface. Such spectra were taken in order to check the presence of various contaminants with a reasonable expenditure of time (∼10 minutes). O1s and Ti2p produce intense peaks at 530.3 and 464.8/459.0 eV

respectively. The most intense satellites which can be observed for the Ti2s, O1s and Ti2p lines are at 10–13 eV higher binding energies. Another prominent group of satellites are the x-ray satellites of the Al source, which produce peaks at ∼10–12 eV lower binding energies [70]. The minor Ar2p peak at around 242 eV, that is due to residual argon from sputtering, is minimized after annealing the sample in oxygen.

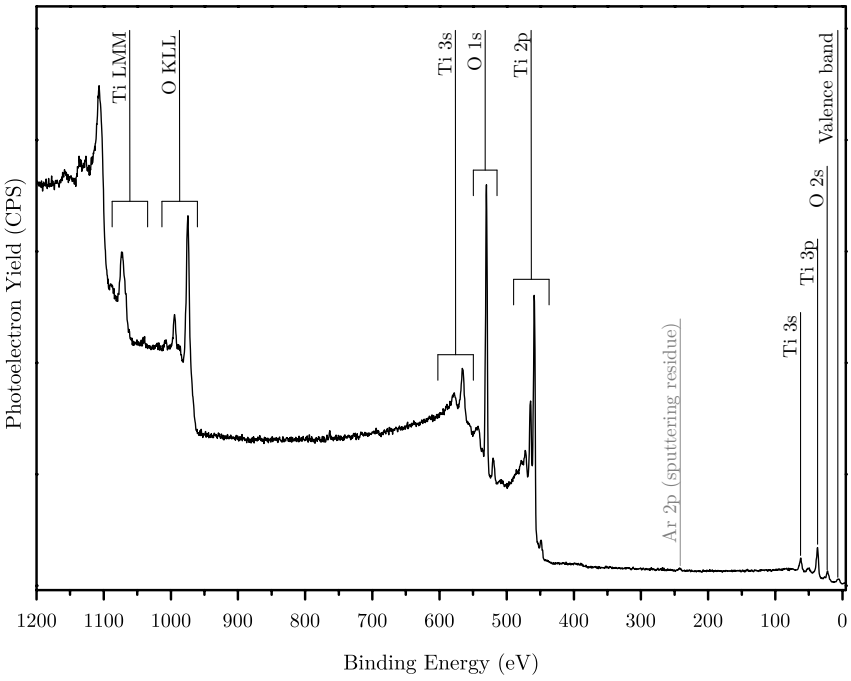

Figure 3.4: A survey XPS spectrum of a clean $TiO_2(110)$ surface, measured using the Al Kα source (1486.6 eV) and a pass energy of 100 eV. Peaks are labelled with the corresponding energy levels or Auger transitions of titanium and oxygen. Embedded argon atoms from the sputtering process contribute a small peak also.

3.3 The Molybdenum–Oxygen System

In the molybdenum-oxygen binary system, starting from molybdenum metal and increasing the oxygen content, the first stable phase is the dioxide (MoO_2) [71, 72]. This phase, although structurally similar to TiO_2, does not possess any Magnéli phase. Several intermediate phases (e.g. Mo_4O_{11}, Mo_9O_{26}) form with increasing oxygen content. The highest oxide of molybdenum is MoO_3. A calculated Mo–O phase diagram in the composition range $x_O = 0.60$–0.75 [72] is presented in Figure 3.5. Mo_9O_{26} is a member of the Magnéli phases of MoO_3 which are based on periodic CSPs (as in the case of TiO_2).

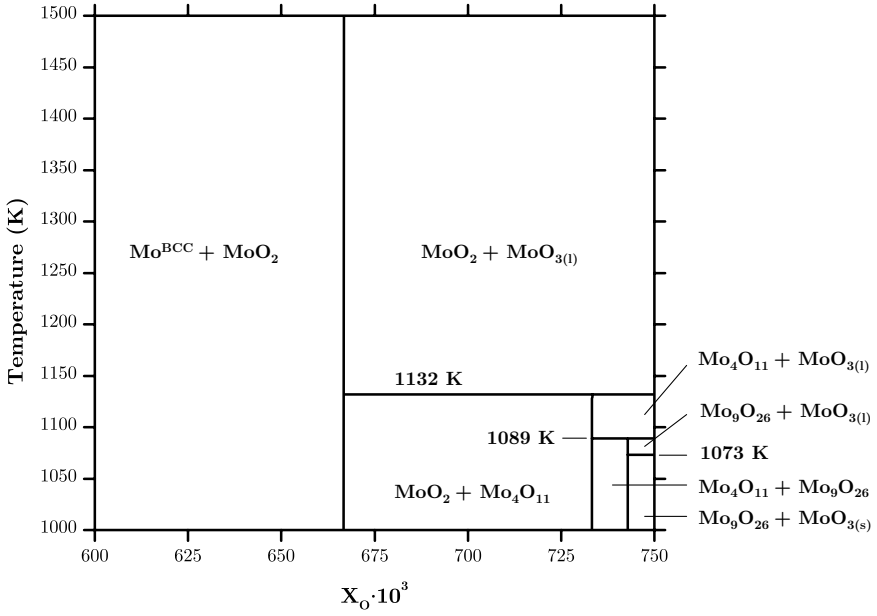

Figure 3.5: Molybdenum–oxygen phase diagram in the composition range $x_O = 0.60$–0.75 [72].

MoO_2 has a rutile-like structure which is in the monoclinic lattice system [73]. All the Mo atoms in MoO_2 are equivalent and there are two types of non-equivalent oxygen atoms with 1:1 abundance. In Figure 3.6, a section of bulk MoO_2 is illustrated. The section is selected such that the exposed surface is analogous to the $TiO_2(110)$ surface. An important structural feature of MoO_2 is the variation of the nearest distance between molybdenum atoms. A Peierls-type instability leads to the pairing of Mo atoms along the a-axis of the lattice [74]. The pairing effect can easily be seen from Figure 3.6. The two shortest distances then become 2.5 Å and 3.1 Å.

MoO_3 has a layered structure, which is made up of bilayers [76–78]. Each bilayer is coordinatively saturated and the interactions between them are due to Van der Waals forces. Each layer of the bilayer consists of corner-sharing octahedra and each of these octahedra shares two edges with two octahedra from the other layer of the bilayer. All the

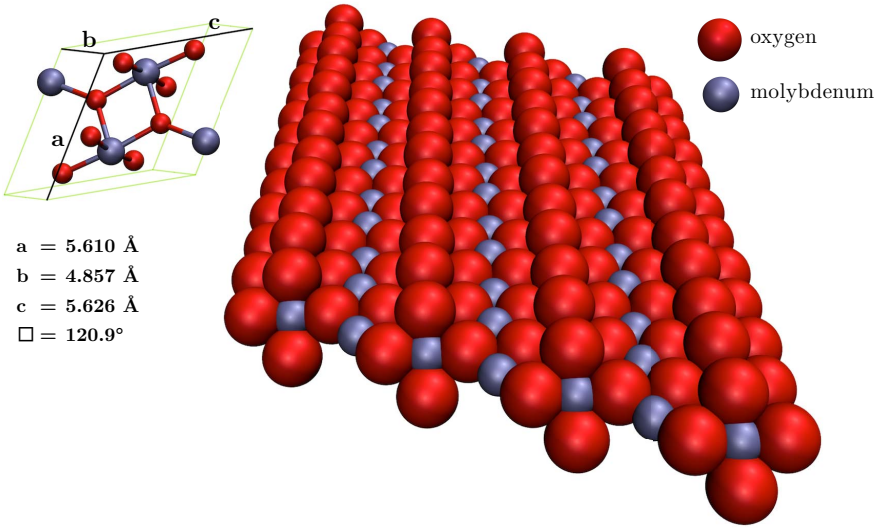

Figure 3.6: A section from the MoO_2 bulk structure, which is analogous to the (110) surface of TiO_2. The unit cell, which belongs to the monoclinic crystal system and contains four formula units, is given on the left. There are two Mo–Mo nearest distances (2.5 and 3.1 Å), which are distinguishable in the image by naked eye. Data from [75].

Mo atoms in the structure are equivalent, whereas there are three types of non-equivalent O atoms with 1:1:1 abundance. The structure of MoO_3 is illustrated in Figure 3.7. Since the bilayer is coordinatively saturated, one bilayer can in principle be stabilized if abstracted from the rest of the crystal. In the literature, there is a collection of works [79–83], which demonstrate the synthesis of the half of the bilayer (monolayer) on a Au(111) substrate. It has been claimed on theoretical grounds, that the layer is stabilized by the image charge in the Au(111) substrate, and that image charge serves as the other half of the bilayer [80].

The thermodynamic stabilities of MoO_2 and MoO_3 in UHV may be relevant for the understanding of the presence or absence of a specific phase in our experiments. The equilibrium constants for the reactions:

$$2\,MoO_2(s) + O_2(g) \rightleftharpoons 2\,MoO_3(s) \qquad (1)$$

$$Mo(s) + O_2(g) \rightleftharpoons MoO_2(s) \qquad (2)$$

have been calculated from the Gibbs energy data of each species in the 300–1000 K range [85]. In Figure 3.8, the equilibrium pressure of oxygen is plotted as a function of temperature for reaction 1. For reaction 2, the curve goes through pressures so low that it is not seen in this scale. In the plotted range, pressures above the line favour the MoO_3 phase, whereas pressures below the line favour the MoO_2 phase. It should be noted that this calculation is based on a very idealized situation in which the phases that are known

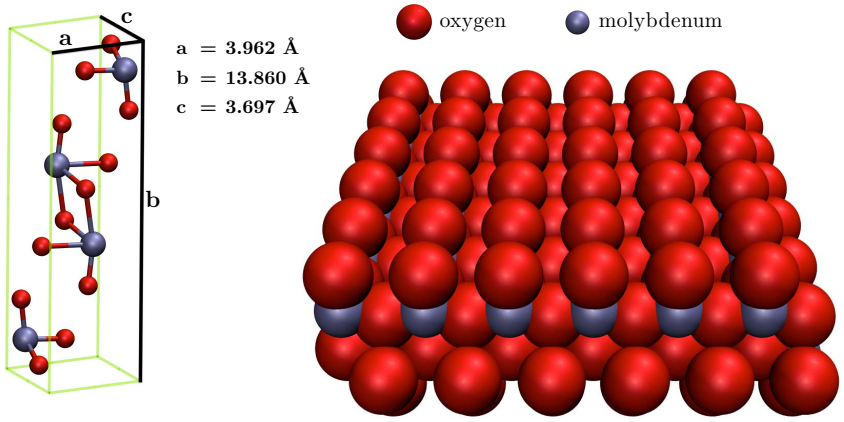

Figure 3.7: Structure of bulk MoO_3. The unit cell, which belongs to the orthorhombic crystal system and contains four formula units, is given on the left. The space filling model on the right is a bilayer, which is coordinatively saturated. Data from [84].

to exist between MoO_2 and MoO_3 (e.g. Mo_4O_{11}, Mo_9O_{26}) are omitted. Furthermore, the contribution of surfaces to the total Gibbs energy is neglected, which is important in the case of small particles and thin layers. Nevertheless, it is calculated from rather precise, reliable data and is thus a good starting point to compare stabilities as long as the limitations are borne in mind. The calculated curve for the MoO_3–MoO_2 equilibrium shows that MoO_3 is the thermodynamically stable phase in UHV conditions at room temperature and somewhat above. Although thermodynamics predicts the stability of MoO_3 in UHV, it does not guarantee its formation during layer preparation. If the activation barriers for the formation of the MoO_3 phase are high, it may not form in the given experiment. Once MoO_3 is formed, it will be stable. One additional piece of information in Figure 3.8 is the vertical grey line at 670 K. This temperature is the onset of MoO_3 sublimation from MoO_3 films grown on Au(111), as measured by TPD in the work of Guimond [85]. This means that bulk MoO_3 can not be stabilized above ∼670 K and the calculated equilibrium line is not meaningful anymore.

Molybdenum has important uses in industrial catalysis, but the catalysts that contain molybdenum in an oxide form are all complex solids that contain other metal ions in significant proportions. A Mo–Fe mixed oxide catalyst is used in the oxidative dehydrogenation of methanol to formaldehyde. Formaldehyde is a very important raw material, used in the production of numerous chemicals, with an annual global production of 20–30 million tons [87]. The catalyst is bulk iron–molybdate with excess MoO_3 which is required to replenish the MoO_x that is lost via sublimation [88].

An alumina supported molybdate catalyst is used in the metathesis step of the multistep SHOP (Shell Higher Olefins Process) process, which converts ethylene to higher alkenes [89]. Molybdate containing catalysts are used in the propene ammoxidation to acrylonitrile

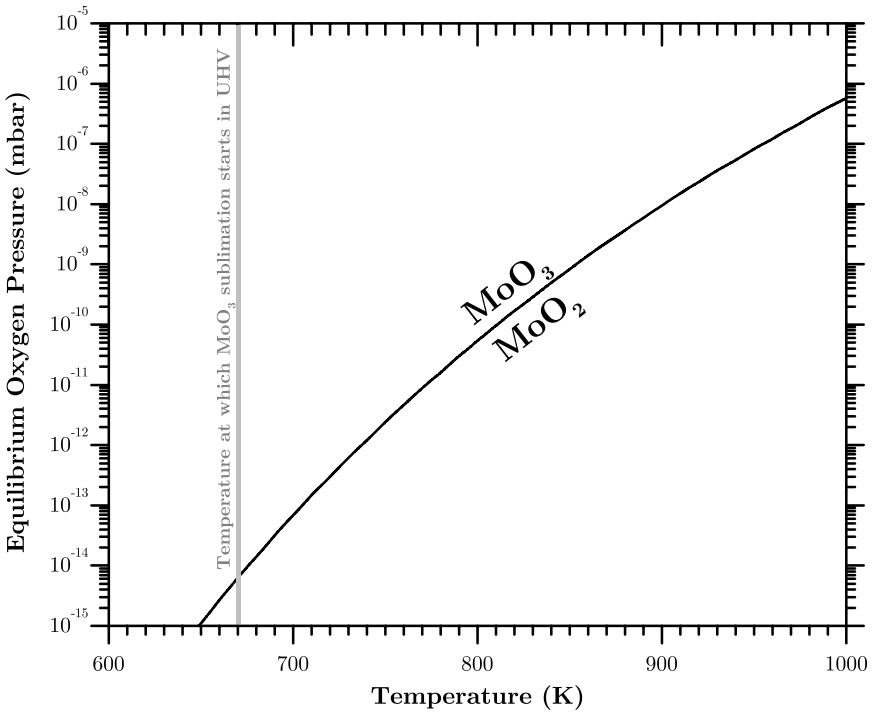

Figure 3.8: Regions of stability for solid Mo, MoO_2 and MoO_3 in the presence of oxygen, as calculated from bulk thermochemistry data [85]. The calculation omits intermediate phases with stoichiometry between MoO_2 and MoO_3. The curve that divides MoO_2 and Mo regions is outside the scale of the plot. The vertical grey line marks 670 K, which has been observed to be the onset of sublimation for a MoO_3 layer in UHV in the TPD experiments by Guimond [86]. Details of the calculation are given in appendix B.

and oxidation to acrylic acid. These catalysts are complex materials, containing oxides of other metals such as W, Bi, V, Sb, Sn, etc. [90, 91]. The annual production of acrylonitrile was 5.6 million tons in 2005, with 4% annual growth rate [91]. Acrylonitrile is the monomer of polyacrylonitrile (PAN), which is the material of many textile fibres and the raw material for the production of carbon fibres.

3.4 The TiO_2–MoO_2 System

Already in the 1950s, a short communication by Marinder and Magnéli reports on the poor miscibility of TiO_2 and MoO_2 [92]. The most recent phase diagram that has been published by Jacob et al. [93] is shown in Figure 3.9. According to this diagram, the solubility of TiO_2 in MoO_2 is almost negligible, while the solubility of MoO_2 in TiO_2 is ∼6% (mol/mol) at 1000 K and increases up to 37% at 1400 K. There are two types of solid solutions below 1560 K, $(S.S.)_1$ and $(S.S.)_2$, which converge to one phase above this temperature.

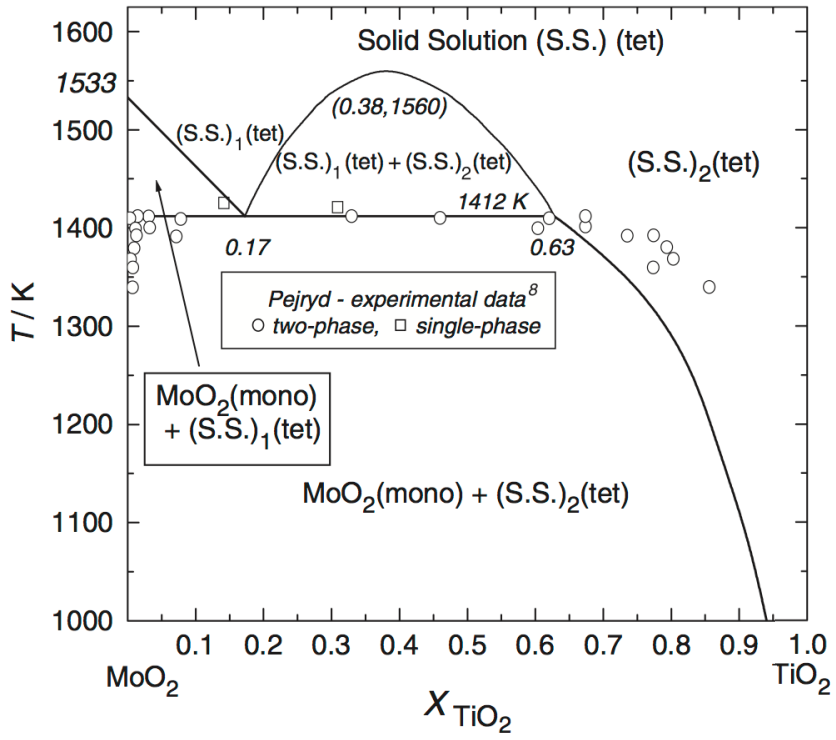

Figure 3.9: Phase diagram of the MoO_2–TiO_2 system, as given by Jacob et al. [93].

Experimentally not accessible due to slow kinetics at temperatures below 1000 K, the solubility of MoO_2 in TiO_2 would be even lower, close to ∼3% at 900 K, estimated by a simple linear extrapolation. The advantage of using physical vapour deposition (PVD) in preparing ultra-thin layers is that equilibrium limitations can be overcome by making use of slow diffusion kinetics at "low" temperatures. This permits to prepare metastable layers.

The MoO_2–TiO_2 system is not a catalytically important system, at least not in the industry. However, it is worth mentioning that MoO_3, similar to WO_3, can be used as a structural promoter to hinder the transformation of the more desired anatase phase

into rutile at high operation temperatures of anatase-supported catalysts [49]. A similar structure stabilizing function is also reported for gas sensors, where rutile TiO_2 is used [94]. There have been theoretical studies in the literature, which focus on the chemical properties of metal-doped TiO_2 [7, 8]. Mo-doped TiO_2 has been shown to be promising as an electrode material for the oxygen evolution reaction (the half-reaction of water electrolysis that produces oxygen) [8]. It has been found promising not because it is more active than the commercial electrodes but because it is extremely cheap.

4 STRUCTURE AND STABILITY OF MIXED LAYERS

4.1 Preparation Procedures and an Overview of Outcomes

In the fields of catalysis and surface science of oxides, many single-oxides as well as some popular multi-component oxides (e.g. Li/MgO [15, 95–100], VO_x/TiO_2 [101–111], $FeMoO_4$ [88, 112–114]) have already been studied in detail. The Mo–Ti mixed oxide system is not one of those. There are no well-established preparation recipes, which led us to trying different procedures for obtaining a good model system.

Almost all the preparations made in this work can be classified into six categories which are illustrated in Figure 4.1. These six procedures are drawn in a timeline representation where the horizontal axis is the time, and the deposition parameters (i.e. substrate temperature, gas ambience, Ti deposition and Mo deposition) are marked in certain time intervals.

Procedures 1 and 2 are quite similar. They both involve deposition of Mo and Ti in oxygen ambient gas (5×10^{-7} mbar) while the substrate is held at high temperature ($\geq$ 800 K). Post-annealing is performed in both cases, first in O_2 (1–3 minutes) then in UVH (2–5 minutes) at deposition temperature. In procedure 1, the depositions of Mo and Ti are simultaneous whereas in procedure 2, they are partially simultaneous with Mo being deposited for a shorter period of time than Ti. The time window for Mo deposition is taken such that it is in the middle of the Ti deposition period. In a hypothetical situation where MoO_x and TiO_2 mix in all proportions and diffusion does not occur, procedure 1 would produce a homogeneously mixed oxide layer containing Mo and Ti, whereas procedure 2 would produce a sandwich-like layer which stacks as $TiO_2/Mo_xTi_yO_z/TiO_2$. In reality, since MoO_2 and TiO_2 mix only a little (see Chapter 3), the resulting layers are far from these ideal constructs. This will be addressed in the following parts.

Procedure 3 is a recipe to prepare TiO_2 layers that contain Mo atoms mixed in them. Mo and Ti are deposited in UHV, in this order, one after the other. The layer is only slightly oxidized due to the interaction with the TiO_2 substrate. Complete oxidation is performed by annealing it in an O_2 ambient for 15 minutes (in front of the gas doser, with an effective $\sim5\times10^{-7}$ mbar O_2 pressure on the sample surface). A final annealing step is performed in UHV at 800 K for 15 minutes.

Procedure 4 is a relatively simple procedure which involves deposition of Mo onto the substrate at room temperature in a 5×10^{-7} mbar O_2 ambient. Post-annealing is performed in UHV at 800 K for 5 minutes. This procedure was expected to result in minimum mixing of Mo into TiO_2.

Procedure 5 is similar to procedure 4. It is taken directly from the work of Domenichini

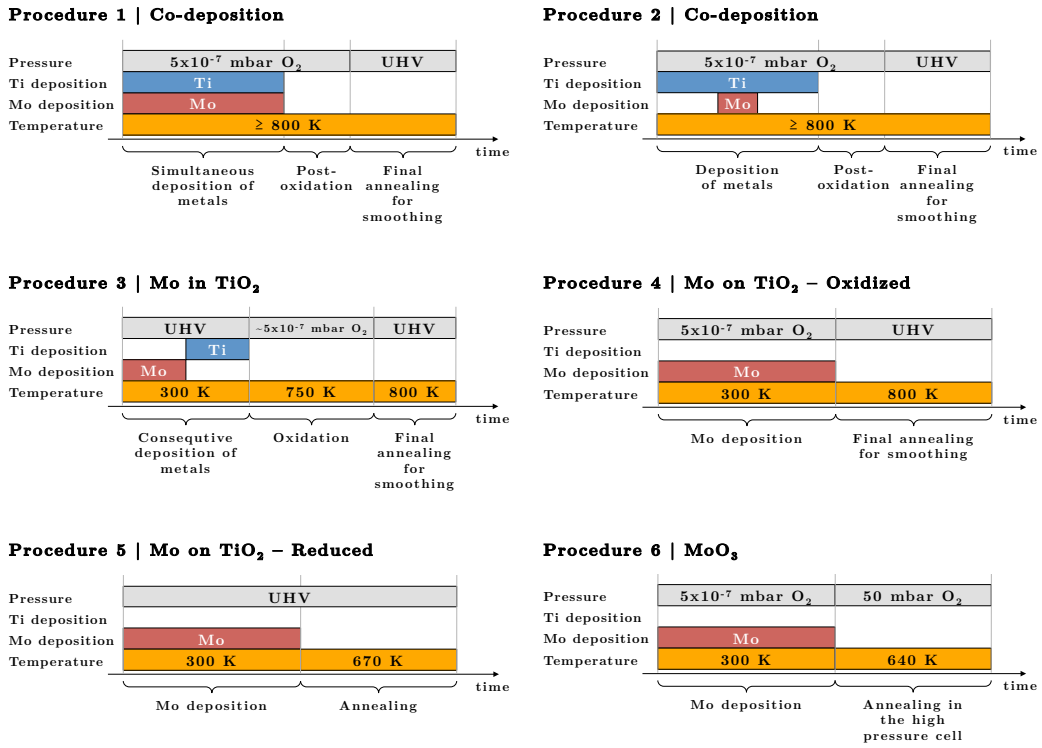

Figure 4.1: Timeline representations of the six procedures which were used to prepare the layers studied in this work.

et al. [115] in order to reproduce their results and compare with ours. Mo is directly deposited onto the substrate at room temperature but in UHV this time. Post annealing is carried out at 670 K in UHV for 10 minutes.

Procedure 6 is employed for growing thick, bulk-like MoO_3 layers. Mo is deposited in an O_2 ambient (5×10^{-7} mbar) at room temperature. Post annealing must be carried out in much higher oxygen pressure to get the MoO_3 phase. This is accomplished in the high-pressure cell of the setup. The sample is transferred to this cell, isolated from the UHV chamber and annealed in 50 mbar O_2 at 640 K. The sample is cooled down after pumping out the oxygen and then transferred back to the main chamber.

One parameter was found to be especially useful for comparing layers from different preparations. This is the ratio of the Mo concentrations as calculated from XPS at different sample–analyser configurations. The XPS measurements made in this work have been performed sometimes in only one of the two selected configurations, but usually in both. These configurations, as depicted in Figure 2.4, are, (i) normal: the surface normal of the sample is parallel to the analyser axis, (ii) grazing: the angle between the surface normal of the sample and the analyser axis is 70°. The Mo concentration, expressed in the number of Mo atoms per 100 metal (Mo+Ti) atoms, is calculated from Mo3d and Ti2p spectra

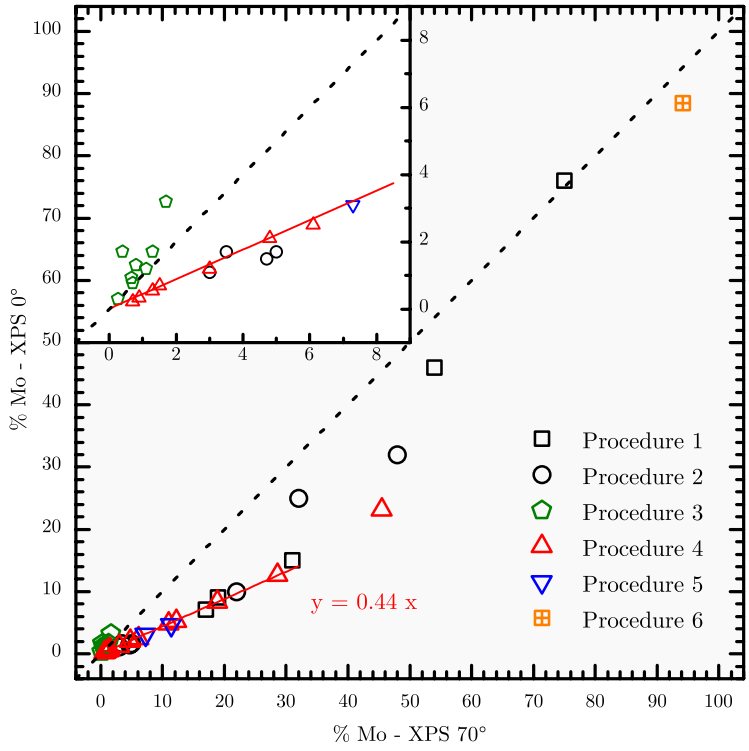

Figure 4.2: Correlation of Mo concentrations as quantified by XPS using 70°(x-axis) and 0°(y-axis) electron exit angles for layers prepared according to procedures 1 to 6. The inset shows the same data up to 9% Mo concentration.

taken at these two configurations, and the two numbers are put into the scatter plot shown Figure 4.2. In the plot, the x-axis is for the Mo concentration obtained in grazing configuration and the y-axis for the Mo concentration obtained in normal configuration. A sample calculation of the Mo concentration is given in appendix A.

Each preparation made according to one of the explained procedures is represented by a single point in Figure 4.2. The dashed line marks the 1:1 ratio, which represents a situation where the film is homogeneous through the probing depth ($\sim 3\lambda$). Layers that contain Mo concentrated at the surface fall below this line whereas layers that contain Mo only below the surface usually fall above the line.

Layers prepared according to procedure 3 usually fall above the 1:1 line as expected. The concentration of Mo calculated from normal configuration is higher than or equal to that from grazing configuration. The reverse is true for procedures 4 and 5 since Mo is deposited right onto TiO_2. Points that represent these surfaces lie below the 1:1 line, and, assuming all the deposited Mo stays on the surface, form the theoretical limit below which a point can not be. This limit is marked by a red line in Figure 4.2, and is linear at low Mo concentrations. The line deviates from linearity at higher concentrations where photoelectrons from Mo atoms can be attenuated by other Mo atoms. A thick enough

MoO_x layer can block all the Ti signal from the substrate and be seen as 100% Mo in both configurations. An example is the point that represents the thick MoO_3 layer prepared by procedure 6.

The most important fact that is evident from Figure 4.2 is that at low Mo concentrations, the points that belong to procedures 1 and 2 fall onto the border line that is marked by procedures 4 and 5. This suggests that the distributions of Mo along the surface normal in preparations 1, 2, 4 and 5 are very similar. If the oxidation state of Mo is also taken into account, the procedures 1, 2 and 4 form almost identical layers. This implies that most of the molybdenum deposited in procedures 1 and 2 ends up on the surface, contrary to the intention of homogeneous mixing. At higher Mo concentrations ($>\sim 30\%$), the points that represent procedures 1 and 2 fall above the aforementioned border line, due probably to the different surface structures of these layers (large agglomerates, etc.).

4.2 Procedure 1

Preparations made according to procedure 1 with low Mo concentrations produced results similar to those produced by just depositing Mo on the substrate in an O_2 ambient (i.e. procedure 4). These layers gave LEED patterns almost identical to the one from the clean $TiO_2(110)$–(1×1) substrate. At higher concentrations of Mo, the differences were more evident. Figure 4.3 shows LEED patterns of two layers, with 54% and 75% Mo content (XPS, 70°), prepared according to procedure 1. The pattern from a clean TiO_2 surface is also shown for comparison. The LEED pattern of the layer with 54% Mo is nearly identical to that of the substrate. The spot intensities are weaker and the background intensity is slightly higher. The layer with 75% Mo do not show sharp spots, but a high background and diffuse streaks along $[1\bar{1}0]$ direction, which implies some order in [001] direction.

The layer with the LEED pattern given in Figure 4.3(c) has been subjected to a series of annealing treatments. The LEED patterns and XPS spectra are presented in Figure 4.4 and Figure 4.5. In the beginning, the layer contains 75% Mo as measured by XPS in both normal and grazing configurations. This indicates that Mo and Ti atoms are distributed homogeneously throughout the layer. After annealing the layer in UHV at 900 K for 10 minutes, there is still no LEED pattern, and all the XPS spectra look qualitatively the same. The only difference is in the Mo concentration, which increases to 81% (for both normal and grazing configurations).

The LEED pattern in Figure 4.4(c) forms after annealing the layer in UHV at 950 K for 10 minutes. The pattern is a $c(2 \times 2)$ superstructure over the $TiO_2(110)$–(1×1) pattern. The reciprocal-space lattice vectors for the (1×1) and $c(2 \times 2)$ patterns are denoted as (a_1, a_2) and (b_1, b_2) respectively. The real-space lattice vectors which correspond to these reciprocal-space lattice vectors are shown on the surface model given at the bottom-centre of the figure, and are named with capital letters. The annealing at 950 K does not lead to any change in the Mo concentration, but the Mo3d and O1s spectra change qualitatively. Annealing this layer at 950 K in $\sim 1\times10^{-6}$ mbar O_2 results in a decrease of the Mo concentration, which becomes 68% (grazing) and 74% (normal). The LEED

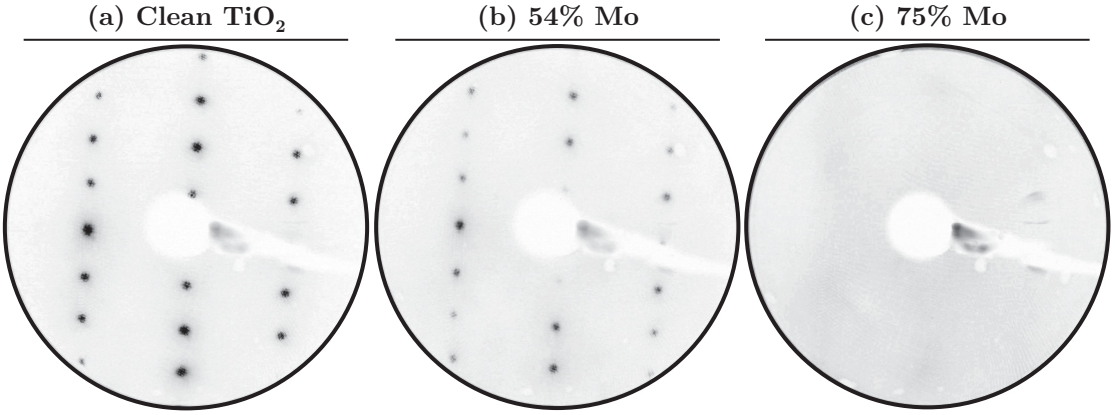

Figure 4.3: LEED patterns of (a) clean TiO_2, (b) a mixed layer with 54% Mo (procedure 1; $T = 870$ K; thickness: 33 Å), (c) a mixed layer with 75% Mo (procedure 1, $T = 800$ K; thickness: 33 Å). The primary electron beam energy is 100 eV. Coloured images of the LEED patterns were converted to greyscale and inverted with subsequent contrast enhancement, all using the same procedure.

pattern remains unchanged.

The $Mo3d_{5/2}$ binding energy in Figure 4.5(a) is 228.7 eV. This is in perfect agreement with the binding energy obtained by Werfel and Minni for single crystalline MoO_2 but it is ∼0.7 eV lower than some other commonly cited binding energies for MoO_2 [116, 117]. It is clear that the composition of the layer is close to MoO_2. How Ti is mixed into the layer is not clear. The Ti^{4+} signal comprises most of the Ti2p intensity although the contribution of Ti atoms with a lower oxidation state is clearly visible. Annealing at 950 K in UHV leads to the oxidation of the layer, as evidenced by the shift of the Mo3d lines to higher binding energies. The oxidation probably proceeds via the diffusion of oxygen atoms from the substrate to the layer since oxygen is not supplied externally nor does a disproportionation reaction take place within the layer. In addition to the shift of the main line, a new signal emerges at ∼230.8 eV ($Mo3d_{5/2}$). In the literature, such a binding energy has been associated with Mo^{4+} ions in an environment different from the environment of Mo in MoO_2 [116, 118, 119], or Mo^{5+} [120–122]. Mo3d spectra of compounds where Mo is in more than one oxidation state are usually complex and the components have to be deconvoluted using certain assumptions. Symmetric peak shapes have been preferred in the earlier studies due to their ease of use, although this is not always appropriate. There is no consensus yet on a complete, unambiguous correlation between Mo3d binding energies and chemical environments for molybdenum compounds.

Figure 4.5(d) shows the XPS spectra from the layer after it has been annealed in $\sim 1 \times 10^{-6}$ O_2. The spectra look qualitatively the same as the previous ones. The effect of the oxygen treatment is the loss of molybdenum. The loss is more prominent nearer to the surface (XPS–grazing, from 81% to 68%) as compared to deeper layers (XPS–normal, from 81% to 74%). This implies that molybdenum is lost from the surface. It has already been

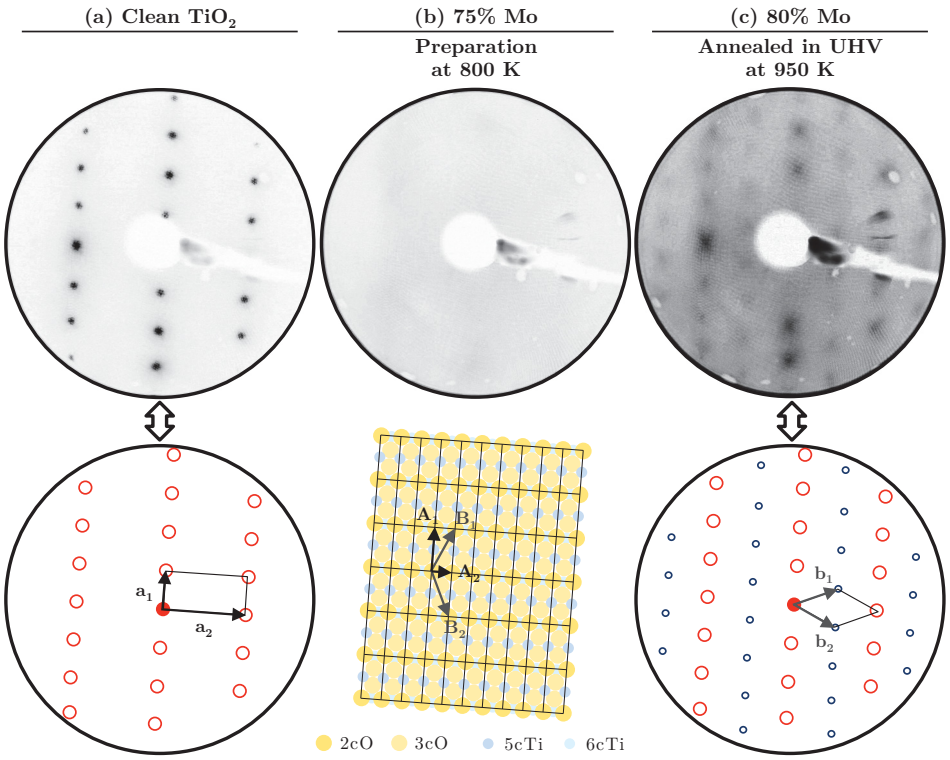

Figure 4.4: The LEED patterns of (a) a clean $TiO_2(110)$–(1×1) surface, (b) a mixed layer with 75% Mo content (procedure 1, $T = 800$ K; thickness: 33 Å), (c) the layer in (b) after annealing treatments in UHV at 900 and 950 K for 10 minutes each. The primary-beam energy is 100 eV for all cases. For (a) and (c) schematically reproduced patterns are shown under each image for a better visualization. The reciprocal-space lattice vectors are given in these patterns. A model of the $TiO_2(110)$ surface is given at the bottom-centre together with the real-space lattice vectors derived from the patterns.

mentioned in the previous chapter that MoO_3 is volatile at high temperatures [86, 123]. Therefore, the observed loss from the surface should be due to oxidation of the surface to MoO_3 and subsequent sublimation.

The formation of the $c(2\times2)$ superstructure after the annealing at 950 K is the one and only case in this work where a LEED pattern different from that of the substrate forms. The pattern is consistent with the rutile-like surface structure of $MoO_2(011)$ depicted in Figure 3.6. The spots are diffuse, indicating that ordered domains are small.

Mo–Ti mixed oxide layers usually contain a mixture of Mo (and to some extent Ti) oxidation states as evidenced by XPS. Figure 4.6 shows XPS spectra from a 50–60 Å thick layer, containing 48% Mo, taken using synchrotron radiation at normal and grazing (80°) configurations. Spectra (a) are from the layer right after preparation. At least three

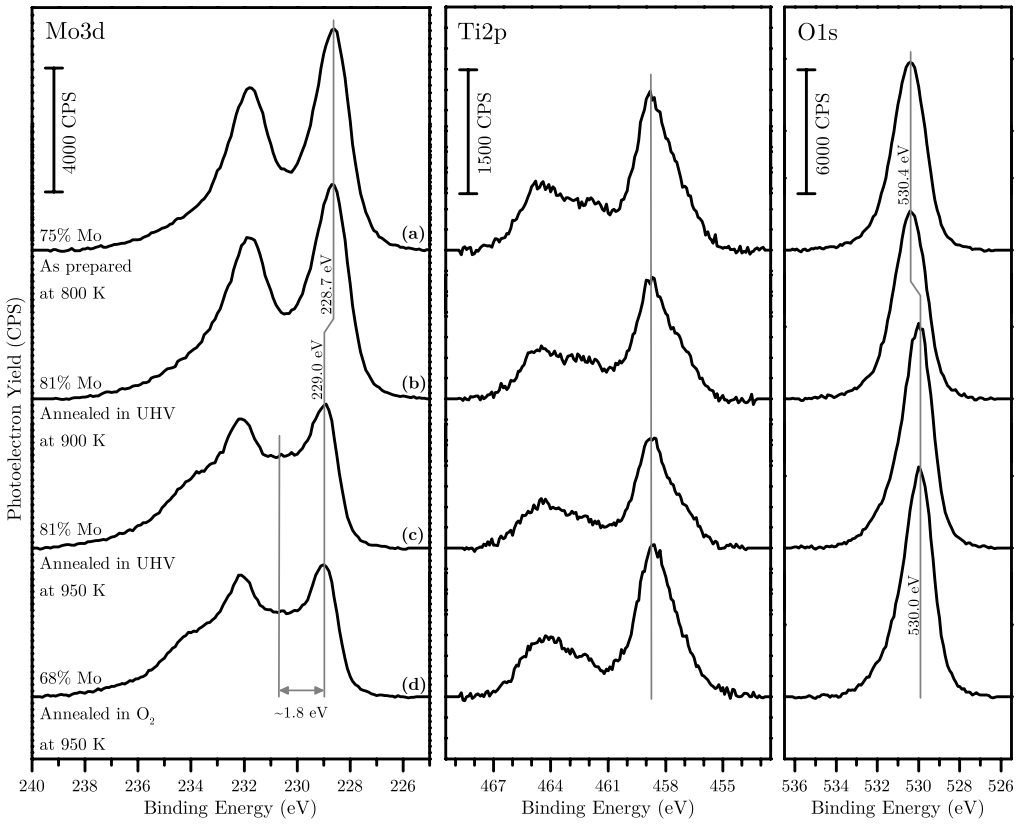

Figure 4.5: XPS spectra (normal configuration) from a 33 Å thick layer, initially containing 75% Mo (XPS, 70°), prepared at 800 K. (a) the as-prepared layer, (b) after annealing in UHV at 900 K for 10 minutes, (c) after annealing in UHV at 950 K for 10 minutes, (d) after annealing in $\sim 1 \times 10^{-6}$ mbar O_2 at 950 K for 10 minutes. The peak maxima are indicated by grey lines.

different doublets can be identified in the Mo3d spectrum owing to the high resolution which is not possible to attain with the laboratory source. These three species are marked with the three line pairs drawn in blue, green and red. The blue and green doublets have been assigned to Mo^{6+} and Mo^{4+} species respectively. The red doublet has the same binding energies as the main peaks observed in Figure 4.5(a) and (b), which were assigned to an unknown structure close to MoO_2 in composition. This state will be denoted by Mo^{n+}. Comparison of the Mo3d spectra taken in normal (0°) and grazing (80°) configurations imply that the Mo^{6+} species are nearer to the surface. The Ti2p spectrum shows a small shoulder towards lower binding energies, indicative of reduction. The O1s peak has prominent intensity to the higher binding energy side of the main peak.

Annealing the sample in UHV at 800 K for 10 minutes makes almost no difference, as can be seen from spectra (b) of Figure 4.6. After annealing in 1×10^{-6} mbar O_2 at 800 K for 20 minutes, the Mo concentration drops to 14% and the ratio of Mo^{6+} to Mo^{4+} increases.

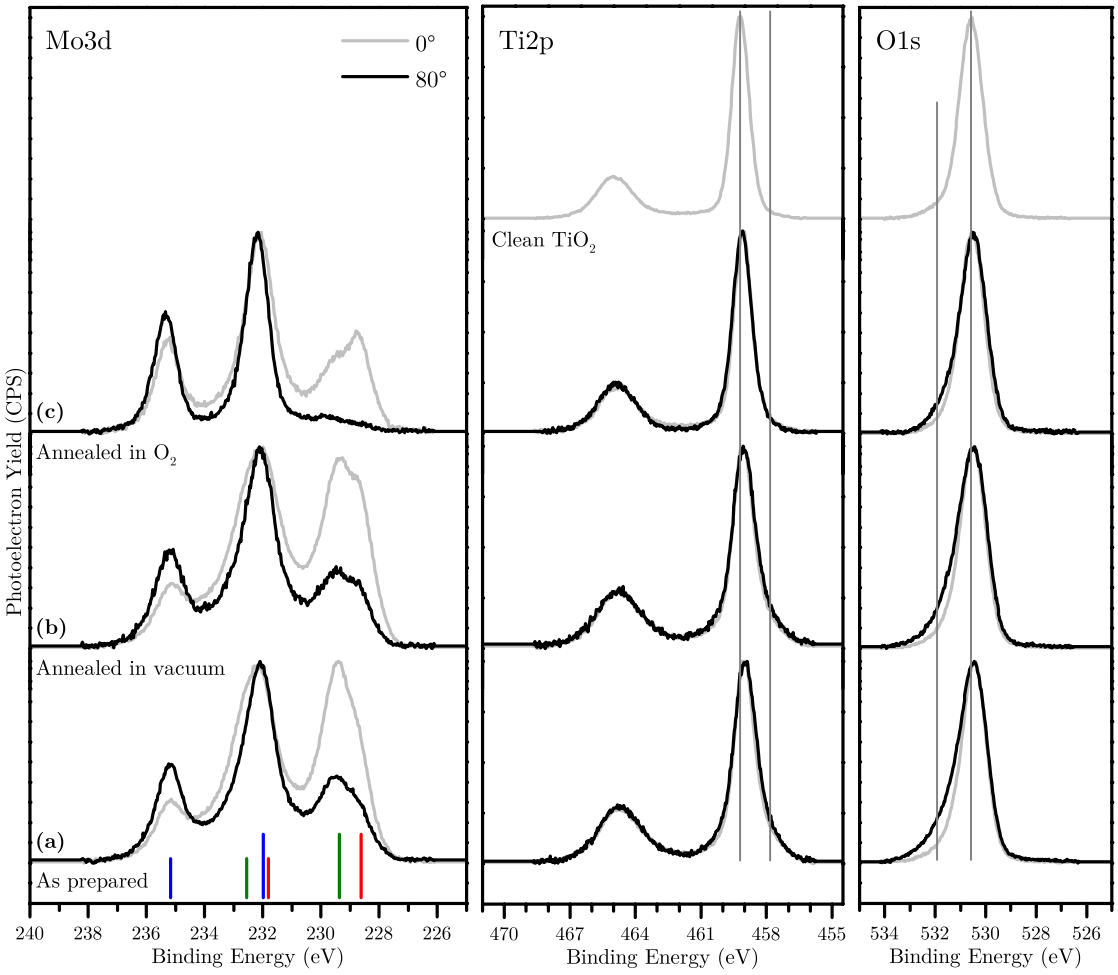

Figure 4.6: High resolution XPS spectra of a Mo+Ti mixed oxide layer prepared according to procedure 1 at 800 K. The layer thickness is about 50–60 Å and the Mo/Ti ratio is about 10% as estimated from the calibration of metal deposition rates using a quartz microbalance. XPS data taken with 0°electron exit angle yield a Mo content of 48% for the as-prepared layer. The effects of treating the layer in UVH and in O_2 ambience can be followed from (a) to (c). (a) As prepared layer, (b) after annealing in UHV at 800 K for 10 minutes, (c) after annealing in 1×10^{-6} mbar of O_2 for 20 minutes. All the curves were normalized to their maximum intensities after subtraction of a Shirley background. The photon energies used for the Mo3d, Ti2p and O1s spectra are 330 eV, 460 eV and 630 eV respectively.

In the very surface sensitive grazing-configuration spectrum, Mo^{6+} becomes almost the only species present. In the Ti2p spectrum, the shoulder on the low binding energy side is reduced significantly. Hence, the oxidation treatment converts all the metal ions in the system to their highest oxidation states, the exception being the Mo^{4+} and Mo^{n+} species which are still observed in the 0° spectrum. This signal originates from layers below the surface, which may be related to i) Mo^{4+}/Mo^{n+} ions that are mixed in TiO_2, ii) relatively large MoO_2 or similar particles whose surface layers contain Mo^{6+} ions, or both.

Going from (b) to (c) in Figure 4.6, the changes in the 0° Mo3d spectra suggest that the Mo^{4+} and Mo^{n+} species are affected differently by the oxidation process. After annealing in O_2, Mo^{n+} dominates Mo^{4+}. This suggests that the species indicated with the green lines is more prone to oxidation than the other one.

The decrease of the concentration of molybdenum during annealing in UHV or O_2 ambient is something that has been encountered in many other experiments throughout this work. It is appropriate to address this issue at this point. The most plausible explanations for this phenomenon are: i) sublimation of molybdenum in the form of oxide clusters, ii) diffusion of Mo^{x+} ions into the bulk of the substrate, iii) agglomeration of small MoO_x clusters into larger particles, iv) growing of new TiO_2 layers via the oxidation of interstitial Ti atoms that are present in the layer and in the substrate. The first mechanism is almost surely in play. It is well-known that MoO_3 sublimates at high temperatures. Mo_3O_9 and Mo_4O_{12} clusters have been detected as the major constituents of the vapour phase above solid MoO_3 [123]. In UHV the onset of MoO_3 sublimation is ∼670 K [86] as already discussed in the previous chapter. The second mechanism is expected to be less prominent. This is discussed in the context of experiments performed with layers prepared according to procedures 3 and 4. The third mechanism is also expected to be less prominent than the first one. This is due to the fact that under oxidizing conditions, MoO_3 formation is thermodynamically favoured for agglomerates (Figure 3.8), and MoO_3 is volatile. Agglomeration may take place, yet these larger particles would sublime and contribute to the first mechanism. The dominance of trimeric clusters in the gas phase is an indication that aggregation is actually a necessity for sublimation. The fourth mechanism is the formation of new layers of TiO_2 during annealing in oxygen, which was already explained in the previous chapter. This process grows new layers of TiO_2 over the Mo-embedded TiO_2, consequently reducing the Mo3d XPS signal from the underlying layer. This mechanism requires the presence of already embedded molybdenum, which may be a part of the observed molybdenum. Nevertheless, there is no indication from XPS (comparison of the 70° and 0° spectra) that molybdenum concentrates in deeper layers. Therefore Mo^{6+} on the surface is probably not "overgrown" by the new TiO_2 layers and "swims" on the surface.

The Mo3d spectrum from Figure 4.6(c), taken in grazing configuration, is presented in more detail in Figure 4.7. The curve is fitted with two doublets, denoted as 1 and 2. "a" and "b" denote spin-orbit components with $m_j = 3/2$ and 5/2 respectively. In the fitting process, the ratio of the intensities of the spin–orbit components has been fixed. The major part the signal can be fitted with two peaks, 1a and 1b, but there remains significant intensity which has to be accounted for. Although two different Mo^{4+} species had been

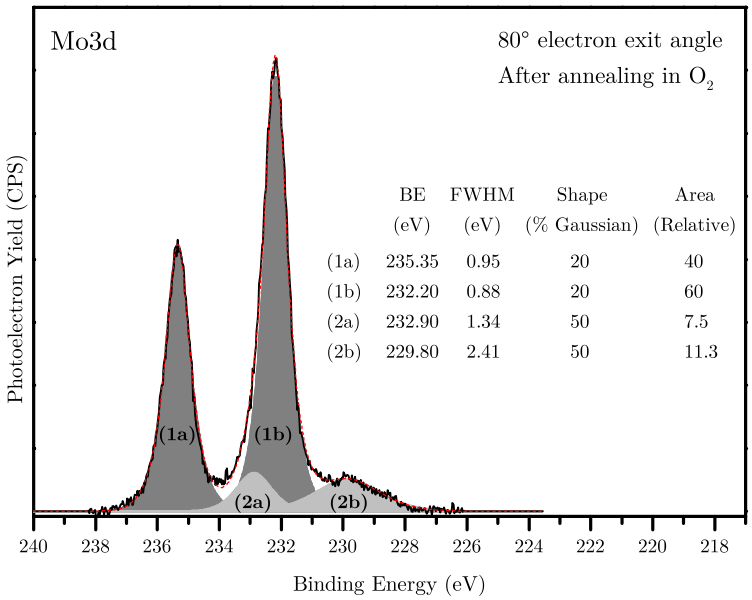

Figure 4.7: The result of peak fitting to the Mo3d spectrum (80° electron exit angle) from Figure 4.6(c). Peak shapes are modelled as Voigt profiles, approximated as a Gaussian/Lorentzian product form.

identified in the system, only one has been assumed and used in the fitting procedure since an additional, third doublet would be fitted with even greater uncertainty than the second one. In this sense, the Mo^{4+} component of the spectrum serves to complete the fit by accounting for all the Mo that is not Mo^{6+}, rather than finding a precise binding energy for Mo^{4+}.

The result of the peak fitting is that the Mo^{6+} and Mo^{4+} have Mo3d binding energies of 235.35/232.20 eV and 232.90/229.80 eV, respectively. The peak profiles, which are approximated as a Gaussian/Lorentzian product form (see appendix C) are 20% Gausssian for Mo^{6+} and 50% Gaussian for Mo^{4+}. The relative intensities of Mo^{6+} and Mo^{4+} come out to be 100:19. The uncommonly large breadth of peak 2b indicates that this component contains at least two components. It should also be noted that peak fitting applied to other spectra in Figure 4.6 yielded slightly smaller ($\sim$0.15 eV) Mo^{6+} binding energies. The slightly higher binding energies observed for the oxidized sample may be related to charging or band bending.

A high resolution STM image taken from a 33 Å thick mixed layer prepared at 870 K and containing 54% Mo (XPS, 70°) is shown in Figure 4.8. The full colour scale of the image is 10 Å, which corresponds to several atomic layers. In the upper-right part of the image, the solid and dashed lines divide the image into 4 types of regions. Each of these regions is at a certain height. Details are given in the caption. The co-existence of regions with different heights can be interpreted as resulting from the growth of oxide layers on top of each other without fully closing. An additional reason for the patchy morphology of

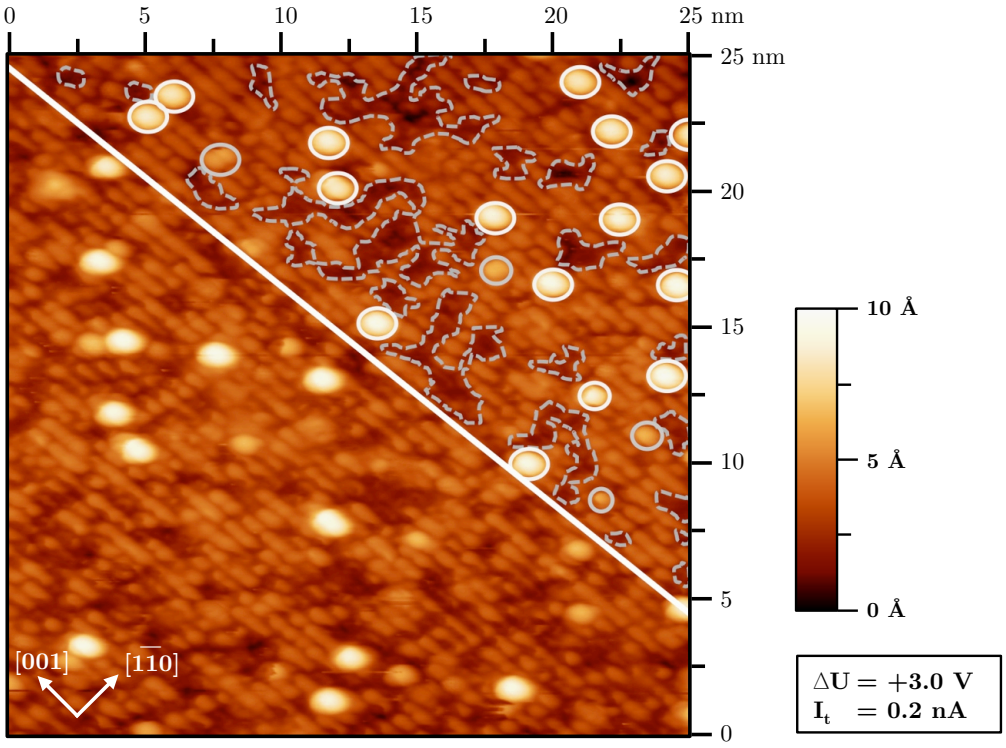

Figure 4.8: High resolution STM image of a surface prepared according to procedure 1 at 870 K and containing 54% Mo (XPS, 70°). The layer thickness is 33 Å (10 ML). In the upper right part of the image, regions of different heights have been marked. The few shallowest points, which are close to black in colour, mark the zero point in height scale. The regions enclosed by the dashed grey, solid grey and solid white lines are ∼2.5 Å, ∼7.5 Å and ∼10 Å high respectively. The rest of the surface which looks moderately bright is ∼5.0 Å high.

the surface shown in Figure 4.8 is possibly MoO_3 sublimation. The sublimation of MoO_3 may require the presence of MoO_x domains of a minimum size. During the growth of the layer, the competition between ordering and sublimation of MoO_x containing regions may result in such a final structure with irregular morphology.

The LEED pattern from the surface, whose STM image is shown in Figure 4.8, is qualitatively identical to a LEED pattern from a clean TiO_2(110) surface (see Figure 4.3). Although STM shows a corrugated layer without extended regions of order, if the original TiO_2 lattice is randomly occupied, small regions may create such a LEED pattern. This is similar to the case of surface alloys, where the LEED patterns of a pure surface and a surface with a lattice randomly occupied by two components are identical [124–129].

Larger scale STM images from the same surface are presented in Figure 4.9. In Figure 4.9(a), it can be seen that terraces have preferentially grown along the [001] direction. Another interesting feature visible in this scale is the presence of large, unusually shaped

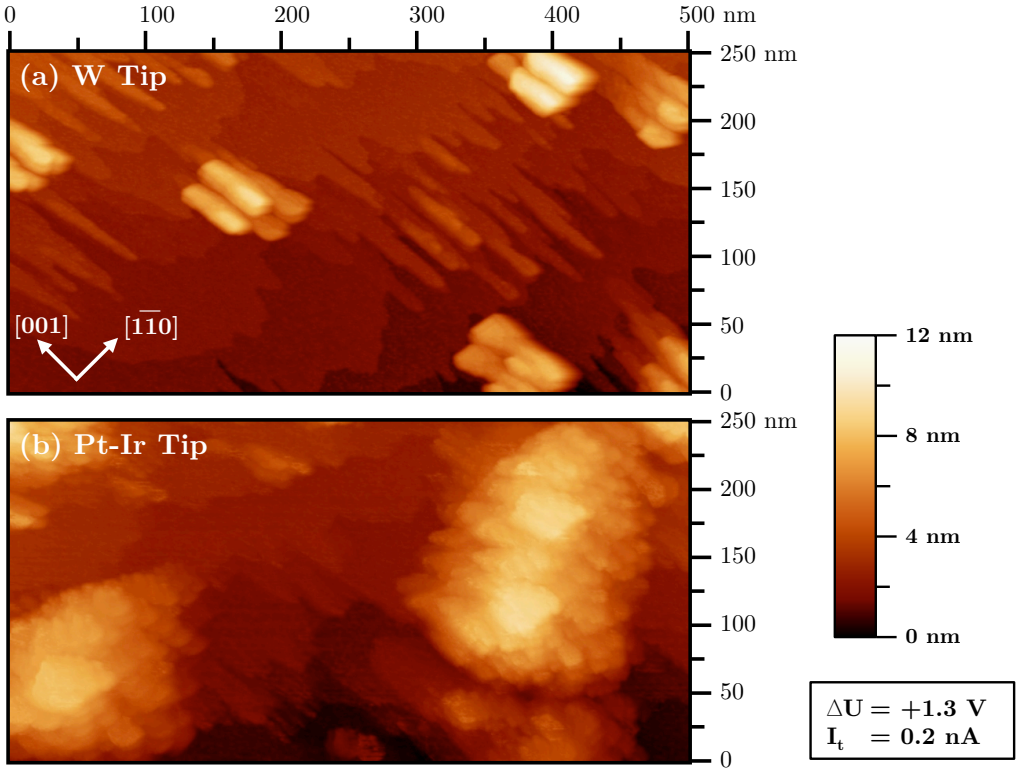

Figure 4.9: Large scale images of a surface prepared according to procedure 1 at 870 K and containing 54% Mo (XPS, 70°). The layer thickness is 33 Å (10 ML). Image (a) was taken using a W tip whereas image (b) was taken using a Pt–Ir tip, which is blunter. Scanned regions are different in the two cases.

particles. The shape of the particles change abruptly when the surface is imaged using a much blunter (Pt–Ir) tip, which means that the strange particle shape is a result of tip–particle convolution. The tip apex is larger than the particle itself, yielding an image of the tip instead of the particle.

Although the lateral size and shape of the particles seen in the STM images from Figure 4.9 are unreliable, the maximum height can be safely assessed. The height of the particles are in 7–9 nm range, which is quite significant considering the height variation on a terrace is ∼1 nm. Assuming such large structures grow with a low aspect ratio, and take the ratio as 1, we can roughly estimate how much material there is in these particles. Assuming a cube shaped MoO_2 particle with 8 nm long sides, one gets a 512 nm^3 particle. From large scale images, the number density of the particles is estimated as ∼30 μm^{-2}, which gives: $512 \times 30 = 15400$ $nm^3 \mu m^{-2}$. Assuming one monolayer of MoO_2 is about ∼0.3 nm thick, we hypothetically spread all the material in the particle onto the surface as a monolayer. That gives $15400/0.3 \approx 5 \times 10^4$ $nm^2 \mu m^{-2}$ which corresponds to 5% coverage. This means that if all the material in the particles were spread out onto the surface, it would cover

about 5% of the surface. This conclusion is valid only if the breadths of the particles are similar to their measured heights. The calculated amount of material within the particles increases by approximately a factor of ten if the measured breadths (W tip) are considered instead.

4.3 Procedure 2

This procedure, as explained earlier, aimed to get better mixing of the Mo into TiO_2 by depositing more TiO_2 after the molybdenum deposition is stopped. From Figure 4.2, it was already deduced that at low Mo concentrations, this was not the case and Mo stayed very near to the surface.

Figure 4.10 shows XPS spectra from a layer prepared according to procedure 2 and the spectra from the same layer after two annealing treatments in O_2. The layer was annealed at 850 K in $\sim 5 \times 10^{-6}$ mbar O_2 for 30 minutes each, and XPS spectra were taken after each treatment. The Mo3d spectra show that the amount of Mo decreases with each annealing treatment. The decrease is 37% and 53% relative to the initial Mo3d signal after the first and second treatments respectively. The amount of Mo^{4+} is reduced more significantly than the amount of Mo^{6+}, thus the latter becomes dominant as in the case of Figure 4.6. The decrease in the Mo3d intensity is very probably due to a loss of molybdenum via sublimation of MoO_3. The discussion made in the context of Figure 4.6 also applies here.

The Ti2p and O1s signals increase with each annealing step due to the removal of MoO_x near/above the surface. When quantified using grazing-configuration spectra, the rise in the Ti2p signal (between the first and last state) is 23% whereas for O1s it is 8% (the numbers become 14% and 9% when normal-configuration spectra are used). This clear difference can be attributed to at least two effects. First, the 5cTi atoms, which are normally exposed on a clean $TiO_2(110)$ surface, become covered with the introduction of MoO_x. Although part of the oxygen atoms also become covered due to MoO_x, the effect is compensated because the Mo containing structures are very probably also terminated with oxygen atoms. Secondly, the Mo atoms that may have substituted Ti atoms in the lattice are removed and replaced back by Ti atoms; an effect which is neutral in terms of the amount of oxygen in the system.

In a different experiment, a 37 Å layer was prepared at 850 K. A series of treatments was applied to the layer and XPS spectra were taken after each treatment. Figure 4.11 shows Mo3d XPS spectra from this series. On the right side of the spectra, a bar chart is shown, indicating the concentration of Mo calculated from XPS spectra obtained in grazing and normal configurations.

Initially, Mo^{4+} is more dominant than Mo^{6+}. With a 5 minute sputtering and consecutive 5 minute annealing (800 K in UHV), Mo^{4+} becomes even more dominant. The surface layer becomes more concentrated in molybdenum as compared to deeper layers according to the changes from (a) to (b) in the bar chart: the Mo concentration increases at grazing configuration while slightly decreasing in normal configuration. The effect may be related to i) the preferential sputtering of lighter Ti atoms as compared to heavier Mo atoms, ii) diffusion of reduced Ti atoms into the bulk during annealing, while reduced Mo atoms are

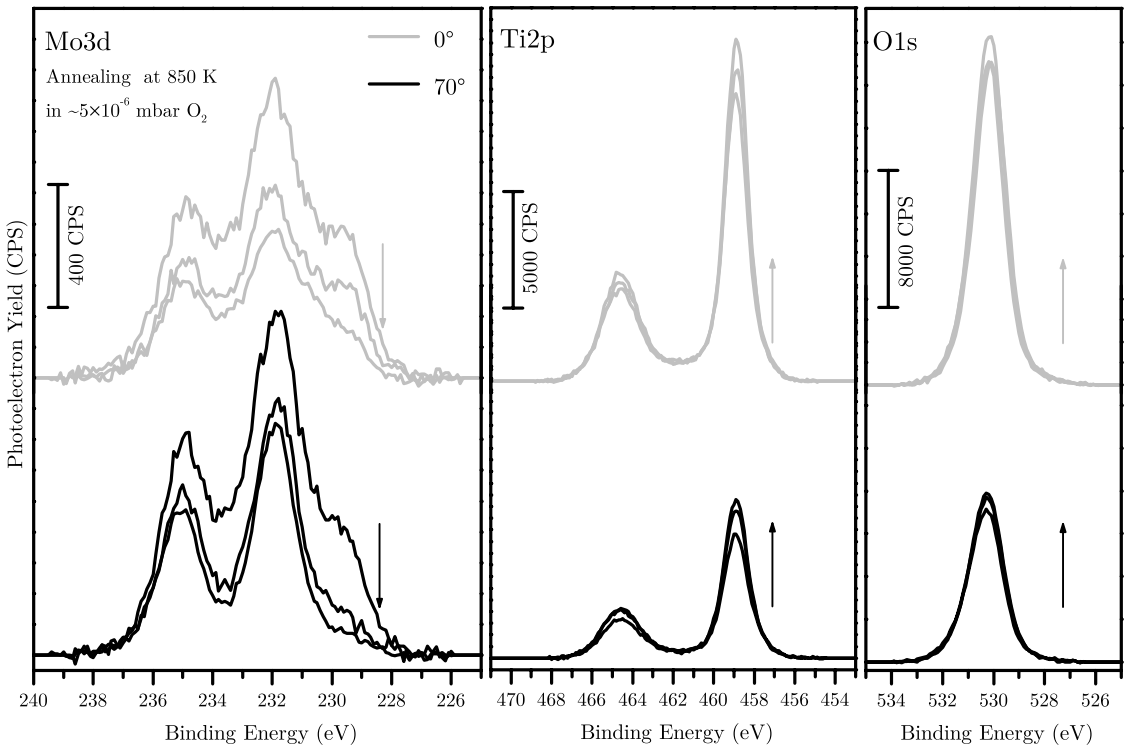

Figure 4.10: XPS spectra from a 36 Å thick layer prepared according to procedure 2 at 850 K. The spectra show the changes in Mo3d, Ti2p and O1s peaks after annealing the sample two times in O_2. Annealing has been performed at 850 K with the sample in front of the gas doser, with an estimated $\sim 5 \times 10^{-6}$ mbar O_2 pressure at the surface. The sample has been annealed two times, for 30 minutes each. Cooling was carried out in UHV. Spectra were taken after preparation and after each annealing. The arrows indicate the sequence of events. Shirley backgrounds have been subtracted from each spectrum.

reoxidized by lattice oxygen and stay on the surface.

From (b) to (c), the effect of mere sputtering is seen. The Mo^{6+} signal diminishes while the Mo^{4+} signal prevails. The Mo concentration is measured to be ∼1.5 times greater at grazing configuration than at normal configuration, which suggests that Mo is still mainly at and/or very near to the surface. Sputtering preferentially removes oxygen atoms first, so within 5 minutes of gentle sputtering, the surface MoO_x structures lose some oxygen and become reduced. The binding energies of the peaks in (c) are actually lower than all other ones in the figure, which implies that Mo may have a lower oxidation state than 4+.

Annealing the sample at 800 K after sputtering, (c) to (d), oxidizes some molybdenum back to Mo^{6+} and restores the position of the low binding energy peak. The bar chart shows that the Mo concentration increases during this annealing process, as well as the intensity of the Mo3d signal (not shown in the chart). It may be likely that during

annealing, some Mo atoms diffuse nearer to the surface; a process which may have a smaller activation barrier because of the defected nature of the sputtered surface. Further annealing, (e), at 800 K for 20 more minutes does not change much the Mo3d spectrum nor the Mo concentration.

When the sample is annealed at 870 K, the concentration of Mo increases although the intensity (or the shape) of the Mo3d signal does not change appreciably. This is probably due to the reduction of the TiO_2 at the surface, and diffusion of the reduced Ti^{n+} ions to the bulk, uncovering more Mo atoms from deeper layers. Uncovered Mo atoms are concentrated on the surface, but a quasi-equilibrium between different oxidation states continues, thus keeping the shape of the XPS spectrum constant.

Annealing the sample at 930 K for 10 minutes (g) leads to a decrease in Mo concentration, without significant change in the intensity or the shape of the Mo3d spectrum. At this temperature, oxidation of MoO_x to MoO_3 and subsequent evaporation is expected, based on the fact that lattice oxygen can also participate in oxidation. Domenichini et al. showed that, molybdenum deposited on a stoichiometric TiO_2 crystal, is oxidized to MoO_3 with subsequent evaporation when heated to ∼900 K in UHV [130]. Since oxygen of the TiO_2 lattice participates in the oxidation reaction, the initial extent of reduction of the TiO_2 crystal determines whether Mo would be oxidized or not. In the same work, it is indeed observed that the same experiment performed with a dark blue (reduced) TiO_2 crystal yields metallic molybdenum on the surface. Although the substrate which was used for our experiment was light blue (slightly reduced), and not yellowish (stoichiometric), oxidation to MoO_3 can still be expected because i) the substrate is not heavily, but only slightly reduced, ii) Mo is already oxidized to a certain extent, iii) the coverage of Mo is low enough that the required amount of oxygen can be supplied without causing extensive reduction to the substrate. Even though sublimation as MoO_3 explains the observed loss of Mo in step (g) of Figure 4.11, diffusion of Mo into the bulk of the substrate might have been considered as an alternative or complementary explanation. The results obtained from the experiments on Mo embedded TiO_2 layers (procedure 3) show that diffusion of Mo in TiO_2 is a very slow process at 900 K and below. Although in step (g) the annealing was carried out at 930 K, the Mo diffusion rates are not expected to be dramatically different. As a result, diffusion, in this case, can be a minor contribution to the loss of molybdenum from the surface.

The next annealing step (h) at 970 K, reduces the Mo concentration dramatically (by ∼50%), although the distribution of Mo oxidation states does not change significantly. There is no indication that the Mo concentration in the bulk increases. Further annealing at 970 K leads to a smaller loss of Mo than the previous treatment. Based on the above arguments, oxidation to MoO_3 and subsequent sublimation is again the primary mechanism of the Mo loss.

The mixed layer which forms after the last treatment (i) in Figure 4.11 is a relatively stable layer. Its Mo concentration and Mo3d spectrum are similar to those before the last annealing step at 970 K in UHV. This surface with 16% Mo content, produces a LEED pattern (not shown), which is identical to that of clean TiO_2(110). In order to understand whether this LEED pattern emerges from a surface terminated by pure TiO_2 or from a

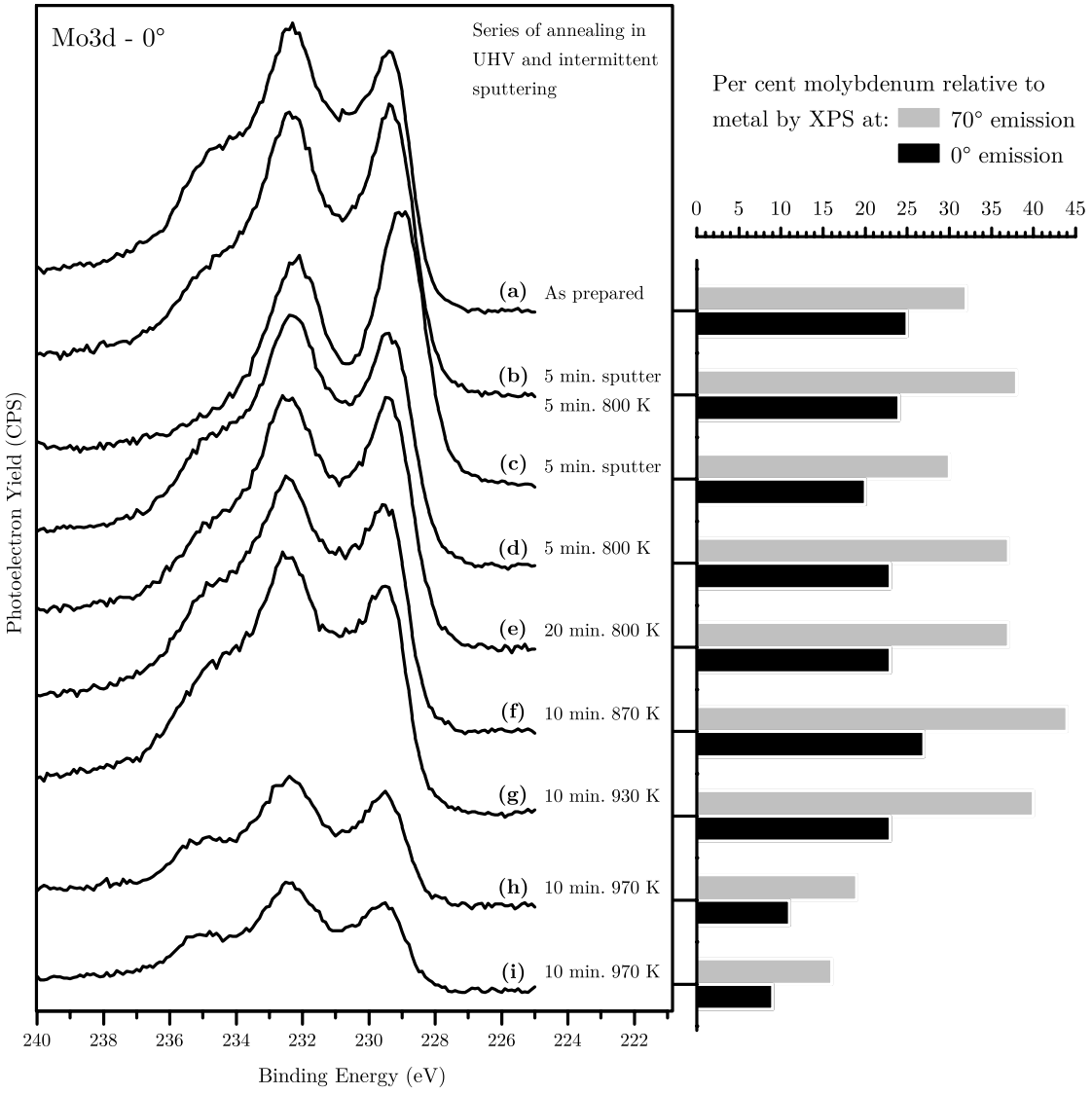

Figure 4.11: Series of XPS spectra which are taken after each consecutive treatment (annealing in UHV and/or sputtering with argon ions of 600 eV energy) applied to a 37 Å mixed layer prepared according to procedure 2 at 850 K. On the right is a bar graph, indicating the concentration of Mo in the film for each step in the spectra plot, as calculated from XPS measurements taken at 0°(black) or 70°(grey) electron exit angles.

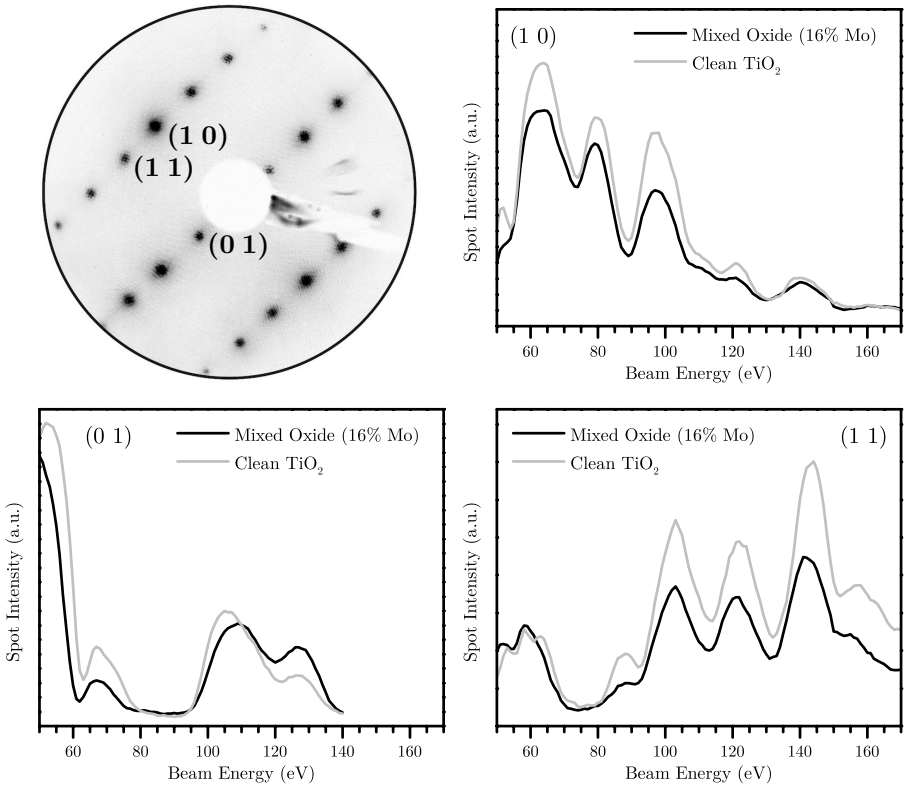

Figure 4.12: Beam energy dependence of LEED spot intensities for clean TiO_2(110) and a mixed oxide layer with 16% Mo, which corresponds to state (i) in Figure 4.11. The LEED pattern is from a clean TiO_2 surface and taken with 100 eV electron beam energy. Spot indices are given on the pattern and the graphs to indicate which graph belongs to which spot.

Mo containing surface with the same periodicity, IV curves of LEED spots have been recorded. Because our LEED system is not optimized for a proper angular adjustment of the sample as required for IV–LEED analysis, a comparison between the mixed oxide layer and a clean TiO_2 layer has been pursued instead. The beam energy dependence of spot intensities is plotted for three inequivalent spots in Figure 4.12. The curves from the two different surfaces match quite well for each spot. This indicates that it is indeed a TiO_2 terminated surface that produces the pattern. The molybdenum at the surface does not contribute significantly to the LEED pattern.

STM images from surfaces prepared according to procedure 2 are presented in Figure 4.13. All the layers have ∼5% Mo content. The images were acquired with relatively high bias voltages. Images (a), (b) and (c) show 20×10 nm^2 regions and image (d) shows a region which is 10 times a larger (200×100 nm^2). Similarities can be found between the features observed in (a), (b) and (c) in terms of size and symmetry. Among the

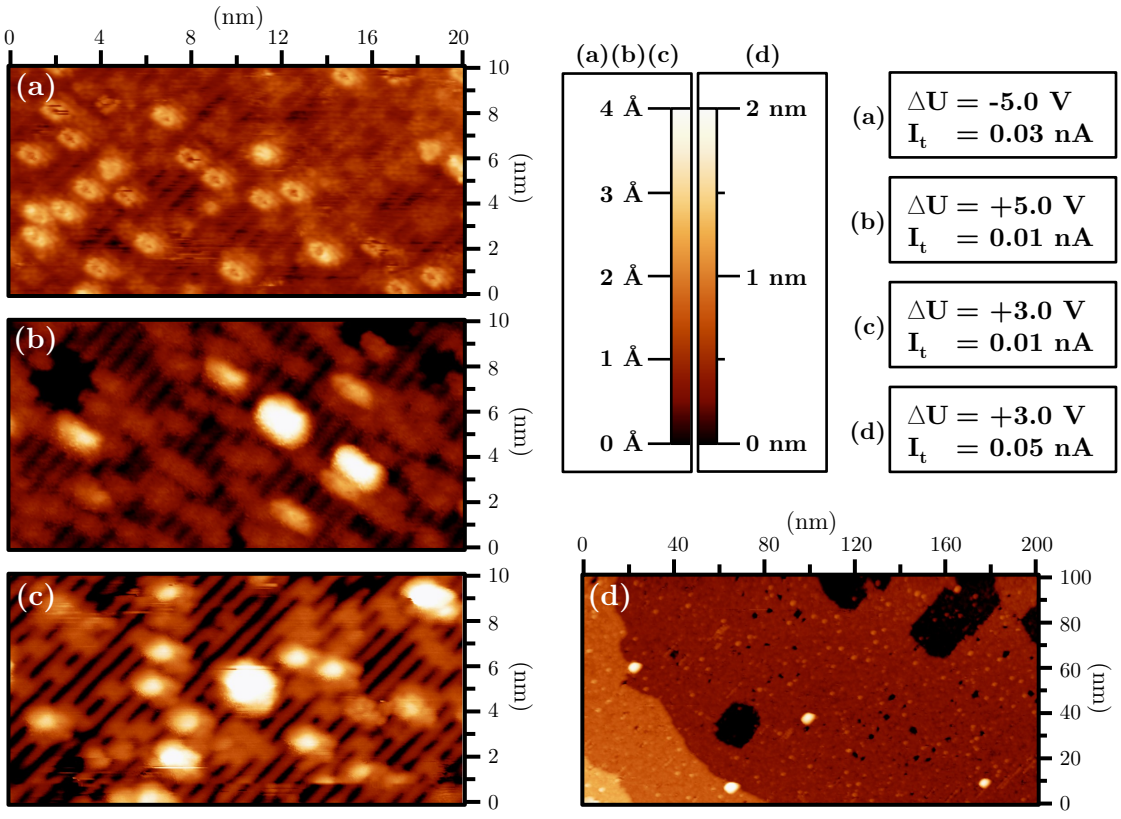

Figure 4.13: STM images of layers prepared according to procedure 2. (a) 35 Å thick layer prepared at 850 K and contains 5.0% Mo (XPS, 70°), (b, c, d) 17 Å thick layer prepared at 1000 K and subsequently annealed in UHV at 900 K for 10 minutes, which contains 4.7% Mo (XPS, 70°).

three images, (c) is the best resolved one, and resembles the images from layers prepared according to procedure 4. This similarity is not surprising, considering the conclusion reached in context of Figure 4.2: at low Mo concentrations, co-deposition produces layers similar to those prepared by depositing Mo onto TiO_2 in an oxygen ambient.

4.4 Procedure 3

It has been made clear by the results from procedure 1 and 2 that Mo has a tendency towards the surface at high temperature and in oxygen ambient. In order to prepare a layer which contains Mo mixed in the bulk of TiO_2, these two factors were eliminated from the preparation procedure. The two metals were deposited onto the substrate in UHV and the substrate was held at room temperature during deposition. Ti was deposited after Mo in order to keep Mo below the surface.

Figure 4.14 shows STM images and Mo3d XPS spectra from a layer prepared according to procedure 3 and from layers obtained by treating this layer at high temperatures.

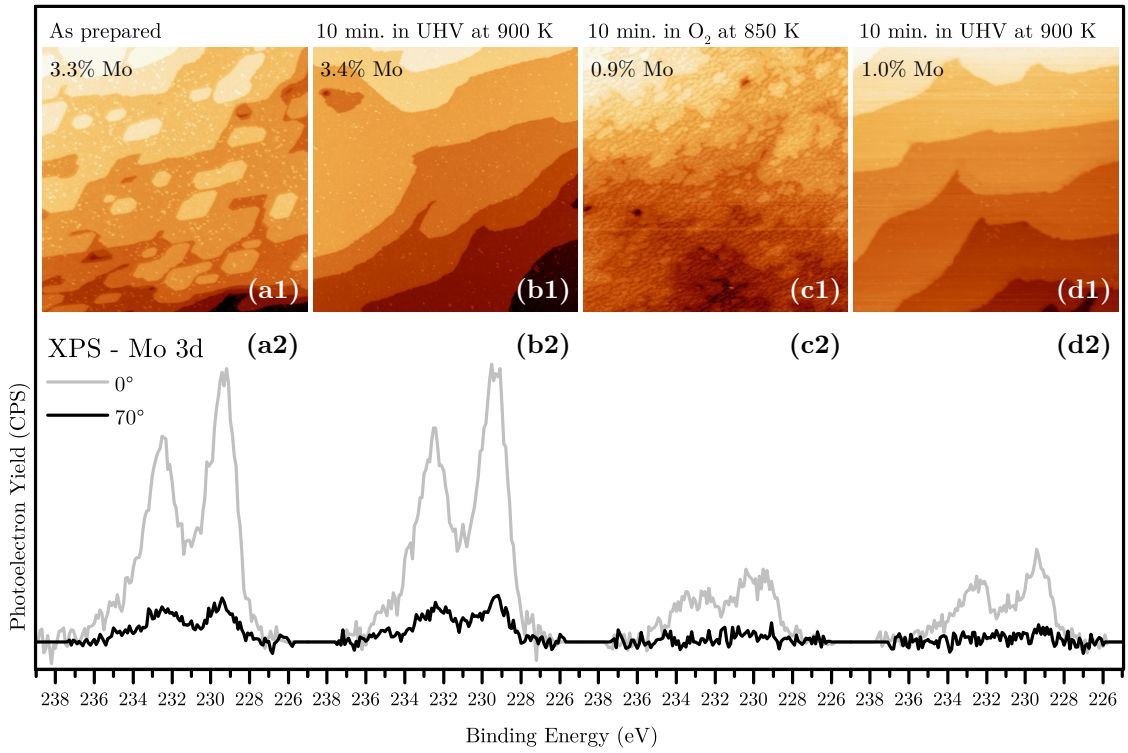

Figure 4.14: STM images and corresponding XPS spectra from a 6.5 Å thick mixed layer prepared according to procedure 3. The Mo concentrations given with the STM images were calculated from XPS spectra recorded for an electron exit angle of 0°. (a) after preparation of the layer, (b) after annealing in UHV at 900 K for 10 minutes, (c) after annealing at 850 K for 10 min in $\sim 5 \times 10^{-7}$ mbar O_2 (effective pressure in front of the doser) followed by cooling down in O_2, (d) after annealing again in UHV at 900 K for 10 minutes. The preparation steps were performed sequentially from (a) to (d). All STM images show an area of 200×200 nm^2 and were taken with $\Delta U = (+1.25)$–$(+1.5)$ V and $I_t = 0.1$–0.3 nA.

After the preparation, the surface still consists of small terraces and contains some small particles which are probably TiO_2 formed during the oxidation step. The Mo3d spectrum contains an asymmetric doublet with a binding energy corresponding to Mo^{4+} in MoO_2 [70, 116, 117]. The signal being far more intense at normal configuration than at grazing configuration implies that most of the Mo is below the surface.

Annealing this layer at 900 K in UHV renders a flatter surface, (b1). XPS spectra and Mo concentration do not change appreciably, which implies that molybdenum diffusion is negligible at this temperature. When this layer is annealed at 850 K in O_2 ambient (with cooling down in O_2), a decrease in the Mo3d signal is observed. Since diffusion of Mo can be excluded as an explanation to the phenomenon, another mechanism must be at play. It can be seen from (c1) that the surface becomes rougher after the treatment. This is due to the newly formed TiO_2 layers during oxidation. Because the cooling was carried out in O_2, partially formed TiO_x clusters remained on the surface, which is a well-known phenomenon [61, 63, 131]. The formation of new layers is the very reason for the observed decrease in the Mo3d signal. The Mo3d XPS signal is broadened, probably due to the oxidation of the surface and the concomitant electronic-structural changes. Annealing the layer one more time at 900 K in UHV produces a flat surface with large terraces. The intensity of the Mo3d signal remains the same and the broadening disappears.

The XPS data and large scale STM images imply that almost all the Mo is mixed in TiO_2. The presence of MoO_x above the TiO_2 surface can be excluded. There may still be some Mo (as Mo^{4+}) within the surface layer—possibly at a substitutional site—since such structures may not be visible in STM images acquired with low resolution. DFT calculations predict low stability for Mo substituted at the 5cTi site of TiO_2(110) [8, 115]. The same calculations find that the 6cTi site, which is below the bridging oxygens, is a relatively stable substitutional site for Mo. There is also experimental evidence from photoelectron diffraction measurements, in favour of the second structure [115]. STM images from the layers prepared according to procedure 4 exhibit a feature (named X2) which may also be due to substitutional Mo at the aforementioned 6cTi site. All these findings suggest that although Mo is mixed well in TiO_2 some Mo may still be present in the surface layer.

The results show that procedure 3 is promising for preparing Mo-doped TiO_2 layers, which can be used as model systems for studying the catalytic properties of doped oxides. However, further experiments with layers prepared according to this procedure have not been performed. The efforts were concentrated on trying to understand the structure and stability of different mixed Mo–Ti oxide layers. Nevertheless, the present findings should be useful for future studies which focus on the catalytic properties of Mo-doped TiO_2.

Among the early studies, the Mo3d XPS spectrum of MoO_2 had been shown to be highly asymmetric in the work of Werfel and Minni [132]. Detailed works on similar narrow-band metallic oxides have attributed the asymmetry to multiple final states [133–137] instead of other Mo species in a different chemical environment (i.e. multiple initial states). In a recent high resolution XPS study by Scanlon et al. [117], an unscreened final state line could be deconvoluted, and a quantitative assessment of the highly asymmetric MoO_2 lines could be made. Although it was not very clear in the cases of preparation 1 and 2,

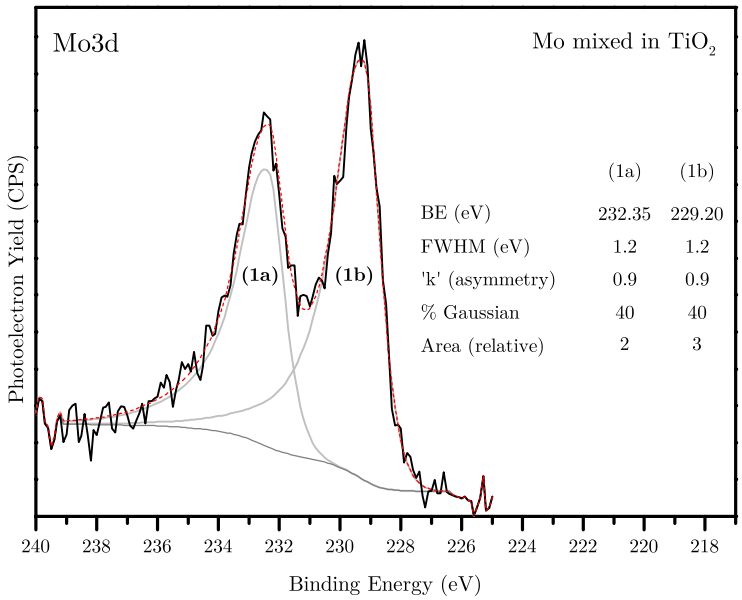

Figure 4.15: XPS spectrum (taken with 0°electron exit angle) of a 6.5 Å thick mixed layer prepared according to procedure 3. The layer contains 3.3% Mo (XPS, 0°). The spectrum is fitted with an asymmetric doublet on a Shirley background. Fitting parameters are given next to the plot. Details of the fitting function is given in appendix C.

in this preparation, by obtaining a distinct Mo^{4+} species, the asymmetry of the peaks can be treated quantitatively.

In Figure 4.15, the results of the peak fitting procedure to the spectrum (a2) of Figure 4.14 are shown. The peak profile used for fitting was picked because of practical reasons without relying on any theoretical argument. The practicality of the profile stems from the ease of its definition and its asymmetry being defined using only one parameter, hereby denoted as “k”. The main mathematical form of the profile is a Voigt function approximation, written as a Gaussian/Lorentzian product. The exact form of the function is given in appendix C. The obtained values are to be used in the further peak fitting processes, which involve mixtures of oxidation states.

4.5 Procedure 4

Procedure 4 has been employed to produce stable MoO_x species on the TiO_2 surface without any mixing of Mo into the TiO_2 bulk. Therefore only Mo, and no Ti, has been deposited. Deposition has been carried out in oxygen in order to ensure complete oxidation of molybdenum.

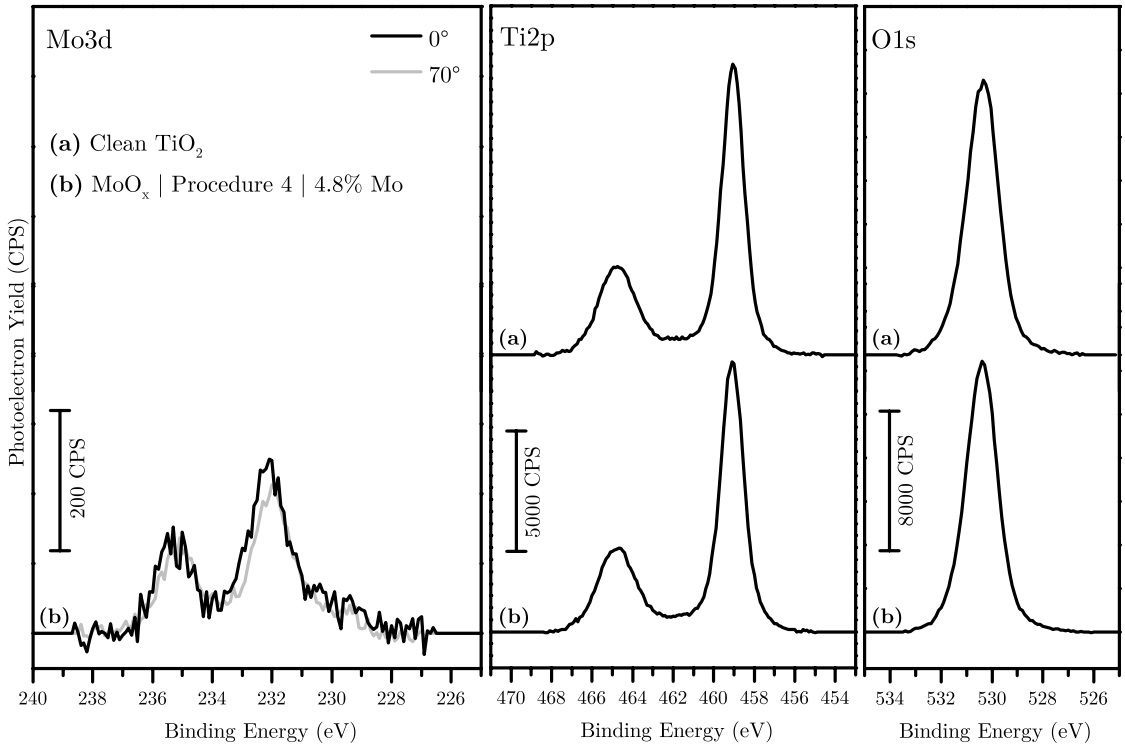

Figure 4.16: Mo3d, Ti2p and O1s XPS spectra from (a) a clean TiO_2 surface, (b) a surface prepared according to procedure 4 which contains 4.8% Mo (XPS, 70°). Shirley backgrounds were subtracted from the spectra.

Figure 4.16 shows XPS spectra from a surface, prepared according to procedure 4 and from a clean TiO_2 surface for reference. The Ti2p and O1s spectra are identical except for a small decrease in intensity. No shoulder to the lower binding energy side of the $Ti2p_{3/2}$ line can be seen, excluding any significant reduction of Ti^{4+}. The Mo3d spectra resemble the ones from Figure 4.7 and Figure 4.10 in the sense that the Mo^{6+} signal is dominant.

STM images of surfaces prepared according to procedure 4 with 1.3% of Mo are presented in Figure 4.17, which show almost mono-disperse particles (X1) on the well-known $TiO_2(110)$ surface. In addition to the particles, "bright square" structures (X2) were identified. Figure 4.18 shows these two features on an enlarged scale. X1 has a minimum along the $[1\bar{1}0]$ direction, which makes it look like a dimer. The minimum point is situated above the 5cTi rows and between two 5cTi atoms. The centre of the feature X2 also corresponds

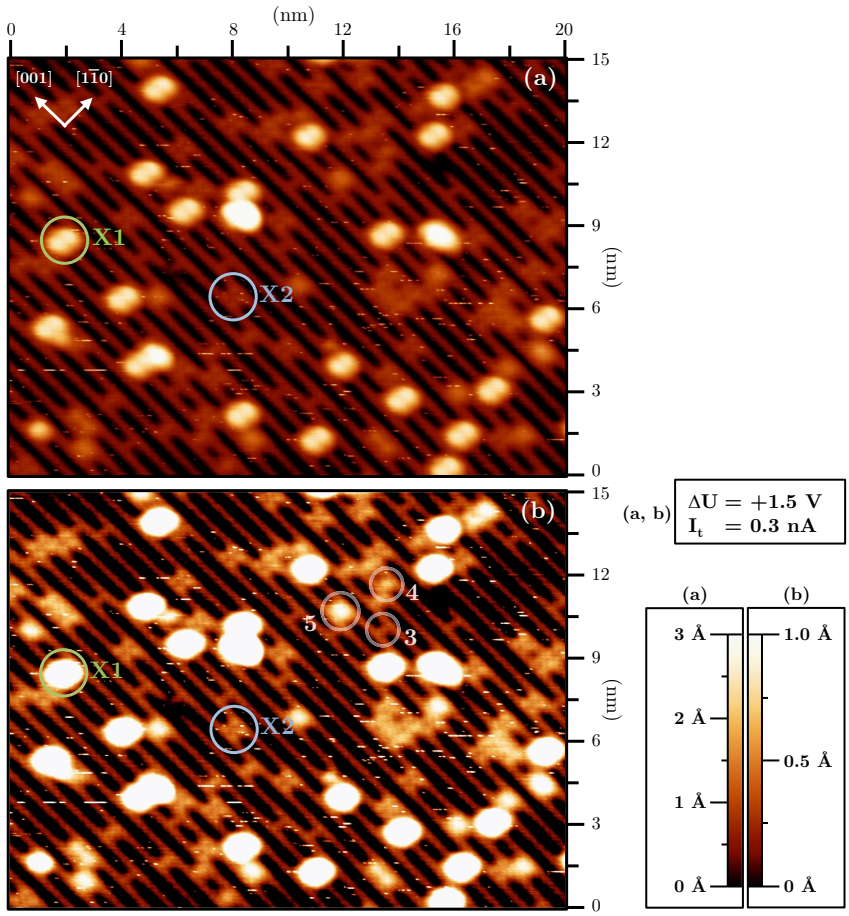

Figure 4.17: STM images from a surface prepared using procedure 4. The layer contains 1.3% Mo (XPS, 70°). Image (b) is identical to image (a) but with higher contrast, so that small protrusions are better visible. The two most common features are denoted as X1 and X2. Features 3, 4 and 5 are assigned to the well-known defects of TiO_2(110) surfaces: bridging oxygen vacancy, hydroxyl and double hydroxyl respectively.

to a local minimum. In the surface plane, the centre of X2 corresponds to the position of the titanium atoms which lie under the row of bridging oxygen atoms. The structures of these two features are not yet understood.

In the literature, a system studied by Chun and co-workers is close to the surfaces that have been prepared by procedure 4 in this work. The authors deposited molybdenum onto TiO_2(110) by "impregnation" of $(NH_4)_6Mo_7O_{24}$ and, using polarization-dependent total-reflection fluorescence x-ray absorption fine structure (PTRF-EXAFS), identified dimers of molybdenum oxide octahedra (edge-sharing) with the Mo–Mo axis being almost parallel to the [1$\bar{1}$0] direction [138]. The features denoted as X1 in our STM images may

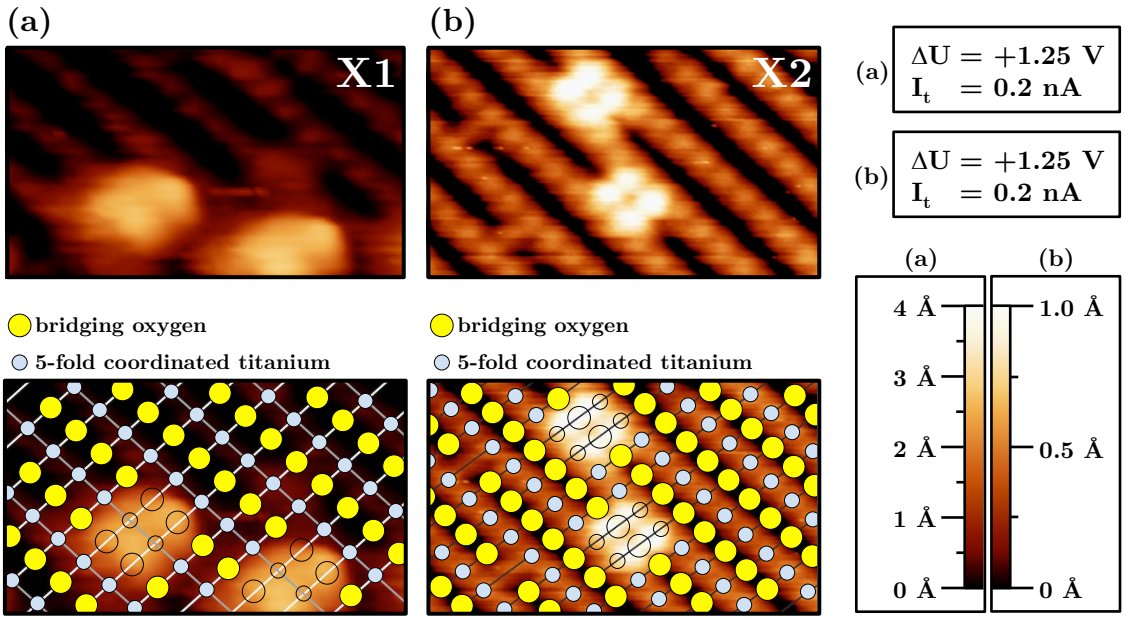

Figure 4.18: STM images of small regions containing the features (a) X1 and (b) X2, from layers prepared according to procedure 4. Below each image is a duplicate which has a $TiO_2(110)$ surface mesh superimposed onto it, showing 5-fold coordinated titanium and bridging oxygen atoms. Each bright spot on the 5cTi row is taken as the position of a titanium atom and bridging oxygen atoms are placed relative to the titanium atoms.

correspond to similar dimers. However, in our STM images the particles are centred at 5cTi rows (bright rows in STM) whereas the dimers proposed by Chun et al. are centred at bridging oxygen rows (dark rows in STM). The difference may stem from the different starting compound used in that study, which is a large complex containing 7 Mo atoms.

The thermal stability of the layer in UHV is demonstrated with XPS and STM in Figure 4.19 and Figure 4.20 respectively. XPS spectra from the as-prepared layer and the layers after 15 minutes of annealing at increasing temperatures in UHV are overlaid in Figure 4.19. The changes in the shape and the intensity of the spectrum are insignificant.

STM images from the surfaces mentioned in Figure 4.19 are shown in Figure 4.20. The contrasts of the images varies to some extent, due to different tip terminations and slightly different imaging conditions. Although the features X1 and X2 are not as well resolved in these images as in Figure 4.17, they can still be recognized. The density of X1 in all the images is around 0.04 per $TiO_2(110)$ unit cell, which implies that there is no agglomeration of the particles with annealing. X2 features could not be resolved very well in every case thus they were not counted. From the combined information from XPS and the stability of X1 from STM, it is reasonable to assume that the density of X2 also stays more or less unchanged.

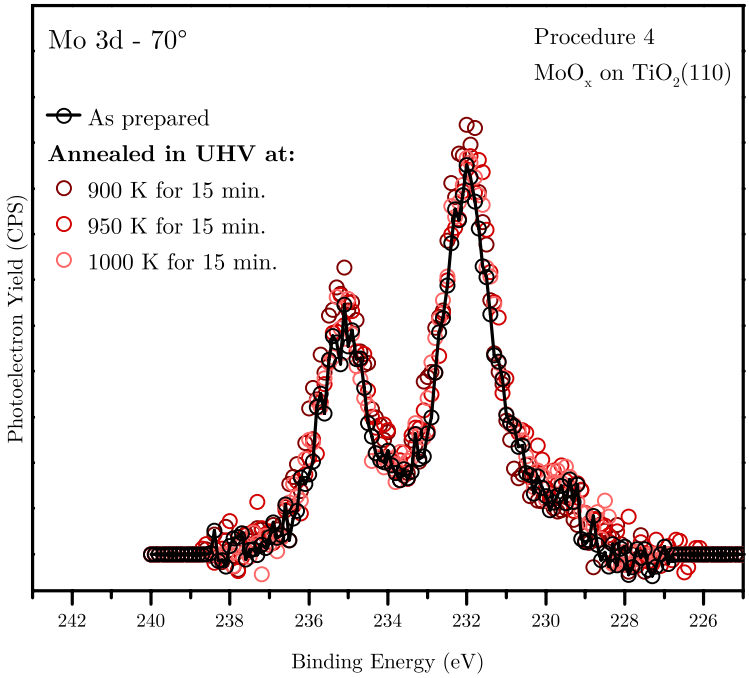

Figure 4.19: XPS spectra from a MoO_x layer prepared using procedure 4, demonstrating its thermal stability in UHV (4.8% Mo – XPS, 70°). Spectra were taken from the as prepared layer, and after annealing it in UHV for 15 minutes each, at 900, 950 and 1000 K.

In order to obtain a quantitative relationship between Mo concentrations obtained from XPS and the actual coverage of Mo on a surface, data from a series of preparations made using procedure 4 are plotted in Figure 4.21. The amount of Mo deposited is calibrated using a quartz microbalance right before the actual deposition. The deposition started only after the measured deposition rate reached a constant value. The x-axis is converted to a unit that was named as "MoO_2 monolayer (ML)", and reported in per cent. 1 MoO_2 monolayer corresponds to a single MoO_2 layer on TiO_2(110) and has a Mo density of 1.04×10^{15} Mo atoms/cm^2.

The data deviate from linearity at high coverage as expected. A linear regression using the data below 100% MoO_2 monolayer gives a slope of "0.34". This number can be used to convert the coverages reported in Mo percentage as calculated from XPS to a unit which may be more useful in many cases. It should be kept in mind that the linear relationship is only valid for low Mo concentrations, below ~30%.

Figure 4.22 shows the Mo3d XPS spectra from layers with increasing Mo coverage. Layers have been prepared according to procedure 4, but each layer used the preceding layer as the starting surface, instead of starting from a clean surface each time. Peak fitting was applied to the spectra. Two oxidation states were assumed, namely Mo^{6+} and Mo^{4+} for the fitting process. For Mo^{6+}, as was in Figure 4.7, a Voigt profile approximated by a

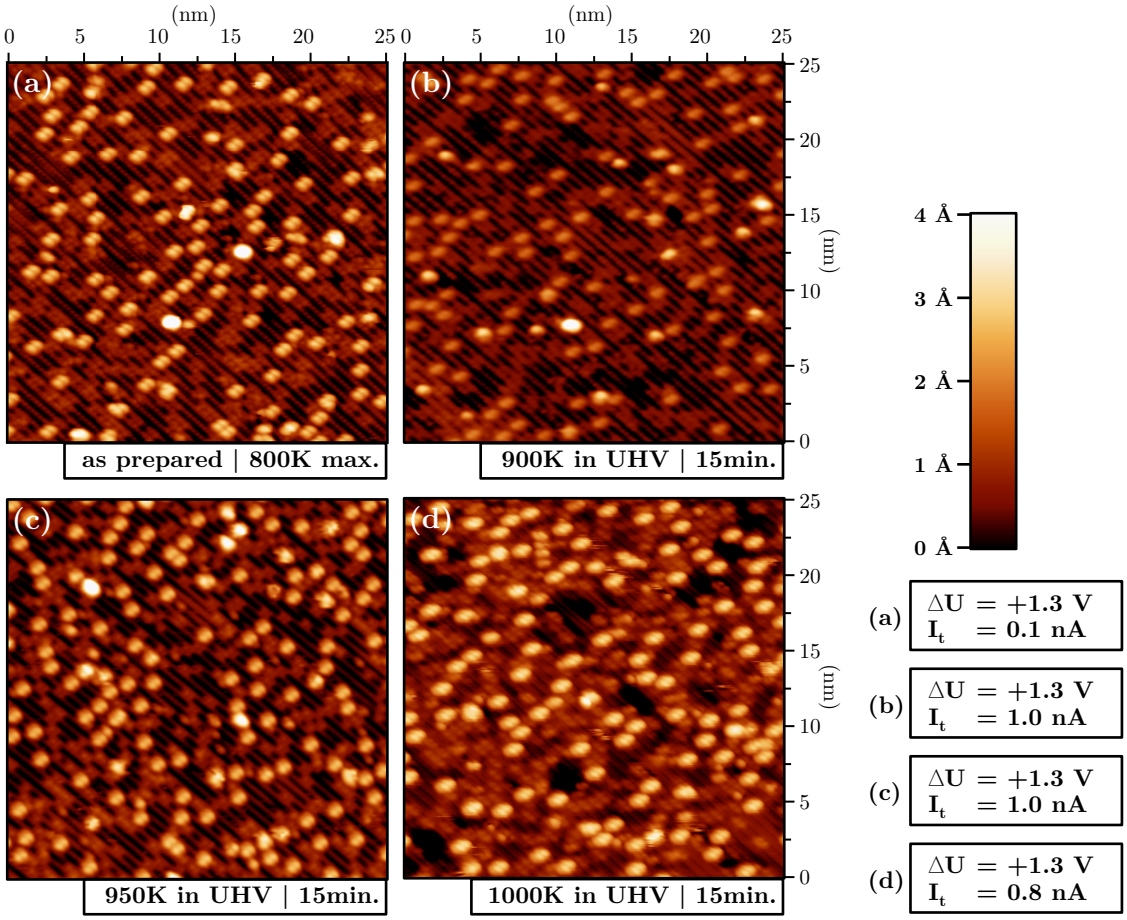

Figure 4.20: STM images from a MoO_x layer prepared using procedure 4, demonstrating its thermal stability in UHV (4.8% Mo – XPS, 70°). Images were acquired from the as prepared layer, and after annealing it in UHV for 15 minutes each, at 900, 950 and 1000 K. The density of the ∼3 Å high particles in all the images are ∼0.04 per TiO_2(110) surface unit cell.

Gaussian/Lorentzian product form was used (30% Gaussian). Mo^{4+} was fitted with the asymmetric function which was mentioned in the context of Figure 4.15, whose asymmetry parameter (0.9) and Gaussian percentage (40%) had been found by fitting it to the Mo3d spectrum of Mo^{4+} mixed in the TiO_2 bulk. The theoretical (2:3) intensity ratio, and the 3.14 eV splitting of the spin–orbit components were dictated to the fitting algorithm. Under these assumptions, good quality fitting was possible up to 0.80 ML MoO_2 coverage without using unrealistic peak widths or additional lines.

As the Mo coverage increases, the intensities of both components increase, which can be followed from Figure 4.22(c). Mo^{6+} is the dominant component at low coverages (< 0.5 MoO_2 ML) and Mo^{4+} is the dominant component at high coverages (> 0.5 MoO_2 ML).

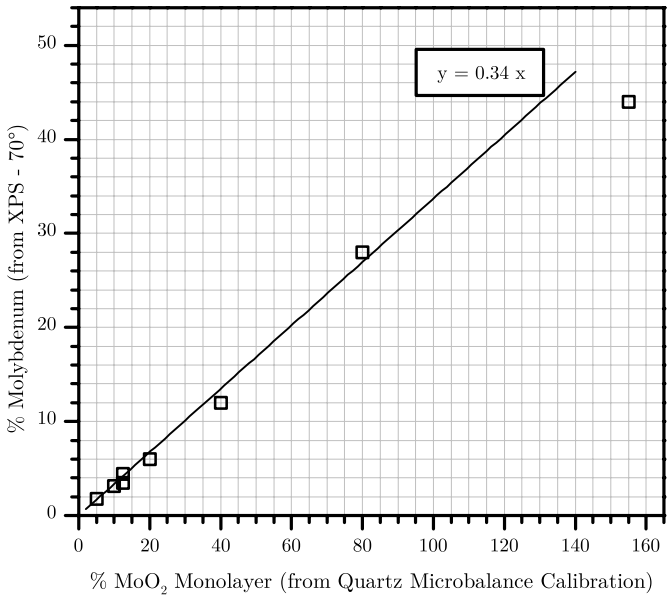

Figure 4.21: Correlation between the amount of deposited molybdenum (expressed in per cent MoO_2 monolayers and calibrated using the quartz microbalance) and the Mo concentration calculated from XPS data (taken with 70° electron exit angle), when the layer is prepared according to procedure 4.

The Mo^{6+} signal does not increase appreciably after 0.5 ML and looks like it is converging to a constant value. Above this coverage, the extra Mo added to the system becomes Mo^{4+}.

Figure 4.22(b) gives the binding energies and the widths of the fitted peaks. The $Mo3d_{3/2}$ binding energies of the Mo^{6+} species lie within the 235.05–235.25 eV range whereas the $Mo3d_{5/2}$ binding energies of the Mo^{4+} species lie within the 229.30–229.70 eV range. The general trend for both the Mo^{4+} and Mo^{6+} lines is that the peak widths increase as the coverage of Mo is increased. The increase in the peak widths may be due to the increased inhomogeneity, like the formation of a variety of different environments for Mo species with slightly different binding energies. The sum of these signals at slightly different binding energies would produce one broad peak rather than many narrow peaks if the peaks are broader than the binding energy range that is spanned.

The observed changes in the relative amounts of Mo^{6+} and Mo^{4+} with increasing Mo coverage are consistent with the following model: at low coverages Mo is well dispersed throughout the surface and forms identical structures almost exclusively (possibly X1 structures observed in STM images). These particles have the maximum possible oxygen coordination, giving the Mo atoms a 6+ oxidation state. As the coverage of these particles increase, they start to interact and oxygen bridges form between them. Oxygen sharing effectively reduces the average oxygen coordination, thus Mo^{4+} species begin forming. With increasing coverage, the overlayer possibly converges to a MoO_2-like structure. Neverthe-

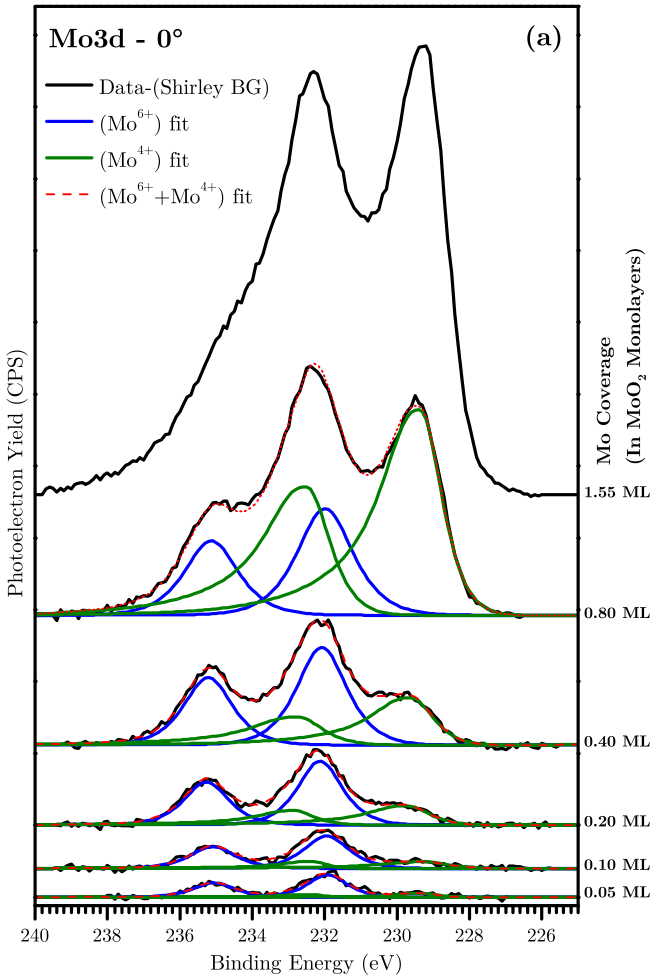

(b)

		Mo3d - Mo6+		Mo3d - Mo4+	
	J =	3/2	5/2	3/2	5/2
0.05 ML	BE (eV)	235.05	231.90	232.45	229.30
	FWHM (eV)	1.30	1.30	~1	~1
0.10 ML	BE (eV)	235.10	231.95	232.40	229.25
	FWHM (eV)	1.45	1.45	~1	~1
0.20 ML	BE (eV)	235.25	232.10	232.85	229.70
	FWHM (eV)	1.40	1.45	1.30	1.45
0.40 ML	BE (eV)	235.20	232.10	232.75	229.60
	FWHM (eV)	1.55	1.60	1.65	1.45
0.80 ML	BE (eV)	235.15	232.00	232.50	229.35
	FWHM (eV)	~1.7	~1.8	1.50	1.40

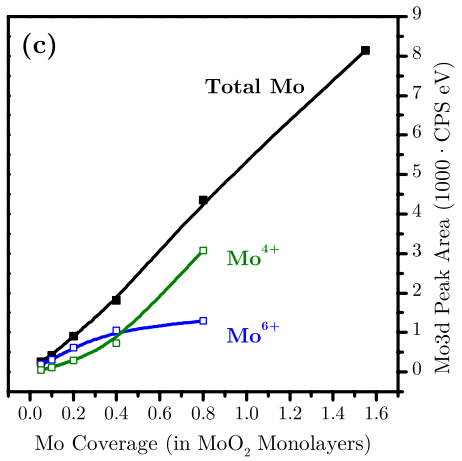

Figure 4.22: Mo3d XPS spectra (0°) with peaks fitted to them, from layers with increasing MoO_x coverage, prepared according to procedure 4. Each surface was prepared by depositing additional Mo onto the surface prepared in the previous step. The given coverages refer to the total amounts of Mo. A Shirley background was subtracted from each spectrum. (a) Two doublets were fitted to the spectra representing Mo^{6+} and Mo^{4+} except for the highest coverage, where fitting with only two doublets was found to not be appropriate. Mo^{6+} (blue) was fitted with a symmetric and Mo^{4+} (green) with an asymmetric profile. Details are given in the main text and in the appendix. (b) Fitting parameters (i.e. BE and FWHM) are tabulated as a function of Mo coverage. (c) The intensities derived from the spectra are shown as a function of coverage. The black line is the integrated Mo3d signal after background subtraction. The intensity of the fitted Mo^{6+} doublet is the blue line, and the intensity of the fitted Mo^{4+} doublet is the green line.

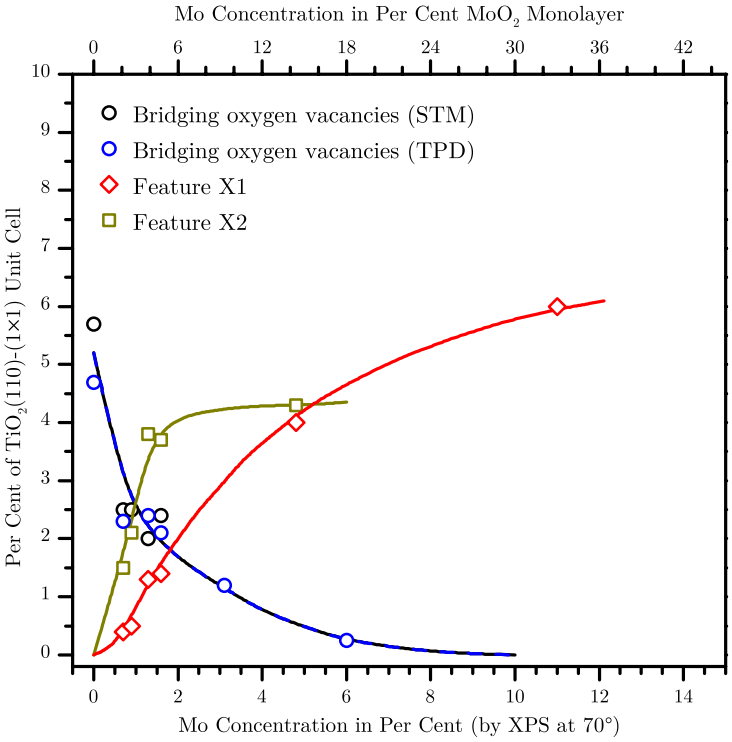

Figure 4.23: Concentration of different surface structures as a function of molybdenum concentration. The concentrations of the surface features were determined by counting the structures in the STM images and dividing this number by the number of $TiO_2(110)$–(1×1) unit cells that should be present in the measured area. In the case of bridging oxygen vacancies, in addition to STM, water TPD was also used for quantification by taking the ratio of the vacancy desorption peak to the monolayer desorption peak [139]. The molybdenum concentrations were calculated from XPS spectra (70°). The top x-axis gives the Mo concentration as MoO_2 coverage (per cent ML) according to the linear relationship obtained in Figure 4.21.

less, even at high Mo coverages, terminations of the layers have high oxygen coordination, giving them Mo^{6+} oxidation state. If only the terminal Mo atoms (or a certain fraction of the terminal Mo atoms) have the 6+ oxidation state in the layer, the signal of Mo^{6+} would converge to a constant as the Mo coverage increases, and the signal of Mo^{4+} would continue increasing just as observed in Figure 4.22(b).

Although STM images of all the studied mixed oxide layers were difficult to analyse at high Mo concentrations, at low Mo concentrations it was possible to count the different structures. The results are shown in Figure 4.23. The plot gives the number density of three features, X1, X2 and bridging oxygen vacancies, as a function Mo concentration. It is well known that residual water molecules present in UHV chambers dissociate at BOVs

forming 2 hydroxyls per vacancy. In the counting of vacancies, this fact has been taken into account, and hydroxyls were counted as half vacancies. As an additional source of information for the number of oxygen vacancies, water TPD has been performed, and the ratio of the ∼500 K peak to the monolayer peak has been taken [140].

The figure demonstrates that as the Mo concentration is increased, the number of X2 features rises more quickly in the beginning than the number of X1 features. At ∼2% Mo concentration, density of X2 starts to level out, and with ∼5%, it becomes roughly equal to the density of X1. At higher Mo concentrations, it becomes impossible to count X2, hence no data is presented for X2 above 5% Mo. Although the increased coverage makes counting X1 less reliable, it is still possible, and its density continues to rise after 5% Mo as well. Although the coverage dependence of the densities of X1 and X2 resemble that of Mo^{4+} and Mo^{6+} obtained from XPS peak fitting, it should be noted that the density of X2 levels out at much lower coverage (∼0.1 MoO_2 ML) than Mo^{6+} does (∼0.5 ML or above).

Another important fact which is demonstrated by Figure 4.23 is that as the coverage of Mo increases, the density of BOVs decreases. STM images have been used to track the density of this type of defect up to ∼2% Mo concentration. Above this point, STM was no longer reliable and the densities were obtained from the TPD spectra. At 6% Mo concentration, the recombinative water desorption peak (at ∼500 K) vanishes almost completely. Above this concentration, it is hard to speak of a distinct water desorption peak at ∼500 K. As a result, it has been concluded that above 6% Mo concentration BOVs don't exist. On the other hand, this does not mean that there are no sites that dissociate water. Such sites with various structures probably exist at higher Mo concentrations, as evidenced by the broad, high-temperature water desorption features in the TPD spectra. These results are presented in the next chapter.

4.6 Procedure 5

Procedure 5 is the repetition of a layer preparation procedure as reported by Domenichini et al. [115]. Mo is deposited onto TiO_2 in UHV at room temperature and the sample is annealed at 670 K after the deposition. No gaseous oxygen is used during the preparation. In that work, the position of the molybdenum atom after annealing is predicted to be the substitutional site under the bridging oxygen atoms. This site is preferred up to a Mo coverage of $\sim 2\times10^{14}$ atoms/cm^2 (0.2 MoO_2 ML). In this structure, the Mo atom is in a MoO_2-like environment and the Mo3d binding energy is consistent with the binding energy of Mo in MoO_2. The barrier for diffusion of a Mo atom from its most stable adsorption site to subsurface is low enough that a substantial fraction of molybdenum atoms can go to subsurface at room temperature [140].

Figure 4.24 shows the evolution of Mo3d, Ti2p and O1s XPS spectra during the stages of layer preparation and with annealing treatments at increasing temperatures in UHV. Stage (a) shows the intermediate step in the preparation procedure, where Mo is deposited but the sample is not yet annealed to 670 K in UHV. At this point, the deposit produces an asymmetric Mo3d doublet with probably a single component. The $Mo3d_{5/2}$ binding energy

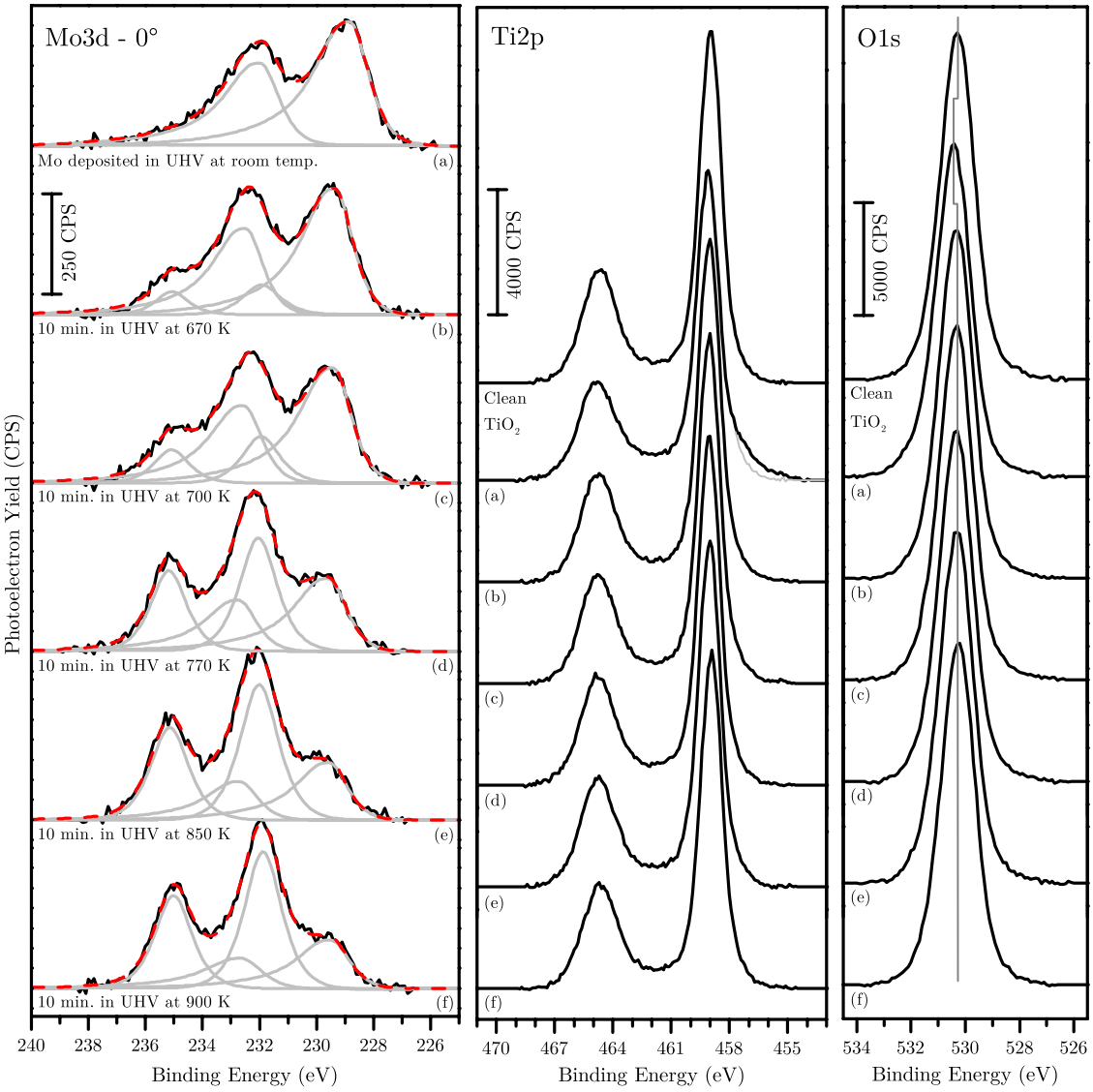

Figure 4.24: XPS spectra taken in between a series of annealing steps (in UHV), applied to a layer prepared according to procedure 5. The layer contains 11% Mo (XPS, 70°). State (a) actually represents the situation before the completion of procedure 5, namely before the annealing step at 670 K. Peak fitting was done for the Mo3d spectra. Two doublets were fitted to the spectra representing Mo^{6+} and Mo^{4+}. Mo^{6+} was fitted with a symmetric and Mo^{4+} with an asymmetric profile. Details are given in the main text and in the appendix. Ti2p and O1s spectra are presented together with spectra from a clean TiO_2(110) surface for comparison. The grey curve in the Ti2p plot (a) shows the data from the clean TiO_2 spectrum, in order to demonstrate the reduction of titanium. The grey line in the O1s plot marks the peak maximum position. A Shirley background was subtracted from each spectrum.

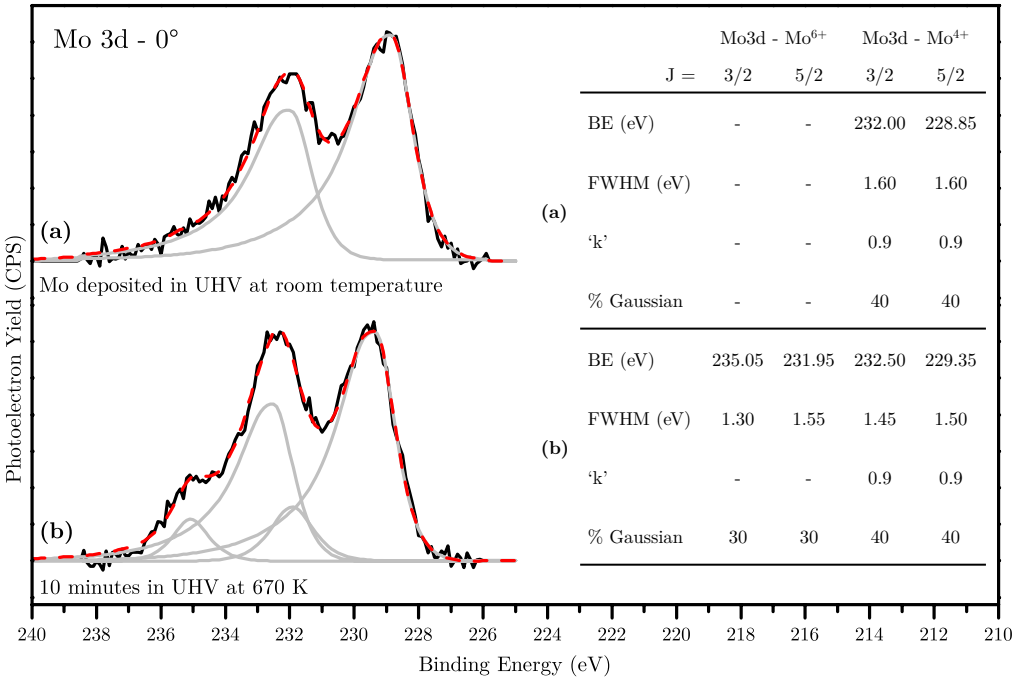

		Mo3d - Mo^{6+}		Mo3d - Mo^{4+}	
	J =	3/2	5/2	3/2	5/2
(a)	BE (eV)	-	-	232.00	228.85
	FWHM (eV)	-	-	1.60	1.60
	'k'	-	-	0.9	0.9
	% Gaussian	-	-	40	40
(b)	BE (eV)	235.05	231.95	232.50	229.35
	FWHM (eV)	1.30	1.55	1.45	1.50
	'k'	-	-	0.9	0.9
	% Gaussian	30	30	40	40

Figure 4.25: Peak fitting parameters for the Mo3d spectra (0°) from Figure 4.24(a) and (b). (a) was fitted with one (Mo^{4+}) and (b) with two doublets (Mo^{4+} and Mo^{6+}). Mo^{6+} was fitted with a symmetric and Mo^{4+} with an asymmetric profile. Details are given in the main text and in appendix C.

(228.85 eV) is ∼0.35 eV lower than that of Mo^{4+} which was produced by embedding Mo in TiO_2 (i.e. procedure 3). The $Ti2p_{3/2}$ peak forms a clearly visible low binding energy shoulder, indicating the reduction of Ti^{4+}. This has been expected given the partial oxidation of molybdenum atoms without any ambient oxygen gas. The O1s peak shifts slightly (∼0.1 eV) towards higher binding energies. Annealing at 670 K in UHV for 10 minutes completes the preparation, (b). At this point, the position of the lowest binding energy peak becomes consistent with Mo^{4+} and a high binding energy shoulder arises (i.e. Mo^{6+}), which is consistent with the previous observation of a redox reaction between the deposit and the substrate (see Figure 4.11). The shoulder of the $Ti2p_{3/2}$ line disappears, and O1s peak shifts back to its original position. The intensity of the Mo3d signal increases by 10%, taking the Ti2p signal as an internal reference. Further annealing the sample in UHV at increasing temperatures increases the intensity of the Mo^{6+} component in expense of the Mo^{4+} component. No appreciable change is observed in the Ti2p and O1s spectra. The intensity of the Mo3d signal remains constant within the margin of error. At 850 K, the equilibrium between Mo^{6+} and Mo^{4+} signals is reached. Annealing at 900 K makes very little difference.

Peak fitting parameters obtained from the first two Mo3d spectra in Figure 4.24 is pre-

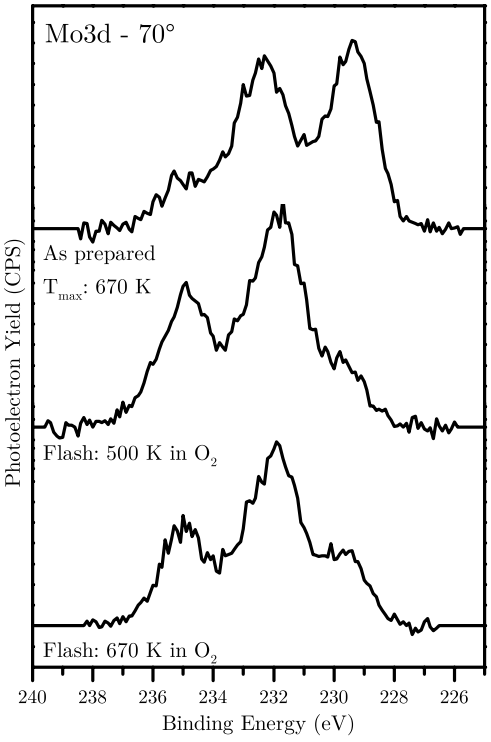

Figure 4.26: XPS spectra (70°) taken in between a series of "flash" heating steps (in O_2), applied to a layer prepared according to procedure 5. The layer contains 7.4% Mo (XPS, 70°). Heating (2–3 K/s) was carried out in front of the gas doser which was producing an effective pressure of $\sim 1 \times 10^{-6}$ mbar on the surface. Cooling down was carried out without oxygen. A Shirley background was subtracted from each spectrum.

sented in Figure 4.25 for quantitative consideration. Annealing the as-deposited molybdenum at 670 K in UHV shifts the $Mo3d_{5/2}$ peak from 228.85 eV to 229.35 eV which is in the range of binding energies reported for MoO_2 (229.3–229.5 eV) [116, 117]. These binding energies (i.e. before and after annealing) are in good agreement with the ones reported in the work of Domenichini et al. [115].

Another experiment has been carried out for the oxidation of Mo^{4+} with gaseous oxygen, instead of lattice oxygen. Figure 4.26 shows the Mo3d spectrum from the as prepared layer as well as those taken after a quick heat-and-cool treatment to 500 K and 670 K in O_2. Already at 500 K, Mo is oxidized to the extent it had been oxidized in Figure 4.24(e), (i.e. by annealing in UHV at 850 K). Further heating to 670 K makes no difference.

STM images from a surface prepared according to procedure 5 are presented in Figure 4.27. Images (a) and (b) are identical, only with different colour contrasts for a better visualization of species with significantly different apparent heights. Features similar to the ones observed on surfaces prepared according to procedure 4 (i.e. X1 and X2) can be

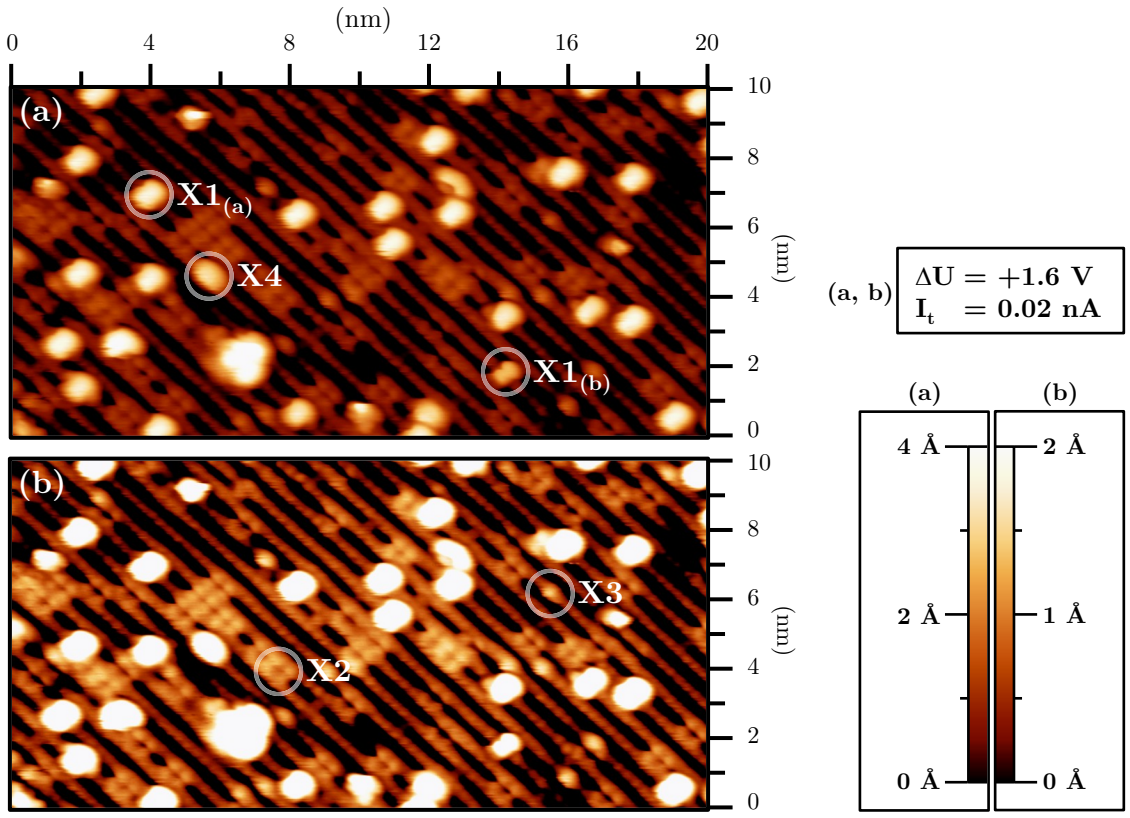

Figure 4.27: STM images from a surface prepared using procedure 5, containing 7.4% Mo. Image (b) is identical to image (a) but with higher contrast, so that small protrusions are better visible. Common features are denoted as $X1_{(a)}$, $X1_{(b)}$, X2, X3 and X4. $X1_{(a)}$ and $X1_{(b)}$ have identical shapes, the former being 0.8–0.9 Å higher than the latter.

identified in the images. Two features, $X1_{(a)}$ and $X1_{(b)}$, both resemble X1 from preparation 4 in size and symmetry. $X1_{(a)}$ is 0.8–0.9 Å higher than $X1_{(b)}$. The features that look like bright squares are named X2, as they look almost identical to those present in Figure 4.17.

Among the features present in the STM images in Figure 4.27, the one feature which fits the "subsurface-Mo" prediction of Domenichini et al. [115] is the bright square (X2). The centre of this feature, as already mentioned in the context of procedure 4 (Figure 4.18), corresponds to the position of the titanium atom that is under the bridging oxygen row. Furthermore, the feature possesses the symmetry that is expected from a point defect at the TiO_2(110) surface (i.e. unchanged under the operations: σ_x, σ_y, C_2).

In addition to the similar features, there are also features in the STM images which are specific to procedure 5. These are labelled as X3 and X4. Both features are centred at bridging oxygen rows. X3 is a small bright spot, about the size of a single atom. X4 is also a bright spot but it is wider along [001] direction.

4.7 Procedure 6

Preparation of a thick MoO_3 layer that would serve as a reference has been aimed by procedure 6. The procedure required the oxidation of a partially oxidized layer to bulk MoO_3, which required the use of the high pressure cell. XPS spectra from a 50 Å thick layer are shown in Figure 4.28. The Mo3d spectrum is dominated by a Mo^{6+} signal. The Ti2p intensity is almost non-existent, whereas the O1s signal peaks around 530.35 eV.

As shown in Figure 4.29, peak fitting to the Mo3d spectrum gives two species with $Mo3d_{3/2}$ binding energies at 235.45 and 233.80 eV. The line at 235.45 eV is the dominant species, and can be safely ascribed to Mo^{6+}. The second one is a minor contribution with 3.5% of the total intensity. The intensity of this feature is so small that it could in principle be an artefact of the peak fitting procedure. Choosing an improper background or peak shape might lead to such an outcome. After trying many background and peak types/parameters, it has been concluded that the signal is real. In the literature, peaks about 1.6 eV negative shifted from Mo^{6+} has been assigned to Mo^{5+} at shear planes [83] as well as ionic Mo^{4+} [116] (which is different from Mo^{4+} in metallic MoO_2). A similar species identified in a MoO_3 single crystal has been ascribed to slight surface reduction by Scanlon et al. [117], without any assignment of structure or oxidation state. In our

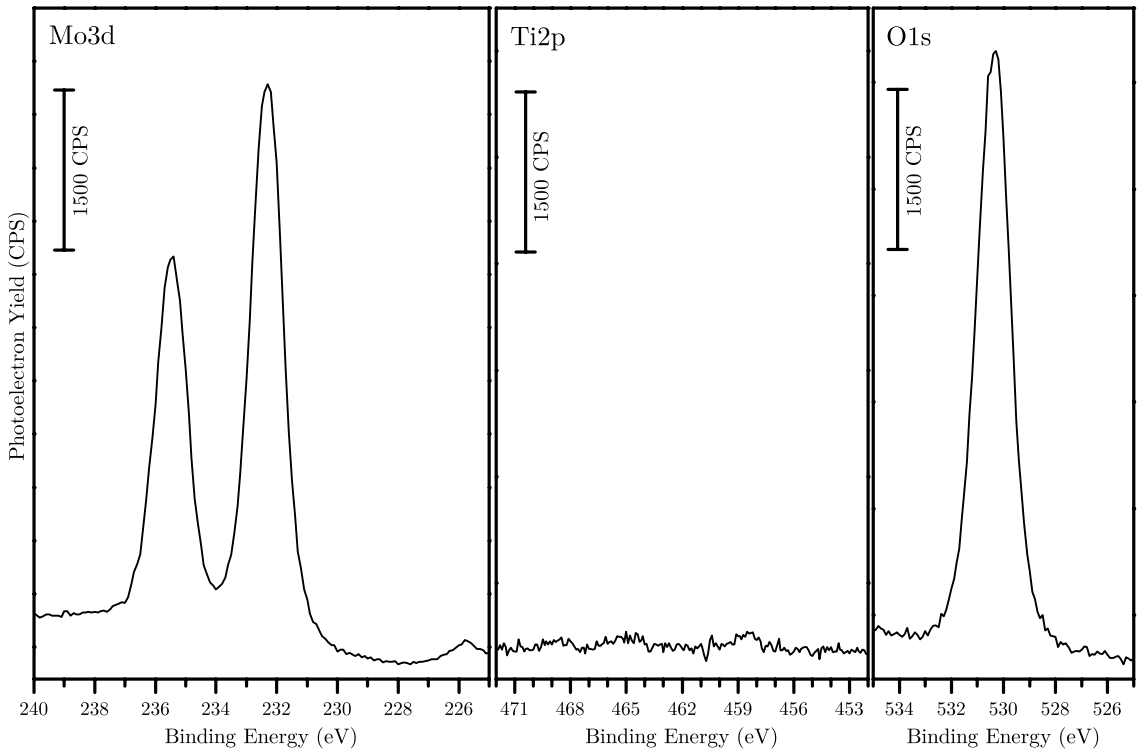

Figure 4.28: XPS spectra (70°) from a 50 Å thick MoO_3 layer prepared according to procedure 6.

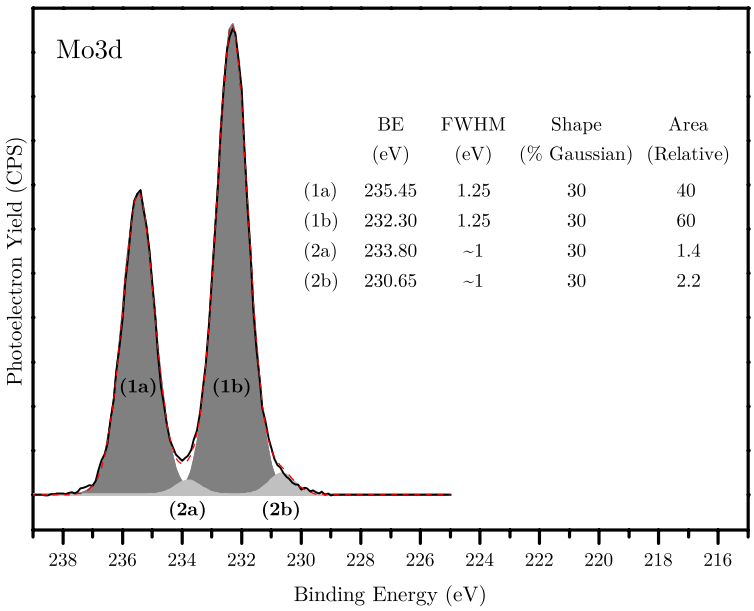

Figure 4.29: Peak fitting to a Mo3d XPS spectrum (70°) acquired from a 50 Å thick MoO_3 layer prepared according to procedure 6.

case, peak fitting to spectra taken at grazing and normal configurations have both given around the same percentage of this reduced species, making it less likely a surface effect. Crystallographic shear planes may be the source of this reduction, which is expected for the MoO_3 system.

A large scale STM image of the same layer is shown in Figure 4.30, with typical 2D orthographic (a) and 3D perspective (b) views. The morphology of the surface is rough, as compared to other layers studied in our work so the 3D reconstruction provides a better intuition for the structure. The full height scale of the image is 20 nm, which is 4 times the thickness of the film itself. This shows that island formation took place at some point in the procedure. The crystallites have a particular orientation, which demonstrates the effect of the substrate on growth. There are flat regions throughout the film, however these regions could not be imaged with high resolution with the STM. No LEED pattern could be obtained from the layer either which is an indication that the flat regions are not ordered.

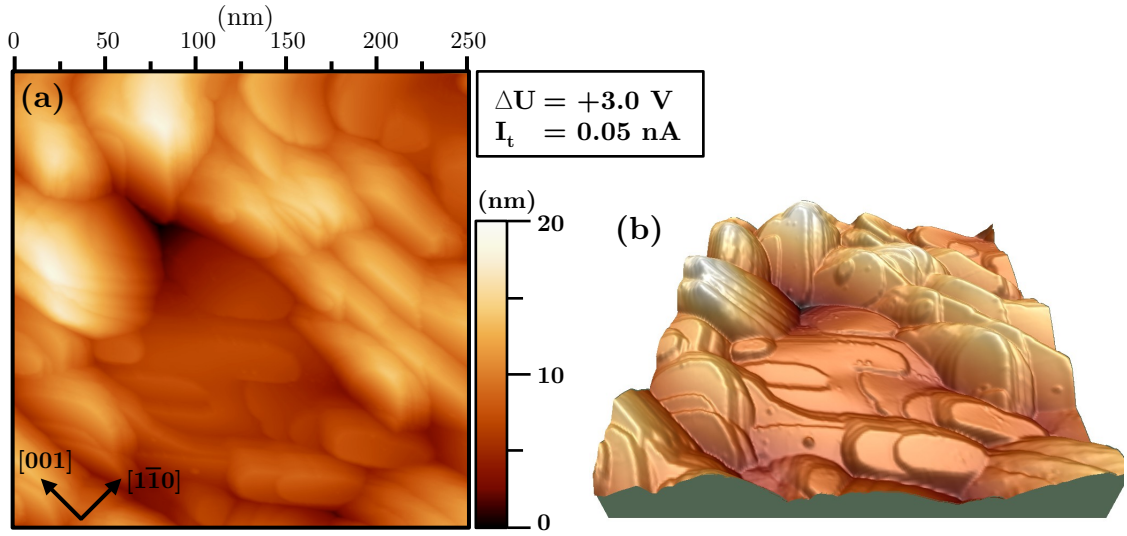

Figure 4.30: STM image of a 50 Å thick MoO_3 layer prepared according to procedure 6: (a) typical 2D image in which height is colour coded, (b) 3D reconstruction of the same image.

5 INTERACTION OF MIXED LAYERS WITH WATER, METHANOL AND ETHANOL

The interaction of water, methanol and ethanol with the layers presented in the previous chapter has been investigated, mostly using temperature programmed desorption (TPD). Results of these investigations will be presented in this chapter, along with some results obtained using XPS and STM.

Breaking of the H_2C–H bond of alcohols in the gas phase requires less energy by about 20–35 kJ/mol as compared to the O–H bond [141–144]. However, the interaction with an oxide surface reverses this tendency. On TiO_2(110), alcohol chemistry is initiated with the breaking of the O–H bond and the formation of an alkoxy–hydroxyl pair. Water can also be visualised as an alcohol (i.e. R–OH) where the R group is a H atom. From this perspective, there is no surprise that interactions of alcohols and water with surfaces show many similarities, which will be pointed out in the coming discussions. As a starting point, the reported adsorption states of water, methanol and ethanol on vacuum-annealed TiO_2(110)–(1×1) have been compiled and summarized in Table 5.1.

5.1 Interaction with Water

The shape of a TPD spectrum is a good indicator of the homogeneity of a surface. It is becoming common practice to use water TPD for assessing the homogeneity of TiO_2(110) surfaces in order to ensure the reproducibility of experiments [139, 146, 148–150]. Figure 5.1 shows two water TPD spectra, one from a smooth surface (larger terraces, smaller step density), and one from a rougher surface (smaller terraces, higher step density). 1 ML of water is desorbed from both surfaces. The desorption peak from the rougher surface is ∼25% broader than the one from the smoother surface, which can be explained by the dissociative adsorption of water at step edges, kinks, etc. [146, 151, 152].

Water TPDs from TiO_2(110) surfaces show two distinct features in the 200–800 K temperature range: one at ∼270 K and one at ∼500 K [67, 139, 146]. The first one is the monolayer peak which originates from water molecules desorbing from 5cTi sites with an adsorption stoichiometry of 1.0 H_2O/Ti [139]. The second peak is a result of recombination of bridging hydroxyls, which form upon adsorption of water at bridging oxygen vacancies (BOVs) [67, 146]. The stoichiometries of these two adsorption processes dictates that, for fully covered surfaces, the ratio of the ∼500 K to ∼270 K peak intensities gives the concentration of BOVs (i.e. number of BOVs per surface unit cell). The BOV

Table 5.1: Data related to adsorption of water, methanol and ethanol on the vacuum annealed $TiO_2(110)$–(1×1) surface.

	Desorption Temperature*	**Adsorption Type**	**Coverage****	**Adsorption Site**	**Reference**
Water	155–160 K	Molecular	Multilayer		[67, 145]
	174–188 K	Molecular	1 ML	2^{nd} layer, bound to bridging oxygen atoms	[67, 139, 145]
	270–284 K	Molecular	1 ML	5cTi atoms	[67, 139, 145]
	490–507 K	Dissociative	0.02–0.08 ML	Bridging oxygen vacancies	[67, 139, 146]
Methanol	145–160 K	Molecular	Multilayer		[139, 147]
	165–180 K	Molecular	0.78 ML	2^{nd} layer, bound to bridging oxygen atoms	[139, 147]
	295–350 K	Molecular & Dissociative	0.66–0.77 ML	5cTi atoms	[139, 147]
	480–500 K	Dissociative	0.02–0.08 ML	Bridging oxygen vacancies	[139, 147]
Ethanol	∼170 K	Molecular	Multilayer		[139]
	∼190 K	Molecular	0.51 ML	2^{nd} layer, bound to bridging oxygen atoms	[139]
	∼340 K	Molecular & Dissociative	0.62–0.76 ML	5cTi atoms	[139]
	∼500 K	Dissociative	0.02–0.08 ML	Bridging oxygen vacancies	[139]

***** Peak temperature for saturation coverage

****** $1\text{ML} = 5.4 \times 10^{14}\ \text{cm}^{-2}$

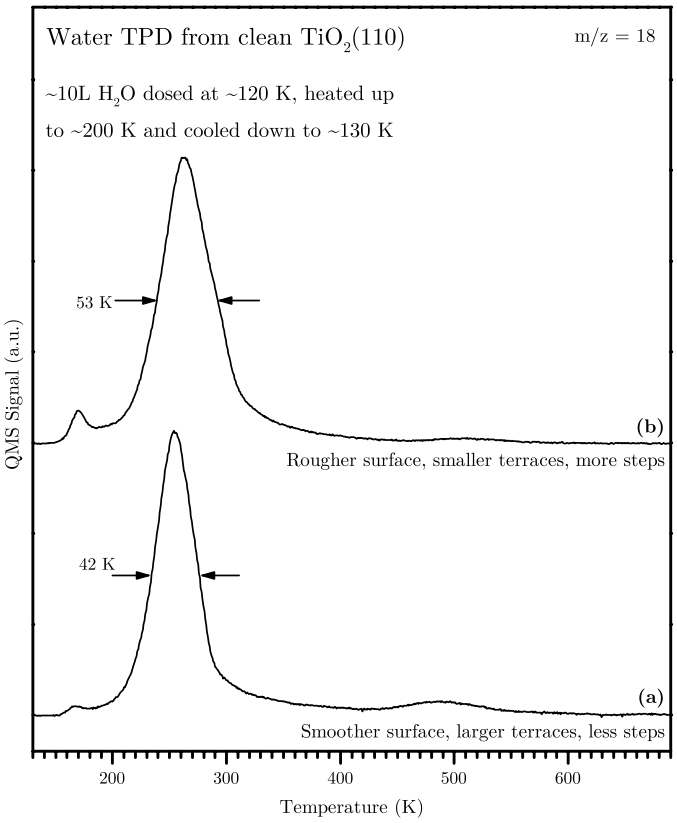

Figure 5.1: Water TPD spectra from two clean TiO_2(110) surfaces differing in their surface roughness and concentration of bridging oxygen vacancies. (a) Smoother surface, with larger terraces and less steps; (b) rougher surface with smaller terraces and more steps. Baseline subtraction was applied to both curves. The peak heights were normalized.

concentration can be correlated with the annealing history of the sample [66], and the temperature at which the sample was last annealed [153].

Figure 5.2 shows water TPD spectra from surfaces prepared according to procedure 4. The spectra are stacked in the order of increasing MoO_x coverage. The distinct ∼500 K desorption peak can be seen more clearly from the 4× magnified spectrum from the clean TiO_2 surface. The effect of MoO_x addition is quite clear even at small Mo concentrations. The intensity of the ∼500 K peak decreases with a slight shift (∼20 K) to lower temperatures for surfaces containing 1.3% and 3.1% Mo. This suggests that a part of the BOVs are blocked by the deposition of MoO_x.

The spectrum from the 6.0% Mo containing surface shows some high temperature desorption. However, a distinct peak can not be identified at ∼500 K anymore. The new desorption feature is broad, possibly due to increased surface heterogeneity. Broad high temperature desorption features are also present for the surfaces containing higher amounts

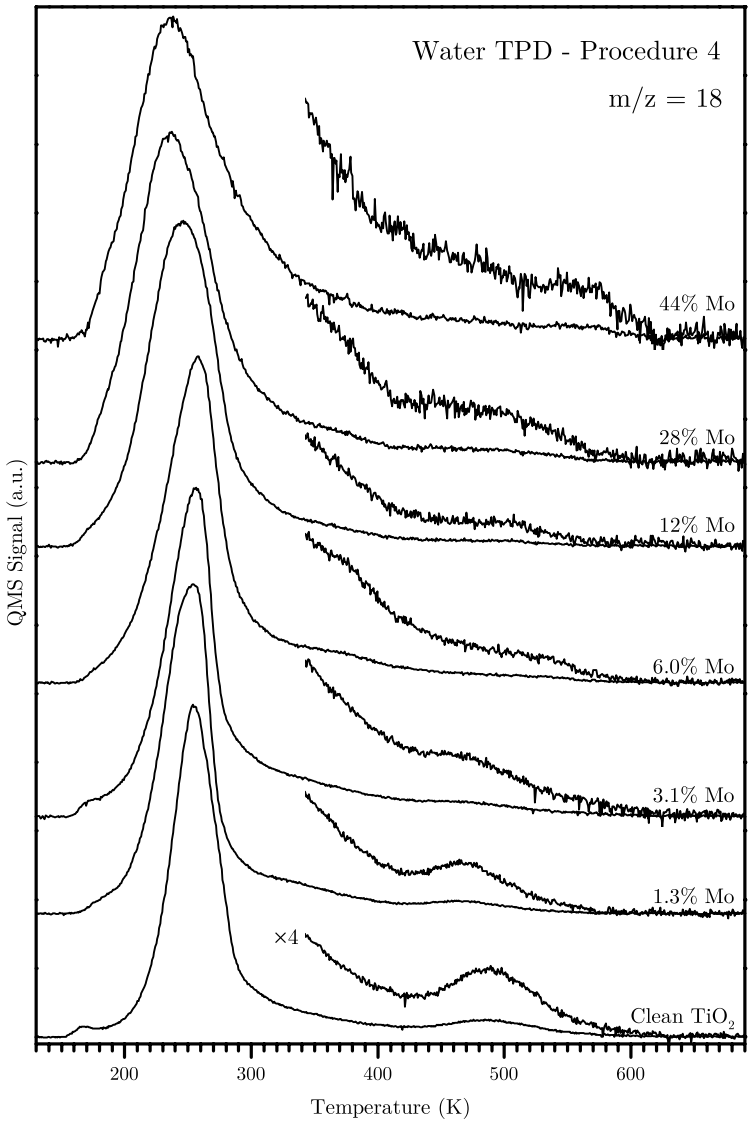

Figure 5.2: Water TPD spectra for surfaces prepared according to procedure 4 with different molybdenum concentrations. All spectra are taken using 0.5 K/s heating rate, after dosing ∼10 L H_2O at ∼120 K, heating up to ∼200 K and cooling down again. Each mixed oxide surface was prepared by deposition of Mo onto the surface prepared in the previous step, except for the 1.3% Mo containing surface. The spectra are normalized to identical maximum intensities, since the QMS detection efficiency was found to vary somewhat between different measurements. The part of the spectra above 350 K was multiplied by a factor of 4 and is shown in addition.

of Mo.

The monolayer peak broadens with increasing Mo coverage. Up to 6% Mo concentration the broadening is relatively small. It becomes prominent with further MoO_x addition. Up to 44% Mo concentration, the broadening is almost entirely towards the low-temperature side. This indicates that the new adsorption sites bind water molecules weaker. The FWHM nearly doubles when going from the clean surface to the 44% Mo containing surface. Broadening towards the high-temperature side is also prominent at 44% Mo concentration.

Even though the monolayer desorption peak broadens towards lower temperatures, the desorption signal at 255 K remains intense even at 44% Mo concentration ($\sim$1.5 MoO_2 ML). It is not unlikely that some part of this signal originates from the 5cTi sites which would mean that the MoO_x layer is not closed. This would be in accordance with the (1×1) LEED patterns obtained from the layers with high Mo content (see Figure 4.3(b)), assuming that the pattern is due to the open patches of TiO_2.

Water TPD spectra for surfaces prepared according to procedures 1, 2 and 6 are shown in Figure 5.3. The spectra from 10%, 68% and 81% Mo containing layers are presented along with the spectra from a clean TiO_2 surface and the thick MoO_3 layer prepared in the high-pressure cell. The peak at $\sim$255 K disappears gradually with increasing Mo concentration. For spectrum (b), in addition to broadening towards lower temperatures, broadening towards higher temperatures is also prominent, which may be due to the nature of the preparation procedure. Procedure 2 involves the co-deposition of Ti and Mo and produces surfaces which are more inhomogeneous than procedure 4 (see the STM images of the layers prepared according to these two procedures in Chapter 4). The spectra (c) and (d) are from layers which were initially prepared according to procedure 1 and then subjected to a series of treatments before the TPD experiments. The details of the preparations have been given in section 4.2. The final treatment before taking spectrum (d) (81% Mo) was annealing at 900 K in UHV whereas it was annealing at 950 K in $\sim 1 \times 10^{-6}$ mbar O_2 for spectrum (c) (68% Mo). According to XPS the 68% Mo containing layer is more oxidized than the 81% Mo containing layer. The 68% Mo containing layer shows the $c(2 \times 2)$ superstructure in LEED whereas the 81% Mo containing layer shows background only. The spectrum from the 81% Mo containing surface shows some intensity around 300 K and some just above 200 K. Spectrum (e), which is from a 50 Å thick MoO_3 layer, shows almost no water desorption above $\sim$250 K. This suggests that a Mo atom which is coordinatively saturated with oxygen has little tendency to interact with water. Henry et al. report a similar finding for a surface-oxidized Mo(100) single crystal, such that water adsorbed at 120 K desorbs completely when the sample is heated to room temperature [154]. Furthermore, on the MoO_3(010) surface, DFT calculations predict an adsorption energy in the range of 0.3 eV for water [155]. This adsorption energy corresponds to a desorption temperature around 100–150 K when Redhead's analysis is used with realistic pre-exponential factors (10^9–10^{13} s^{-1}) (see Chapter 2). All these facts combined with what is known from other studies investigating water adsorption on oxides [149, 156] indicate that water adsorbed at coordinatively saturated MoO_x species would not be expected above room temperature. A similar remark can be made for TiO_x as well,

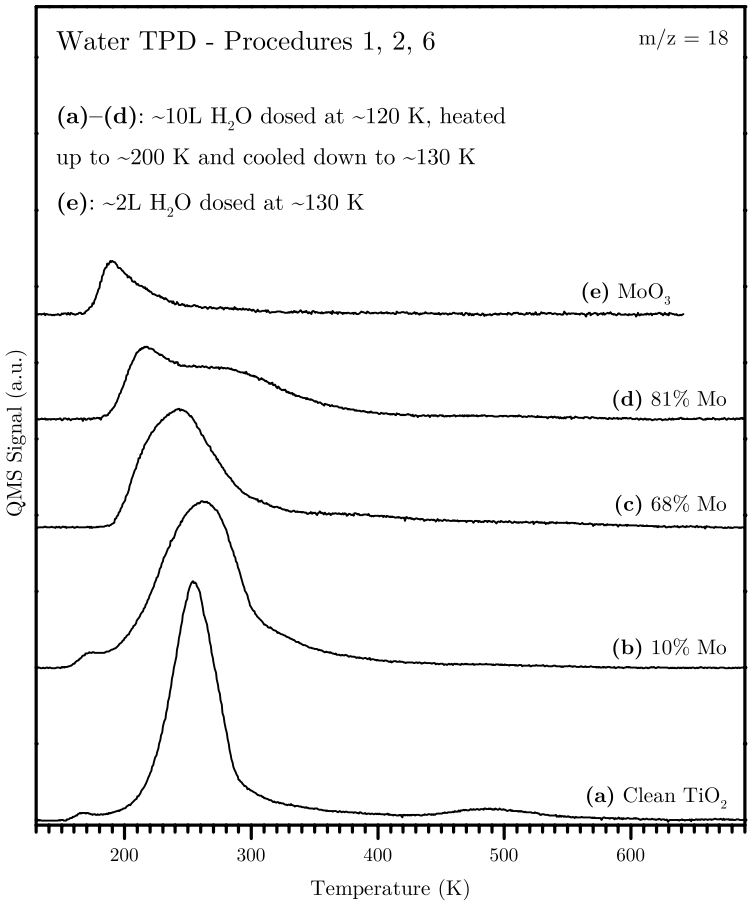

Figure 5.3: Water TPD spectra from layers prepared according to procedures 1, 2 and 6. All spectra are taken using 0.5 K/s heating rate. (a) Clean TiO_2, (b) 10% Mo containing, 35 Å thick layer prepared according to procedure 2 at 900 K, (c) 68% Mo containing layer prepared by annealing layer (d) at 950 K for 10 minutes in UHV and then for 10 minutes in $\sim 1 \times 10^{-6}$ mbar O_2, (d) 81% Mo containing, 33 Å thick layer prepared according to procedure 1 at 850 K and then annealed to 900 K for 10 minutes, (e) 50 Å thick MoO_3 layer prepared according to procedure 6.

such that fully coordinated Ti is not expected to bind water above room temperature [20, 149, 157]. Undercoordinated MoO_x species are not very active for binding water either. A water desorption temperature of 320 K or above has never been reported for oxidized Mo single crystal surfaces [154, 158–161]. As a result, the ∼300 K desorption feature in spectrum (d) may be due to undercoordinated Ti atoms. A desorption peak around 300 K has been reported in the literature for TiO_2(100), which was assigned to dissociatively adsorbed water on the 5cTi atoms of that surface [146]. A Ti site with a similar structure can thus tentatively be predicted for the 81% Mo containing layer.

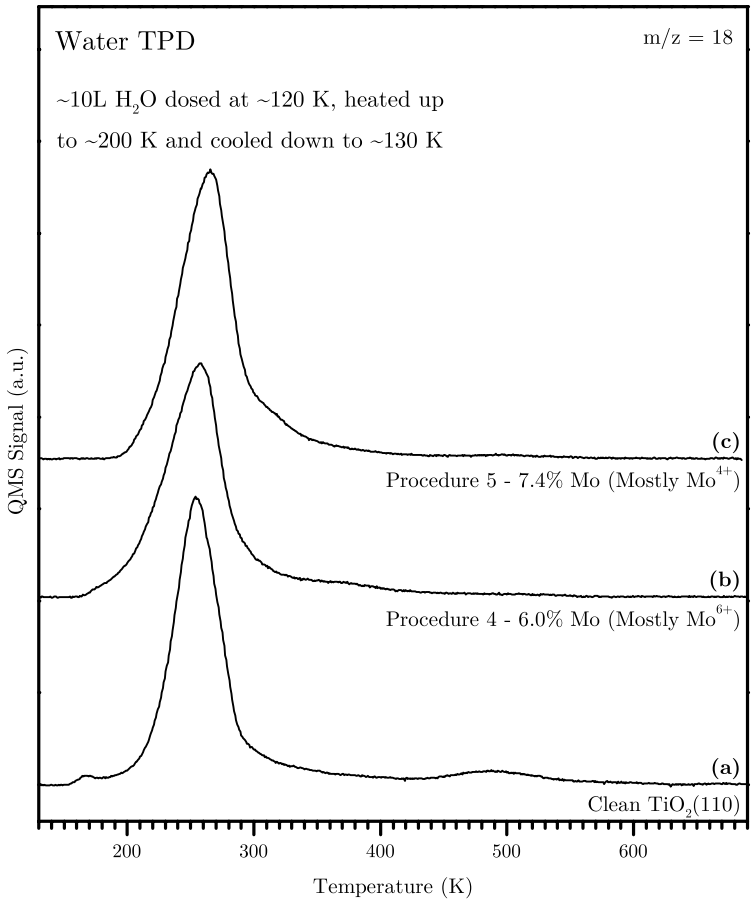

Figure 5.4: Water TPD spectra from layers prepared according to procedures 4 and 5. All spectra were taken using 0.5 K/s heating rate. (a) Clean TiO_2, (b) MoO_x (mostly Mo^{6+}) on TiO_2 prepared according to procedure 4, containing 6.0% Mo (XPS, 70°), (c) MoO_x (mostly Mo^{4+}) on TiO_2 prepared according to procedure 5, containing 7.4% Mo (XPS, 70°).

In Figure 5.4, water TPD spectra from layers prepared according to procedures 4 and 5 with similar Mo concentrations are presented. 6.0% and 7.4% Mo concentration translates to ∼0.2 ML of MoO_2. The difference between the layers is the dominant oxidation state of Mo. For spectrum (b) the layer contains mostly Mo^{6+} whereas for spectrum (c) it contains mainly Mo^{4+}. In both spectra (b) and (c), the intensity of the ∼500 K peak (bridging OH recombination) is reduced significantly. For procedure 4, spectrum (b), the peak has vanished although some high temperature feature is still there, peaking at a slightly higher (∼20 K) temperature. Even that feature, when taken into account, makes up to only 0.7% of the monolayer peak. For procedure 5, spectrum (c), the intensity is 1% of the monolayer peak intensity, which suggests that the vacancy-blocking effect of procedure 4 is also valid in case of procedure 5. The reason why not all the vacancies are blocked despite the higher

Mo concentration for (c) is likely to be related to the oxidation state of Mo, and the use of oxygen in the case of procedure 4. Another explanation would be that the binding site is different for procedure 5, which could involve Mo^{4+} ions directly or indirectly.

Other notable features of spectrum (c) are the shoulder of the monolayer peak around 310 K, and the shift of the monolayer peak temperature to ∼10 K higher relative to the clean surface. It may be speculated that the ∼10 K shift is due to a modification of the 5cTi sites by the presence of Mo. The valence electrons of Mo^{4+}, which have a d^2 configuration, may induce changes on a larger scale if the charge is delocalized. The shoulder at ∼310 K is likely due to a different site. The similar desorption temperature observed in Figure 5.3(d) was thought to be due to an undercoordinated Ti atom. A similar logic may apply here and the shoulder might be assigned to desorption from a newly created site with an undercoordinated Ti atom.

5.2 Interaction with Methanol

As already summarized in Table 5.1, earlier studies identified three distinct methanol desorption features above 250 K for a clean TiO_2(110) surface with bridging oxygen vacancies. The peak at ∼275–295 K and the shoulder at ∼340–350 K were assigned to molecularly and dissociatively adsorbed methanol at 5cTi sites, respectively, while the broad desorption feature at ∼400–500 K was attributed to recombinative desorption of methanol dissociatively adsorbed at BOVs.

TPD spectra of methanol from layers prepared according to procedure 4 are presented in Figure 5.5. The spectra are stacked in the order of increasing MoO_x coverage. The desorption of methanol is accompanied by signals from smaller masses due to the cracking of methanol by the electron beam and the reactions that take place on various surfaces inside the QMS housing. These signals dominate the spectra up to ∼400 K, during the desorption of the methanol monolayer. While it is possible to account properly for the effect of cracking by the electron beam, this is not the case for the effect of the wall reactions. For this reason formaldehyde, methane and water signals are not shown for temperatures below 400 K.

Different from what has been reported in the literature, on the clean TiO_2(110) surface, desorption of significant amounts of formaldehyde and methane was observed at ∼650 K, together with some methanol. Although parts of formaldehyde and methane signals come from the fractionation of this ∼650 K methanol desorption, the effect is definitely not enough to account for the whole signal. It is also worth mentioning that the methane signal peaks at a slightly higher (∼5 K) temperature than methanol and formaldehyde.

In addition to the ∼650 K products, another unprecedented feature of the spectrum from the clean TiO_2 surface is the desorption of water at ∼500 K. Henderson reports a "small amount of H_2O desorption" in his methanol TPD, without mentioning the desorption temperature, and assigns it to water adsorption from the residual gas atmosphere [147]. The author also shows that pre-adsorbed water at oxygen vacancies can be removed (by ∼50%) by dosing methanol on top. The remaining water at the vacancies desorbs at ∼500 K which may mean that the water that he believes adsorbs from the residual gas

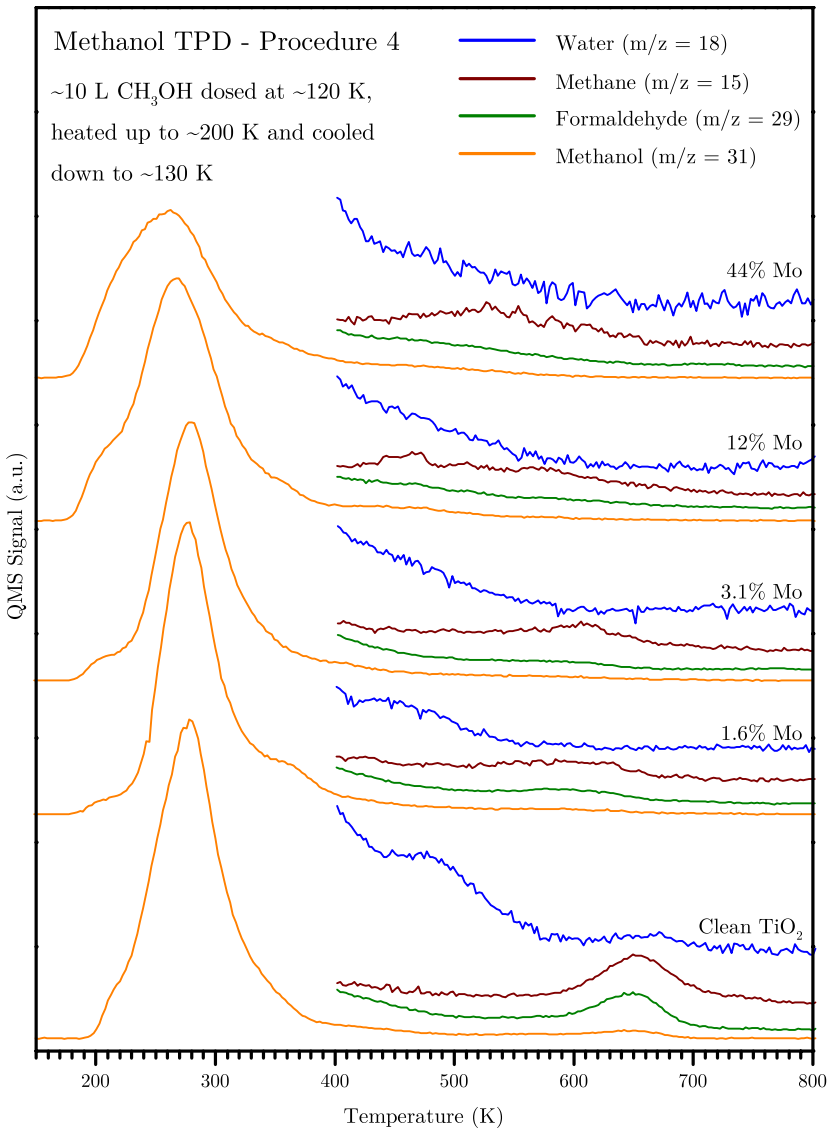

Figure 5.5: Methanol TPD spectra for surfaces prepared according to procedure 4 with different molybdenum concentrations. Each mixed oxide surface was prepared by deposition of Mo onto the surface prepared in the previous step. For water, formaldehyde and methane, the data are not shown below 400 K because they are dominated by the fragmentation and wall-reaction products of the monolayer methanol. Masses 15, 18 and 29 are scaled with their respective sensitivity factors. All spectra are taken using 0.5 K/s heating rate.

also desorbs at ∼500 K. On the other hand, the amount of methanol desorbing around 500 K is the same for a water pre-covered surface and a clean surface. This may mean that the adsorption from the residual gas populates a significant part of the vacancies (∼50%).

In our case, the desorption of water at ∼500 K and the other products at ∼650 K are likely linked, although the reason why this difference from the published results exists in the first place, is not clear. The link between these two additional desorption features is the stabilization of methoxies at the bridging oxygen vacancies. This stabilization is a consequence of the hydroxyl recombination process at ∼500 K. These hydroxyls originate from methanol dissociation. The removal of each hydroxyl leaves a methoxy on the surface without any hydrogen to recombine with. These methoxies are stable only up to ∼650 K, where they react with each other and disproportionate to form methanol and formaldehyde or methane and formaldehyde, depending on the retaining or breaking of the C–O bond. This type of mechanism has already been observed in methanol TPDs from oxygen pre-dosed [147] or "stoichiometric" [162] (i.e. annealed and cooled down in O_2) TiO_2(110) surfaces, resulting in the production of formaldehyde and methanol at similar temperatures. In these cases, hydrogen that is abstracted from methanol upon adsorption is removed by the extra oxygen on the surface, desorbing as water, hence leaving stable methoxies on the surface which recombine and disproportionate at higher temperature. In the literature, formation of methane has only been observed for defective, oxygen-poor surfaces, which have a tendency to abstract oxygen from adsorbates [162].

The presence of MoO_x affects the high temperature desorption features significantly. Even at the lowest Mo concentration (1.6%), the decrease in intensity is prominent. The decrease is accompanied by a shift of the peak temperature to ∼600 K. Further increase in the Mo concentration does not result in much change in the intensity of the high temperature features but they broaden and shift to even lower temperatures. At 44% Mo concentration, formaldehyde desorption goes effectively to zero while methane desorption remains and becomes the primary desorption product at high temperature. The monolayer desorption peak still contains significant intensity at ∼280 K, which means 5cTi sites of the TiO_2 surface are still exposed, in accordance with the TiO_2(110)–(1×1) LEED pattern observed from surfaces with comparable Mo contents. The broadening of the monolayer peak is prominent towards lower temperatures whereas very little change is observed at the high temperature side. This is in accordance with the reported desorption temperatures in the literature for methanol molecularly bound to MoO_x surfaces [154, 161, 163, 164].

Kim et al. investigated the dehydrogenation of methanol on monooxo MoO_3 clusters supported on TiO_2(110) with DFT calculations and found a path towards formaldehyde with an activation energy of 1.40 eV [165]. The rate determining step involves the breaking of a C–H bond, and the mechanism does not involve methoxy disproportionation. This activation energy inserted into the Arrhenius equation with a pre-exponential factor of 10^{12} s^{-1} yields a first order rate constant of 0.15 s^{-1} at 550 K. Redhead analysis with an activation energy of 1.40 eV would correspond to a desorption peak temperature of about 520 K assuming the same pre-exponential factor. However, our TPD spectra show that only a small amount of formaldehyde is produced in this temperature range which means that the process reported by Kim et al. applies at most to a small part of the surface

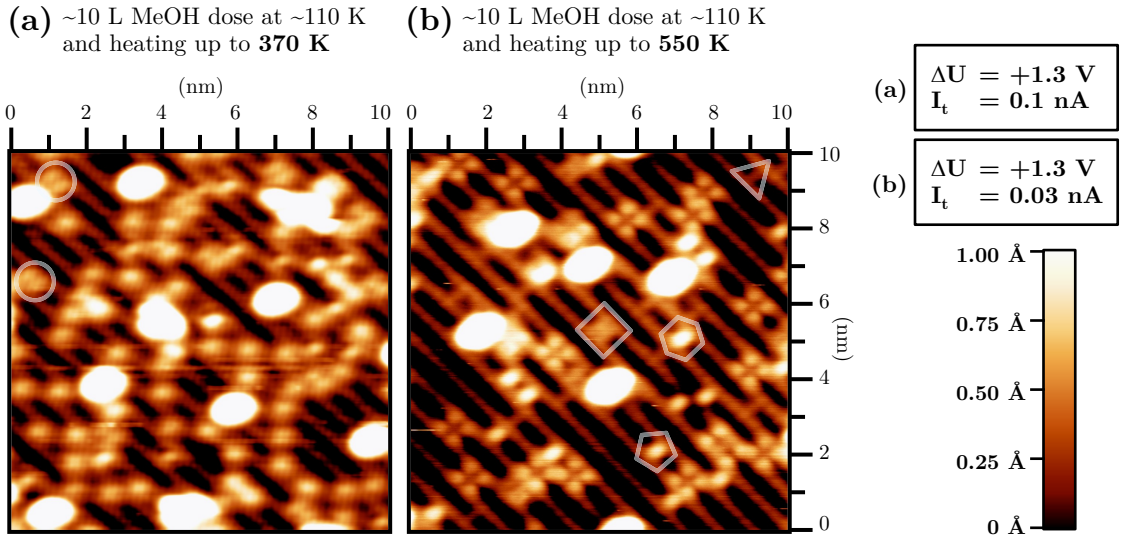

Figure 5.6: STM images from layers prepared according to procedure 4 and contain ∼1% Mo. Images were taken after an exposure of ∼10 L methanol at ∼110 K and consecutive heating to (a) 370 K in UHV and (b) 550 K in UHV. The encircled features have been assigned to the feature X2, which is also visible in the second image as the bright squares. The features enclosed in other shapes have a different height each and are not assigned to anything conclusively.

reactions.

In order to gain more insight about the adsorption of methanol on a MoO_x containing surface, a surface containing ∼1% Mo was imaged with STM after dosing ∼10 L methanol at ∼110 K and heating the sample to 370 K and 550 K. The images are shown in Figure 5.6.

According to the known desorption temperatures from the literature for the different adsorption states of methanol, heating to 370 K should leave methanol adsorbed at BOVs and heating to 550 K should leave nothing on the surface. On the other hand, the high temperature (∼650 K) desorption products observed in our TPD spectra imply that some carbon containing adsorbates must still be present after heating to 550 K, which is exactly what is observed.

None of the features in the two images (except X1) is centred on the bright rows (i.e. 5cTi rows) which implies that all the methanol adsorbed at 5cTi atoms is removed by heating to 370 K, as expected. In image (b), at least 4 different types of bright features which connect the bright rows are present. The features differ by their brightness. At least one of these features is likely a methoxy. It was already mentioned in the context of formaldehyde formation on the clean TiO_2 surface that the stabilization of the methoxies is due to the recombinative desorption of the bridging hydroxyls at ∼550 K. The features enclosed in squares are thought to be BOVs that formed upon this OH recombination.

The features which were previously named X1 are seen in both images. The typical

height of this feature is 2.5 Å for methanol-free surfaces. The same height (2.5 Å) is observed for both images in Figure 5.6. Similarly, the heights of the feature X2 (which looks like a "bright square") are very close for image (b) and images from methanol-free surfaces. These observations indicate that X1 and X2 features are not strong adsorption sites for methanol.

Methanol TPD spectra from layers prepared according to procedures 1, 2 and 6 are shown in Figure 5.7. The formaldehyde yield at ∼650 K is smaller for the 10% Mo containing layer than for TiO_2(110) and is zero in the other spectra. The mass signals 29 and 31 differ only by a multiplication factor throughout the shown temperature range (> 400 K), so the formaldehyde signals observed in the spectra (c) to (e) are probably all due to the electron beam cracking and the wall reactions in the mass spectrometer. The same linear scaling also applies to the methane signals (m/z = 16, not shown) for the same spectra indicating the absence of methane formation.

A significant difference between methanol and water adsorption on clean TiO_2(110) is that, there is a distinct state for methanol (but not for water) at ∼330 K which is related to dissociative adsorption at 5cTi sites. This feature is also observed in all the spectra in Figure 5.7 except (e), indicating the presence of the same or a similar undercoordinated Ti site which can dissociate methanol. A counterintuitive result is that the intensity of the ∼330 K feature is smaller in (c) (68% Mo) as compared to (d) (81% Mo) although the former layer contains more Ti. The layer containing 68% Mo was obtained by annealing the 81% Mo containing layer in O_2 (see section 4.2 for details). The oxidized Mo sublimes as MoO_3 (hence the decrease in the Mo concentration). Significant changes in the surface structure can be expected upon MoO_3 sublimation. The number of 5cTi sites possibly decreases with the oxidation treatment, which leads to the observed decrease in the ∼330 K desorption intensity.

The desorption features below 300 K shift towards lower temperatures as the Mo concentration increases. Methanol desorbs dominantly between 200–250 K in spectra (c) and (d), which is consistent with the desorption temperatures measured on oxidized Mo single crystals [154, 161, 163, 164].

Adsorption of ∼10 L methanol onto a 10% Mo containing layer (procedure 2) at 110 K and stepwise heating to higher temperatures has been monitored by XPS. C1s and Mo3d spectra are shown in Figure 5.8(a). Initially only very little carbon (contaminant) is present on the surface and Mo shows a dominant oxidation state of 6+. Upon multilayer methanol adsorption, some Mo3d intensity shifts to lower binding energies, indicative of reduction. When the surface is heated up to 330 K, only methoxies remain on the surface and the dominant oxidation state of molybdenum is 4+, together with some 6+. The C1s binding energies of methanol and methoxy are more or less consistent with the literature [162]. Heating to 500 K restores the initial oxidation state of Mo and no carbon remains on the surface except for the initial small contamination.

Although, at first, the data shown in Figure 5.8(a) seem to suggest the reduction of Mo^{6+} to Mo^{4+} via methanol adsorption, the phenomenon turned out to be an artefact of XPS. When the same surface was dosed with the same amount of methanol and heated up to 330 K without exposing it to x-rays, the oxidation state of Mo turned out to be identical

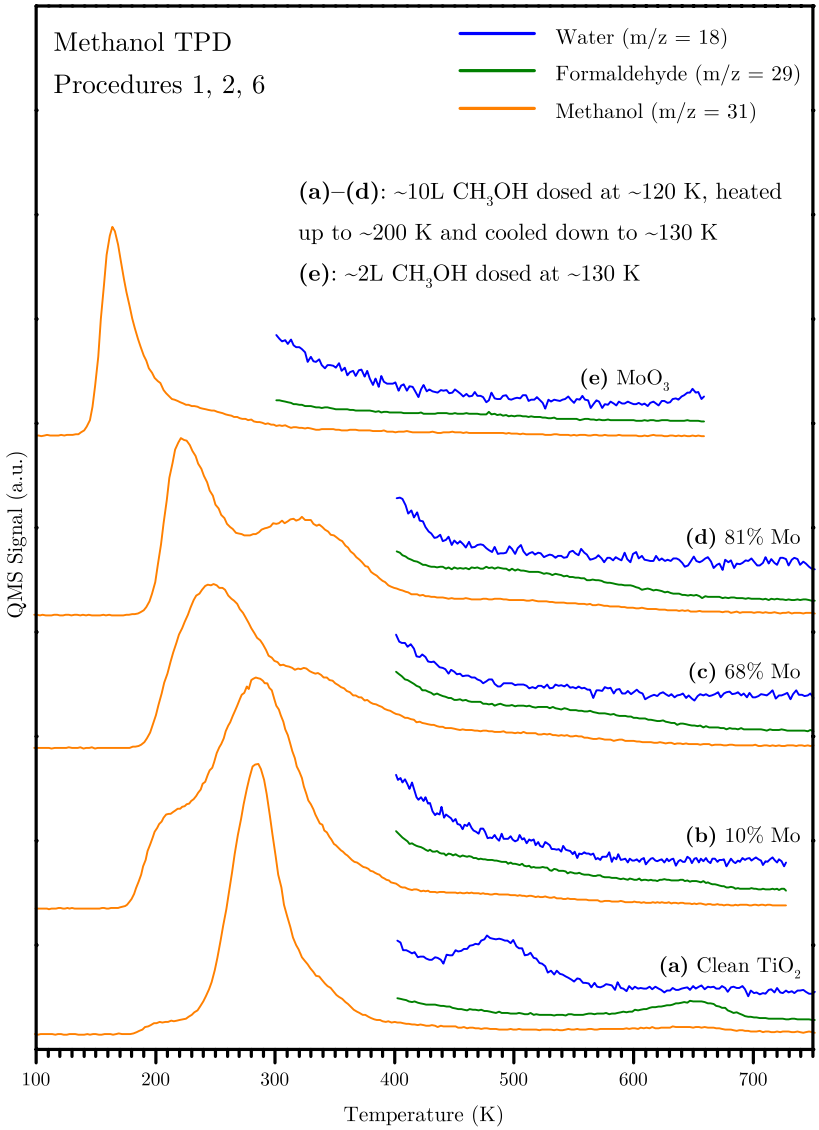

Figure 5.7: Methanol TPD spectra for surfaces prepared according to procedure 1, 2 and 6 with different molybdenum concentrations. For water and formaldehyde, the data are not shown below a certain temperature because they are dominated by the fragmentation and wall-reaction products of the desorbing methanol. Masses 18 and 29 are scaled with their respective sensitivity factors. All spectra are taken using 0.5 K/s heating rate. (a) Clean TiO_2, (b) 10% Mo containing, 35 Å thick layer prepared according to procedure 2 at 900 K, (c) 68% Mo containing layer prepared by annealing layer (d) at 950 K for 10 minutes in UHV and then for 10 minutes in $\sim 1 \times 10^{-6}$ mbar O_2, (d) 81% Mo containing, 33 Å thick layer prepared according to procedure 1 at 850 K and then annealed to 900 K for 10 minutes, (e) 50 Å thick MoO_3 layer prepared according to procedure 6.

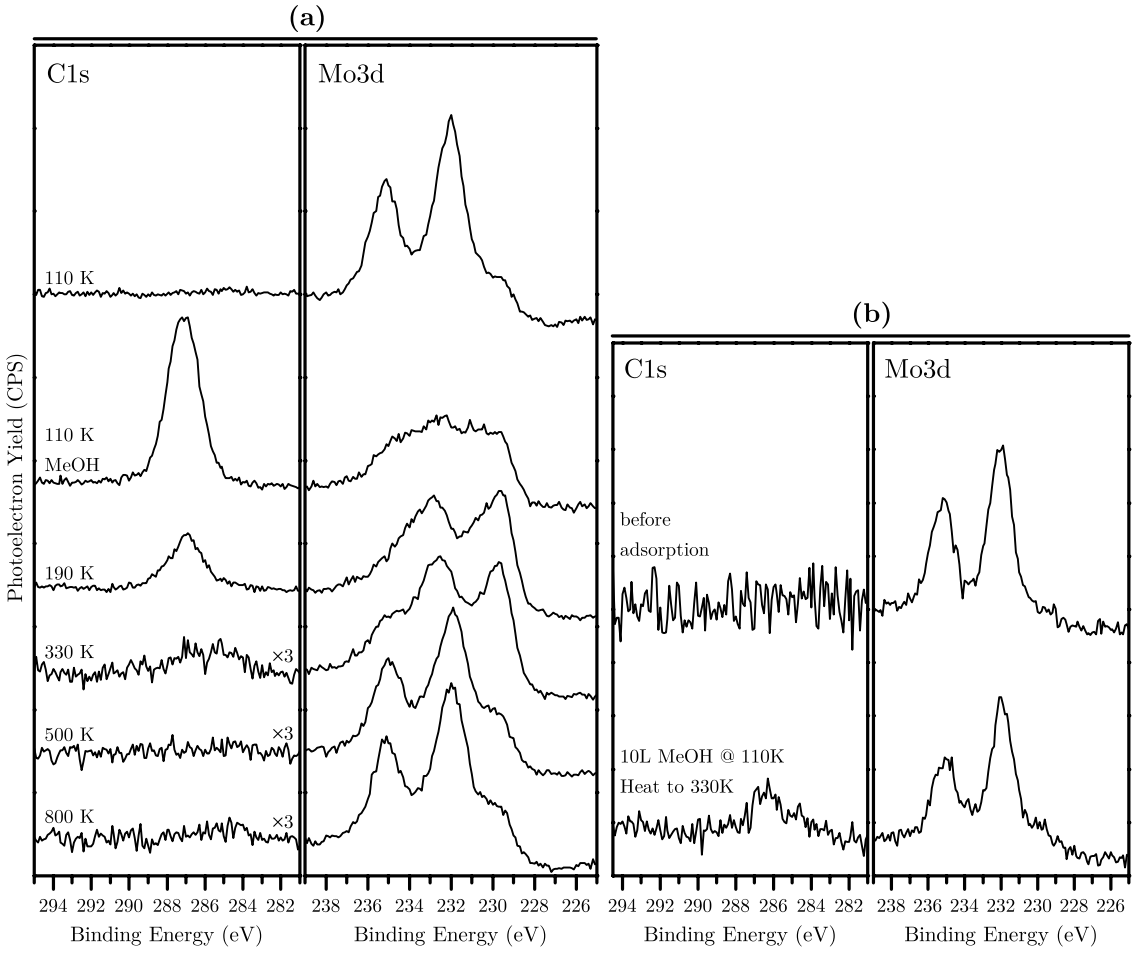

Figure 5.8: C1s and Mo3d XPS spectra from mixed layers, illustrating the reduction of Mo^{6+} to Mo^{4+} due to a combined effect of adsorbed methanol and irradiation from the x-ray gun. (a) 35 Å thick, 10% Mo containing layer, prepared according to procedure 2. The spectra are from the clean surface, after adsorbing 10 L methanol and after stepwise heating to the indicated temperatures. The spectra were acquired at the indicated temperatures except for the one labelled as 800 K, which has been taken at room temperature after heating the sample to 800 K. (b) 3.5% Mo containing layer prepared according to procedure 4. The spectra were acquired before adsorption and after adsorbing 10 L of methanol at 100 K with consecutive heating to 330 K. The sample was not exposed to the x-ray gun in between.

to its initial oxidation state (i.e. Mo^{6+} mostly). The data from the control experiment are presented in part (b) of Figure 5.8. Methoxies are visible as a small peak in the C1s spectrum. The Mo3d spectra are almost identical, maybe with a small low-binding-energy shoulder after adsorption and heating. This shows that reduction of Mo requires adsorbed methanol being hit by x-rays from the gun or photoelectrons from the sample. Irradiating a methanol-free surface does not lead to the reduction of Mo^{6+}, at least not at the same rate, thus reduction is possibly a consequence of proton-coupled electron transfer from methanol to the MoO_x cluster, forming OH groups and effectively reducing the Mo ion, instead of removal of oxygen from MoO_x.

Spectrum (c) in Figure 5.9 is from a layer prepared according to procedure 5 and is shown together with spectra that belong to a layer of similar Mo concentration prepared according to procedure 4, (b), and clean TiO_2(110), (a). The formaldehyde desorption observed on the clean TiO_2 surface at high temperature is suppressed to a smaller extent in (c) as compared to (b). The discussion made in the context of Figure 5.4 (water adsorption on the same surfaces), seems to be valid here as well. The use of oxygen in procedure 4 is probably responsible for the blocking of more vacancies than in the case of procedure 5.

The shoulder around 360 K in spectrum (c) is also similar to the shoulder observed for water at ∼310 K in Figure 5.4(c). The relatively high desorption temperature had been interpreted as a sign of desorption from a Ti site rather than a Mo site. In the case of methanol two desorption channels have been reported in the literature from an oxidized Mo(100) surface: at 210 K and 370 K. The latter one matches well with the shoulder observed in spectrum (c). Another explanation for the shoulder could be a different kind of 5cTi site created by the presence of Mo, since the temperature (∼360 K) is in the range for the desorption of dissociatively adsorbed methanol bound to titanium atoms.

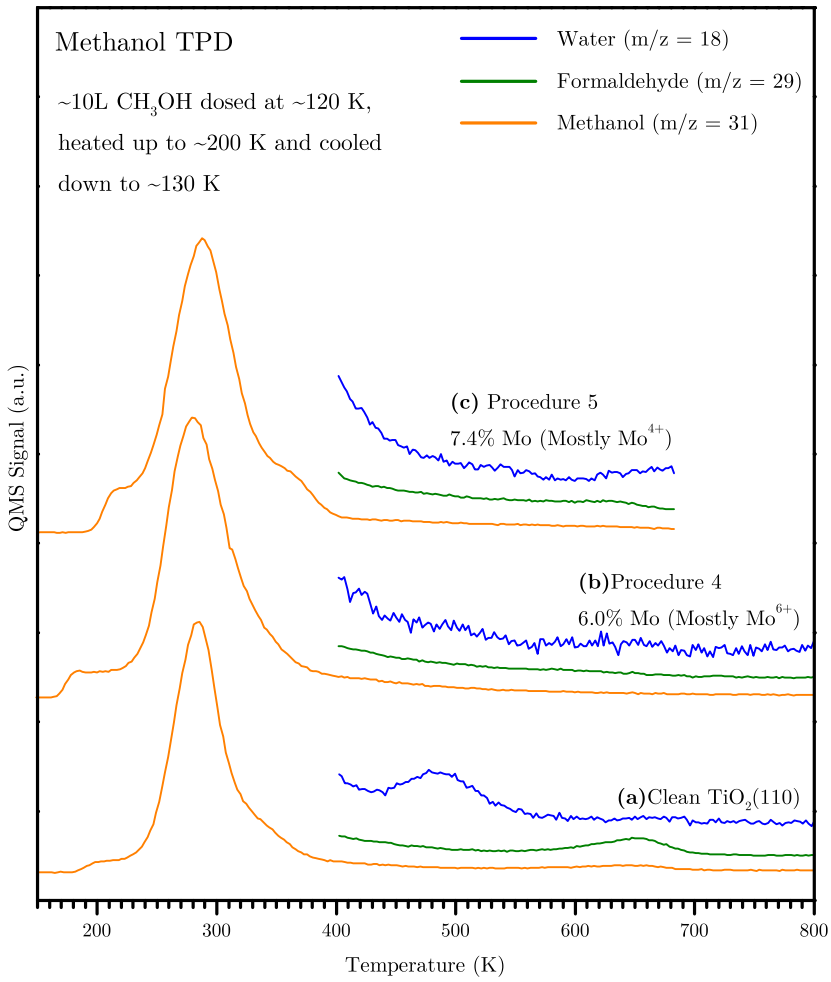

Figure 5.9: Methanol TPD spectra from layers prepared according to procedure 4 and 5. For water and formaldehyde, the data are not shown below 400 K because they are dominated by the fragmentation and wall-reaction products of the monolayer methanol. Masses 18 and 29 are scaled with their respective sensitivity factors. All spectra are taken using 0.5 K/s heating rate. (a) Clean TiO_2, (b) MoO_x (mostly Mo^{6+}) on TiO_2 prepared according to procedure 4, containing 6.0% Mo (XPS, 70°), (c) MoO_x (mostly Mo^{4+}) on TiO_2 prepared according to procedure 5, containing 7.4% Mo (XPS, 70°).

5.3 Interaction with Ethanol

On clean TiO_2(110), all the simple alcohols except methanol react primarily through a dehydrogenation pathway, yielding water and the corresponding alkene [166]. Dehydrogenation takes place primarily at high (> 500 K) temperatures and partially at low (300–450 K) temperatures [150, 166]. It has been shown that the low-temperature mechanism does not require the presence of bridging oxygen vacancies whereas the high-temperature mechanism does [7]. Ethanol TPD spectra from surfaces prepared according to procedure 4 are presented in Figure 5.10 as a function of the Mo concentration. The spectra show predominant production of ethylene, in accordance with the literature. The low temperature channel is not distinguishable in our case because of the lack of proper data which would allow its deconvolution.

The features at ∼295 K and ∼350 K are assigned to molecularly and dissociatively adsorbed ethanol at 5cTi sites, and the small feature at ∼420 K is due to desorption of dissociatively adsorbed ethanol at BOVs as already summarized in Table 5.1. At ∼600 K ethylene, acetaldehyde and water desorb together with additional ethanol.

A concentration of 1.6% of Mo leads to a dramatic decrease of the amount of ethylene (as well as acetaldehyde, ethanol and water) at ∼600 K, accompanied by a decrease in the peak temperature. The ethylene and formaldehyde yields decrease by ∼50% whereas the ethanol and water yield decreases by ∼60%. The numbers are in accordance with the decrease in the number of bridging oxygen vacancies (∼50%). With increasing Mo concentration the peaks become wider and shift to lower temperatures with the ethylene desorption peak maximum finally reaching ∼500 K. The change in the shape of the monolayer peak is also in parallel with the changes observed in water and methanol. Broadening towards lower temperatures suggests partial blocking of the 5cTi sites and the presence of MoO_x.

Figure 5.11 shows ethanol TPD spectra from layers prepared according to procedures 1, 2 and 6. As in Figure 5.3 and Figure 5.7, the Mo concentration varies from 0 to ∼100%. Similar conclusions to the case of methanol can be drawn. Increasing the Mo concentration shifts some methanol desorption intensity towards ∼200 K and some intensity remains around 320–350 K as long as there is some titanium in the system. The MoO_3 surface shows almost no ethanol desorption above 300 K. A very small amount of ethylene desorption can still be observed near 500 K, which is probably due to steps, kinks, etc. since the structure of the layer is rather inhomogeneous as evident from the STM image in Figure 4.30.

Ethanol TPD spectra from a 7.4% Mo containing layer prepared according to procedure 5, (c), are presented in Figure 5.12 along with spectra from a 6.0% Mo containing layer, (b), and clean TiO_2(110), (a). Again, a similar behaviour to the case of methanol (Figure 5.9) is observed. A small shoulder develops around 380 K, which can be assigned to desorption from either a Mo (probably Mo^{4+} and undercoordinated) or from a new kind of 5cTi site. An interesting feature is that the high temperature ethylene desorption peak comes at about the same temperature for (a) and (c), whereas it comes at a ∼20 K lower temperature for (b). The difference between (b) and (c) is mainly the oxidation state of Mo. In the case of (b) it is mainly Mo^{6+} whereas for (c) it is mainly Mo^{4+}. As previously discussed for

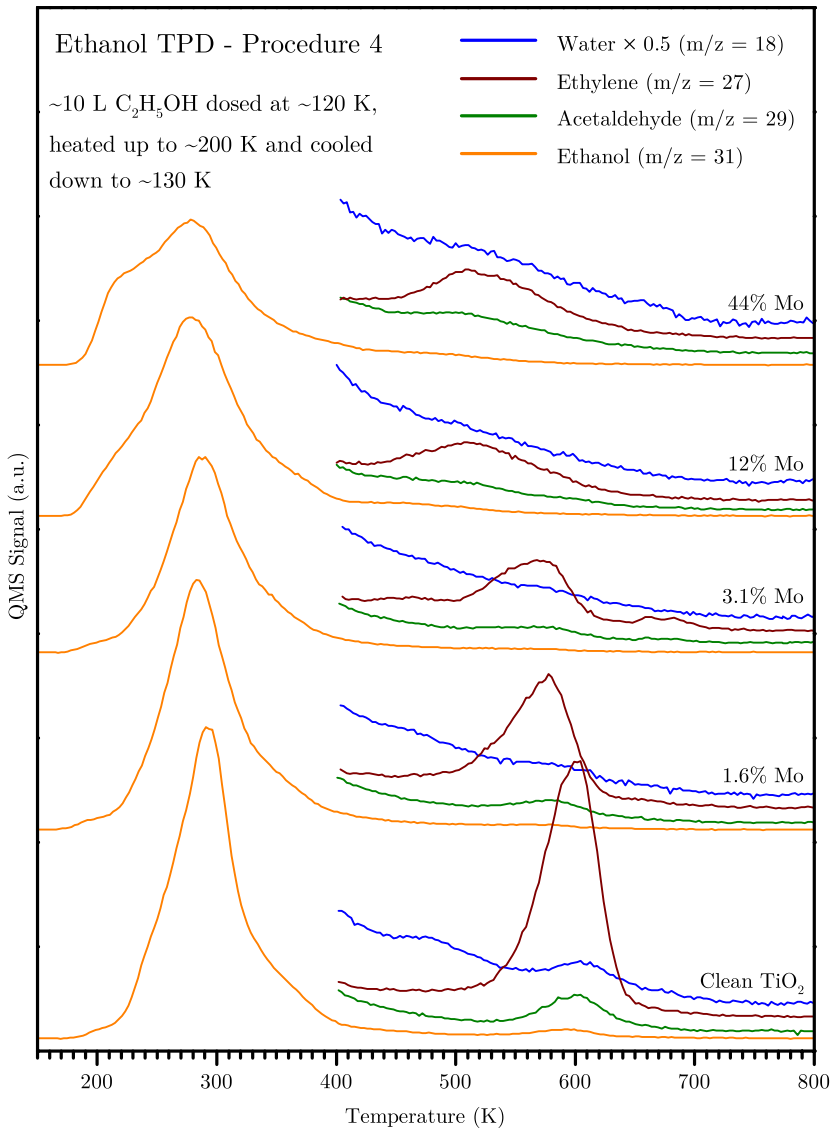

Figure 5.10: Ethanol TPD spectra for surfaces prepared according to procedure 4 with different molybdenum concentrations. Each mixed oxide surface was prepared by deposition of Mo onto the surface prepared in the previous step. For water, acetaldehyde and ethylene, the data are not shown below 400 K because they are dominated by the fragmentation and wall-reaction products of the monolayer ethanol. Masses 18, 27 and 29 are scaled with their respective sensitivity factors. Mass 18 is scaled by an additional factor of 0.5.

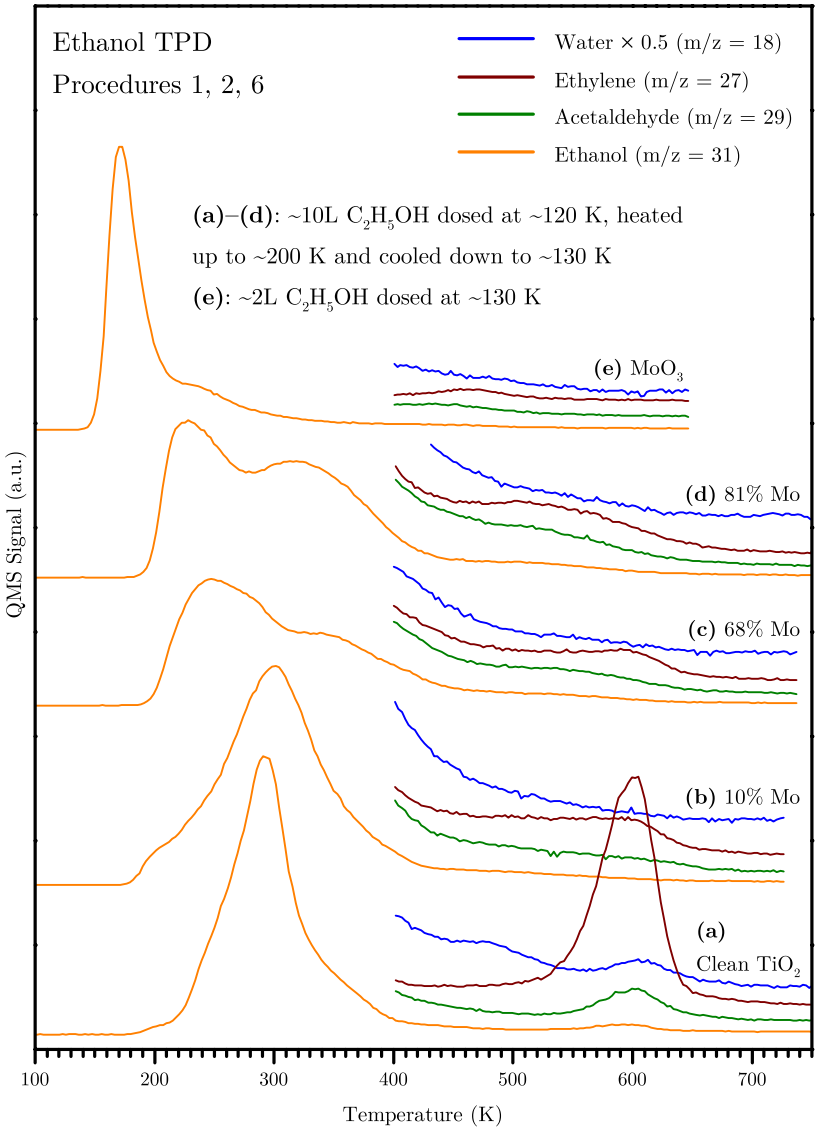

Figure 5.11: Ethanol TPD spectra for surfaces prepared according to procedure 1, 2 and 6 with different molybdenum concentrations. For water, acetaldehyde, and ethylene the data are not shown below 400 K because they are dominated by the fragmentation and wall-reaction products of the monolayer ethanol. Masses 18, 27 and 29 are scaled with their respective sensitivity factors. Mass 18 is scaled by an additional factor of 0.5. All spectra are taken using 0.5 K/s heating rate. (a) Clean TiO_2, (b) 10% Mo containing, 35 Å thick layer prepared according to procedure 2 at 900 K, (c) 68% Mo containing layer prepared by annealing layer (d) at 950 K for 10 minutes in UHV and then for 10 minutes in $\sim 1 \times 10^{-6}$ mbar O_2, (d) 81% Mo containing, 33 Å thick layer prepared according to procedure 1 at 850 K and then annealed to 900 K for 10 minutes, (e) 50 Å thick MoO_3 layer prepared according to procedure 6.

the case of water adsorption, the extra valence electrons of Mo may be inducing changes on the nearby charge density or atomic positions. Such perturbations may influence the transition-state structure of the reaction and shift the desorption temperature. In this case, the high-temperature ethylene desorption temperatures for (a) and (c) being the same, suggests a very similar electronic and/or geometric structure for the active sites of these two surfaces.

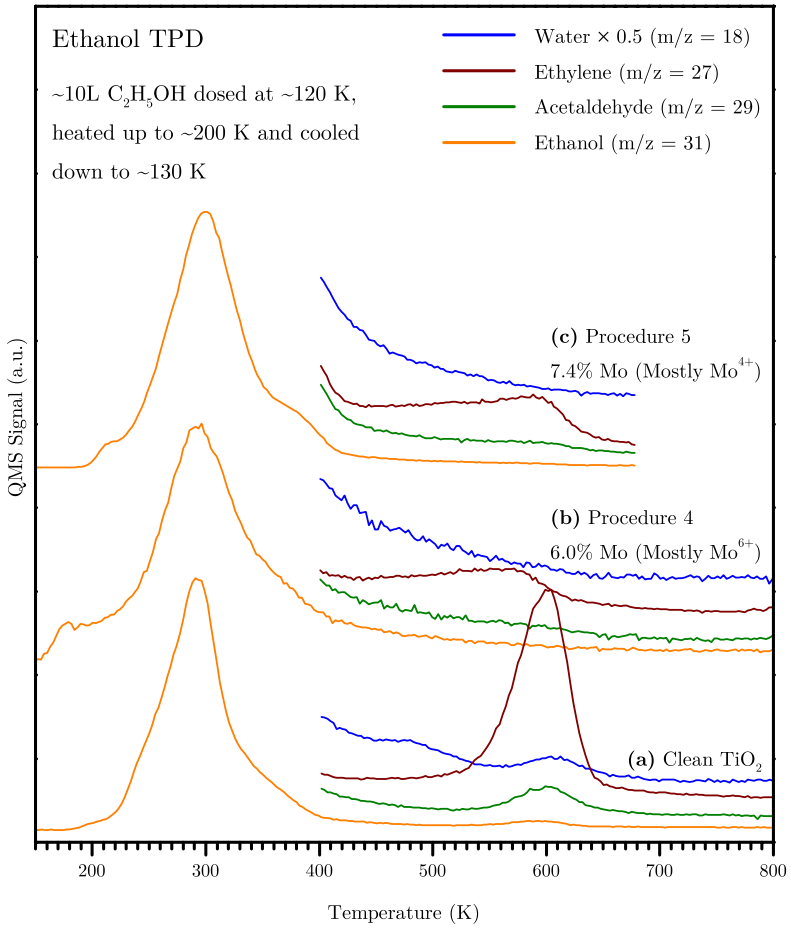

Figure 5.12: Ethanol TPD spectra from layers prepared according to procedure 4 and 5. For water, acetaldehyde, and ethylene the data are not shown below 400 K because they are dominated by the fragmentation and wall-reaction products of the monolayer ethanol. Masses 18, 27 and 29 are scaled with their respective sensitivity factors. Mass 18 is scaled by an additional factor of 0.5. All spectra are taken using 0.5 K/s heating rate. (a) Clean TiO_2, (b) MoO_x (mostly Mo^{6+}) on TiO_2 prepared according to procedure 4, containing 6.0% Mo (XPS, 70°), (c) MoO_x (mostly Mo^{4+}) on TiO_2 prepared according to procedure 5, containing 7.4% Mo (XPS, 70°).

5.4 Summary

In summary, some general remarks can be made regarding the interaction of water, methanol and ethanol with the mixed layers. At low Mo concentrations, the decrease in the number of oxygen vacancies suppresses the vacancy-related products which form at high temperatures. The products desorb at lower temperatures for layers containing Mo^{6+} as compared to clean $TiO_2(110)$ and layers containing Mo^{4+}. The binding of water, methanol and ethanol to MoO_x is weaker as compared to $TiO_2(110)$. Furthermore, adsorption on MoO_3 is even weaker as compared to MoO_2-like layers. Desorption from MoO_x mostly takes place below 250 K, thus dissociation of the adsorbates is not expected. Among the mixed layers studied for chemical reactivity, none of them is promising for dehydrogenation of methanol/ethanol or dehydration of ethanol. In fact, the $TiO_2(110)$ surface seems to be more active by itself.

6 SUMMARY AND OUTLOOK

Oxides make up an important class of catalysts that are mainly important for selective oxidation of organic molecules. There is also great potential for oxides in methane activation and water splitting reactions, which are likely to be implemented at large scales in the future as possible solutions to the energy conversion problem. In order to obtain oxides with the desired catalytic properties for these reactions and others, doping may be a simple means for modifying the properties of oxides. The greater aim of this thesis was understanding the effect of Mo doping on the catalytic properties of an extensively studied oxide surface—rutile–TiO_2(110). However, complete mixing of an additional component into a "host" material may be hard to achieve in many cases, especially for high concentrations. Indeed, the materials that were investigated in this work (i.e. mixtures of molybdenum oxides and titanium oxides) have little thermodynamical driving force for mixing and obtaining completely mixed layers was difficult. Oxide mixtures containing different amounts of Mo were prepared and characterized.

The oxide mixtures were prepared as thin layers (< 5 nm) on single-crystalline TiO_2(110) substrates. Preparation of the layers was carried out by evaporating Ti and Mo metals onto the substrate in UHV or an O_2 atmosphere, and different preparation procedures were tested to get better mixing. Substrate temperature, deposition period of each metal, ambient atmosphere, and post-annealing treatments were varied to control the structure of the layers. The preparation procedures were classified into six categories, and results were reported in separate sections. For the characterization of reactivity, dehydrogenation and dehydration of alcohols (methanol and ethanol) were investigated. The interaction of water with the layers was also studied, and all reactivity studies employed temperature programmed desorption (TPD) as the main technique.

In procedure 1, where the deposition of molybdenum and titanium was carried out simultaneously in oxygen at high substrate temperature ($\geq$ 800 K), molybdenum had a tendency to stay on/near the surface. This was also the case for procedure 2, where after simultaneous deposition of Mo and Ti, additional Ti was deposited on top. A real mixing of the two components was achieved with preparation procedure 3, where consecutive deposition of metals in UHV was followed by annealing at 700 K in $\sim 5 \times 10^{-7}$ mbar O_2. In that case, almost no Mo was observed at the surface. In procedures 4 and 5, only Mo was deposited onto the substrate at room temperature in O_2 and UHV environments, respectively. A post annealing treatment was applied in UHV in both cases. The relative amounts of Mo at the surface and in deeper layers were similar to the relative amounts obtained in procedures 1 and 2 for low Mo coverages. This clearly shows that Mo also tends to stay at the surface when co-deposited via procedures 1 and 2. Finally, with procedure 6, a separate cell designed for high-pressure experiments was used to generate the 50 mbar O_2 pressure needed to produce a layer of pure MoO_3 on the TiO_2, which was used mainly

as a reference for other experiments. This layer was predominantly corrugated but also possessed some flat, disordered regions.

The oxidation states of molybdenum were tracked using the Mo3d binding energies in XPS spectra. In almost all cases, the observed binding energies were compatible with Mo^{4+} or Mo^{6+}. In procedure 3, where Mo is mixed in TiO_2, the binding energy of Mo ($Mo3d_{5/2}$ = 229.35 eV) agreed well with Mo^{4+} in MoO_2 ($Mo3d_{5/2}$ = 229.3–229.5 eV). In the cases of procedures 1, 2 and 4, where Mo is concentrated near the surface, the dominant oxidation state was found to be 6+. The $Mo3d_{3/2}$ binding energies measured for Mo^{6+} (∼235.2 eV) were lower than the values in the literature for Mo^{6+} in MoO_3, and this was attributed to interaction with TiO_2. The other oxidation state of Mo in these layers was 4+. At low coverages of MoO_x, Mo^{6+} was dominant. As the coverage of MoO_x was increased, the amounts of Mo^{4+} and Mo^{6+} both increased. Whereas the Mo^{4+} signal intensity continued to grow with increasing coverage, the Mo^{6+} signal eventually plateaued, such that the signal intensities were equal at a MoO_2 coverage of about 0.5 ML. XPS revealed that the Mo^{6+} was nearer to the surface than the Mo^{4+}, consistent with the structure of a Mo^{6+} terminated MoO_2-like overlayer on TiO_2(110). The layers prepared according to procedure 5 consisted mostly of Mo^{4+}. In this case oxidation is a result of binding to lattice oxygen, which results in a concomitant redox reaction with Ti^{4+}. As such, Ti^{4+} is reduced upon Mo deposition but oxidizes back to Ti^{4+} when the layers are annealed in UHV at 670 K and above. Annealing in UHV also leads to the oxidation of Mo^{4+} to Mo^{6+}, via reduction of the TiO_2 substrate.

STM images of surfaces with a low MoO_x coverage revealed two types of features, which are not present in the images of clean TiO_2(110). One of the features (X1) is indicative of particles with apparent heights of ∼2.5 Å, which are centred over the 5cTi rows in the [001] direction and in between two 5cTi atoms in the $[1\bar{1}0]$ direction. The other feature (X2) is ∼1 Å high, has the shape of a bright square, and is centred on the bridging oxygen rows in the [001] direction and in between two bridging oxygen atoms in the $[1\bar{1}0]$ direction. X2 is more dominant at very low Mo concentrations (< 5%), whereas X1 becomes predominant above this concentration. No assignments were made to these features. At higher Mo concentrations, the layers were corrugated, and distinct features could not be identified. Nevertheless, a partial order was present despite the patchy appearance of the surfaces. Up to ∼50% Mo concentration, LEED patterns identical to those from TiO_2(110)–(1×1) were obtained from these surfaces. This observation was rationalized by assuming the presence of randomly occupied TiO_2(110) surface lattice sites. The corrugated structure was partly related to the sublimation of MoO_3 as the MoO_x domains grew thicker.

MoO_x layers with a low Mo concentration (∼5%) and prepared according to procedure 4 were stable in UHV up to at least 1000 K, and no agglomeration of the particles was observed in the STM images. The Mo mixed in TiO_2 (procedure 3) was also stable in UHV up to at least 900 K. The oxidation of MoO_x to MoO_3, and concomitant sublimation, was observed when mixed layers were annealed in O_2 at high temperatures (≥800 K). Mo loss was more prominent at high Mo concentrations and became slower as the concentration decreased. Sublimation was observed even when the layers were annealed in UHV, this time via oxidation with lattice oxygen.

Water TPD spectra of MoO_x containing surfaces indicated the blocking of BOVs with increasing Mo concentration. This observation was also verified by the STM images. In methanol TPD spectra of clean, UHV-annealed TiO_2(110), an unprecedented formaldehyde and methane formation pathway was observed at ∼650 K. This pathway, which requires methoxy formation at the BOVs, was suppressed as the MoO_x coverage increased and ceased to exist above ∼6% Mo concentration. At high Mo concentrations, the formation of methane was observed at ∼500 K. The well-established high-temperature (∼600 K) dehydrogenation pathway for ethanol was also suppressed with increasing MoO_x coverage due to blocking of the BOVs, and a new ethylene formation pathway was observed at ∼500 K. At low MoO_x concentrations, where Mo predominantly has the 6+ oxidation state, new molecular desorption features for water, methanol, and ethanol were noted at relatively low temperatures (200–250 K). Desorption features at higher temperatures (300–350 K) were observed for higher coverages, where Mo^{4+} was dominant.

To sum up, a number of different preparation procedures have been investigated in this work, which has centred on finding a useful recipe for the preparation of a Mo-doped TiO_2 model system. The prepared layers were characterized to provide a better understanding of the Mo–Ti mixed oxide system, even though most of them contained large amounts of Mo and suffered from segregation. The depositions carried out at high temperatures in O_2 were heavily influenced by two very important effects. The first is the oxidation of the TiO_2 substrate, which results in the formation of new layers via oxidation of Ti interstitials. The second one is oxidation of Mo to MoO_3, which then sublimes away. These two effects have to be taken seriously whenever a new recipe is tried. Furthermore, the limited solubility of MoO_2 in TiO_2 is also a critical issue. Mixing of these two phases is very limited below 1000 K, which means preparing an “atomically mixed” layer with more than ∼6% Mo content is always bound by thermodynamic restrictions. Apart from these issues, the layers with a low Mo concentration, prepared according to procedures 3 and 4 seem to be more promising than the others for further studies due to their homogeneity and thermal stability in UHV. Procedure 4 is suited for preparing layers that model TiO_2 supported MoO_x catalysts, whereas procedure 3 can be used to prepare mixed Mo+TiO_2 layers.

Symbols and Abbreviations

β (TPD)	heating rate
β (XPS)	angular asymmetry parameter
h	Planck's constant
$\hbar$	reduced Planck's constant ($h/2\pi$)
λ_e	electron wavelength
λ	inelastic mean free path of electrons in a solid
ν (TPD)	Arrhenius pre-exponential factor
ν (XPS)	frequency of light
ϕ	work function
ρ	electrical conductivity
σ	photoemission cross-section
σ_x	reflection operation in the x-direction
σ_y	reflection operation in the y-direction
ε	Hartree–Fock orbital energy
C_2	2-fold rotation operation
d_e	escape depth of electrons in a solid
E_{kin}	kinetic energy of photoelectron
E_{pass}	pass energy of the electron analyser
E_{ret}	retardation energy at the analyzer entrance
E_b	binding energy
E_d	activation energy of desorption
E_F	Fermi energy
F	photon flux
I_t	tunnelling current
I	photoelectron intensity
m_e	mass of electron
q_{st}	isosteric heat of adsorption
r_d	rate of desorption
R	ideal-gas constant
T	electron analyzer transmission function
5cTi	5-fold coordinated titanium atom
6cTi	6-fold coordinated titanium atom
2cO	2-fold coordinated oxygen atom
3cO	3-fold coordinated oxygen atom

BE	binding energy
BOV	bridging-oxygen vacancy
CSP	crystallographic shear plane
FO	frozen orbital
HF	Hartree–Fock
DFT	density functional theory
IMFP	inelastic mean free path
KT	Koopmans' theorem
LEED	low-energy electron diffraction
SPA–LEED	spot profile analysis LEED
STM	scanning tunnelling microscopy
TDS	thermal desorption spectroscopy
TPD	temperature programmed desorption
UHV	ultra-high vacuum
XPS	x-ray photoelectron spectroscopy

Appendix

Appendix A – Calculation of Mo Concentrations from XPS Spectra

The reported concentrations for Mo in the thesis are calculated from the Mo3d and Ti2p spectra of the corresponding surface. The assumptions below have been made:

1. The structure of the layer is homogeneous, irrespective of the actual structure.
2. All the XPS signals are coming from this homogeneously mixed layer. No signal is coming from the substrate (which is clearly non-factual in many cases).
3. The IMFP (λ) of the photoelectrons in the layer are equal to their IMFP in pure TiO_2

The above assumptions mean that we are calculating the Mo concentration in a hypothetical homogeneously-mixed layer which is thick enough that no signal is coming from the substrate.

The transmission function of the analyser is assumed to have the form:

$$T \propto E_{kin}^{-0.7} \tag{6.1}$$

Kinetic energies are calculated by subtracting the average binding energies ($E_{b,Ti2p} =$ 470 eV, $E_{b,Mo3d} = 230$ eV) and the analyser work function ($\phi_a = 4.8$ eV) from the photon energy. The ratio of the transmission of the Mo3d to Ti2p photoelectrons is then:

$$\frac{T_{Mo3d}}{T_{Ti2p}} = \left(\frac{1486.6 - 230 - 4.8}{1486.6 - 470 - 4.8}\right)^{-0.7} = 0.862 \tag{6.2}$$

The ionisation cross-sections of Mo and Ti for 1486.6 eV photon energy (Al Kα) are obtained from Yeh and Lindau:

$$\sigma_{Mo3d}(1486.6 \text{ eV}) = 0.130 \text{ Mb}$$

$$\sigma_{Ti2p}(1486.6 \text{ eV}) = 0.107 \text{ Mb}$$

The IMFP of the Ti2p and Mo3d photoelectrons in TiO_2 depend on their kinetic energies. The values are calculated from the TPP2M formula using the free software developed by Sven Tougaard.

$$\lambda_{Mo3d}(1486.6 \text{ eV}) = 24.8 \text{ Å}$$

$$\lambda_{Ti2p}(1486.6 \text{ eV}) = 21.2 \text{ Å}$$

Equation 2.15 can be integrated since n_i was assumed to be independent of the position in the layer. This gives the photoelectron intensity for Mo3d and Ti2p as:

$$I_{Mo3d} = F\ T_{Mo3d}\ \sigma_{Mo3d}\ n_{Mo}\ \lambda_{Mo3d}\ \cos\theta \tag{6.3}$$

$$I_{Ti2p} = F\ T_{Ti2p}\ \sigma_{Ti2p}\ n_{Ti}\ \lambda_{Ti2p}\ \cos\theta \tag{6.4}$$

The ratios of the signals are relevant for relative quantification, which is:

$$\frac{I_{Mo3d}}{I_{Ti2p}} = \frac{T_{Mo3d}}{T_{Ti2p}}\ \frac{\sigma_{Mo3d}}{\sigma_{Ti2p}}\ \frac{n_{Mo}}{n_{Ti}}\ \frac{\lambda_{Mo3d}}{\lambda_{Ti2p}} \tag{6.5}$$

$$= 0.862\ \frac{0.130}{0.107}\ \frac{n_{Mo}}{n_{Ti}}\ \frac{24.8}{21.2} \tag{6.6}$$

When the intensities of the Mo3d and Ti2p signals are known, the last relationship can be used to calculate the ratio of the molybdenum concentration to titanium concentration.

$$\frac{n_{Mo}}{n_{Ti}} = 0.82\ \frac{I_{Mo3d}}{I_{Ti2p}} \tag{6.7}$$

The reported concentrations in the text are always the percentage of molybdenum in all the metal atoms, which is simply:

$$\frac{n_{Mo}}{n_{Mo} + n_{Ti}} \times 100 \tag{6.8}$$

Appendix B – Calculation of the Equilibrium Pressure of Oxygen in the $Mo/MoO_2/MoO_3$ System

In the case of chemical equilibrium between molybdenum and oxygen, these two reactions have been taken into account:

$$\mathrm{Mo(s)} + \mathrm{O_2(g)} \rightleftharpoons \mathrm{MoO_2(s)} \quad (1)$$

$$2\,\mathrm{MoO_2(s)} + \mathrm{O_2(g)} \rightleftharpoons 2\,\mathrm{MoO_3(s)} \quad (2)$$

In chemical equilibrium, the equilibrium constants of reactions 1 and 2 can be expressed as:

$$K_{eq,1} = \frac{a_{\mathrm{MoO_2}}}{a_{\mathrm{Mo}}\, a_{\mathrm{O_2}}} \tag{6.9}$$

$$K_{eq,2} = \frac{(a_{\mathrm{MoO_3}})^2}{(a_{\mathrm{MoO_2}})^2\, a_{\mathrm{O_2}}} \tag{6.10}$$

where a_i is the activity of chemical species i and it is defined as:

$$a_i = \exp\left(\frac{G_i - G_i^\circ}{RT}\right) \tag{6.11}$$

G_i and G_i° are the Gibbs energies at the state that we are interested in (T, P) and the standard state (T, P°) respectively. $a_i \approx P_i/P_i^\circ = P_i/(1\ \mathrm{bar})$ for pure gases with nearly ideal behaviour and $a_i \approx 1$ for solids at low to moderate pressures. These substituted into equations 6.9 and 6.10 give:

$$K_{eq,1} = \frac{1}{P_{\mathrm{O_2}}/(1\ \mathrm{bar})} \tag{6.12}$$

$$K_{eq,2} = \frac{1}{P_{\mathrm{O_2}}/(1\ \mathrm{bar})} \tag{6.13}$$

The equilibrium constants can be calculated from the reaction Gibbs energy change according to the relation:

$$K_{eq} = \exp\left(\frac{-\Delta_r G^\circ(T)}{RT}\right) \tag{6.14}$$

The term $\Delta_r G^\circ$ must be calculated with the given stoichiometric coefficients in reactions

1 and 2 in order for the equations 6.12 and 6.13 to be valid.

$$\Delta_{r,1}G^\circ = G^\circ_{\mathrm{MoO_2(s)}^\circ} - G^\circ_{\mathrm{Mo(s)}} - G^\circ_{\mathrm{O_2(g)}} \tag{6.15}$$

$$\Delta_{r,2}G^\circ = 2G^\circ_{\mathrm{MoO_3(s)}} - 2G^\circ_{\mathrm{MoO_2(s)}} - G^\circ_{\mathrm{O_2(g)}} \tag{6.16}$$

Standard enthalpies and entropies for Mo, MoO_2, MoO_3 and O_2 are given by Chase [85] and are also available via NIST Chemistry WebBook (`http://webbook.nist.gov/chemistry/`). Equations 6.17 and 6.18 are the formulas for H° and S°, where $t = T/(1000\ \mathrm{K})$ and the coefficients A–H are tabulated in the reference. Gibbs energies can be calculated from these values using the definition $G \equiv H - TS$.

$$H^\circ - H^\circ_{298.15} = At + B\frac{t^2}{2} + C\frac{t^3}{3} + D\frac{t^4}{4} - \frac{E}{t} + F - H \tag{6.17}$$

$$S^\circ = A\ln(t) + Bt + C\frac{t^2}{2} + D\frac{t^3}{3} - \frac{E}{2t^2} + G \tag{6.18}$$

$$G^\circ = (H^\circ - H^\circ_{298.15}) - TS^\circ \tag{6.19}$$

Calculating Gibbs energies the components at different temperatures using equations 6.17–6.19, one can obtain $\Delta_{r,1}G^\circ$ and $\Delta_{r,2}G^\circ$ as a function of temperature. Using equations 6.12 and 6.13, the equilibrium pressure of oxygen can be calculated at different temperatures, as it was done in Figure 3.8.

Appendix C – Peak Fitting in XPS

The approximation to the Voigt function was made using with the following normalized functions for Gaussian (G) and Lorentzian (L) peak shapes:

$$G(x : E, F, m) = \exp\left(-4(\ln 2)(1-m)\left(\frac{x-E}{F}\right)^2\right) \tag{6.20}$$

$$L(x : E, F, m) = \left(1 + 4m\left(\frac{x-E}{F}\right)^2\right)^{-1} \tag{6.21}$$

where E is the binding energy at peak maximum, F is the full width at half maximum (FWHM) and m ($0 \leq m \leq 1$) is the weighting factor for Lorentzian contribution. The Voigt function approximation was made by multiplying the two contributions:

$$GL(x : E, F, m) = G(x : E, F, m)L(x : E, F, m) \tag{6.22}$$

Mo3d lines in the XPS spectra of Mo^{4+} species are asymmetric. The functions which were used for the fitting of these lines were given an asymmetric shape by the modifying function (T):

$$T(x : E, F, k) = \begin{cases} \exp\left(-k\left(\frac{x-E}{F}\right)\right) & \text{if } x \geq E, \\ 0 & \text{if } x < E. \end{cases} \tag{6.23}$$

The final form of the asymmetric profile is:

$$GLT(x : E, F, m, k) = GL(x : E, F, m) + T(x : E, F, k)\,(1 - GL(x : E, F, m)) \tag{6.24}$$

Bibliography

[1] Dingedissen, U.; Martin, A.; Herein, D.; and Wernicke, H. J. *Handbook of Heterogeneous Catalysis*, chapter The Development of Industrial Heterogeneous Catalysis. Wiley-VCH Verlag GmbH & Co. KGaA, 2008. pages 37–56

[2] Hatscher, S. T.; Fetzer, T.; Wagner, E.; and Kneuper, H.-J. *Handbook of Heterogeneous Catalysis*, chapter Ammonia Oxidation. Wiley-VCH Verlag GmbH & Co. KGaA, 2008. pages 2575–2592

[3] Moser, M. D. and Bogdan, P. L. *Handbook of Heterogeneous Catalysis*, chapter Catalytic Reforming. Wiley-VCH Verlag GmbH & Co. KGaA, 2008. pages 2728–2743

[4] Caspary, K. J.; Gehrke, H.; Heinritz-Adrian, M.; and Schwefer, M. *Handbook of Heterogeneous Catalysis*, chapter Dehydrogenation of Alkanes. Wiley-VCH Verlag GmbH & Co. KGaA, 2008

[5] Haber, J. *Handbook of Heterogeneous Catalysis*, chapter Selective Oxidations. Wiley-VCH Verlag GmbH & Co. KGaA, 2008. pages 3359–3384

[6] Håkonsen, S. F. and Holmen, A. *Handbook of Heterogeneous Catalysis*, chapter Oxidative Dehydrogenation of Alkanes. Wiley-VCH Verlag GmbH & Co. KGaA, 2008

[7] Kim, H. Y.; Lee, H. M.; Pala, R. G. S.; Shapovalov, V.; and Metiu, H. *Journal of Physical Chemistry C* **112(32)**:(2008) 12398–12408

[8] Garcia-Mota, M.; Vojvodic, A.; Metiu, H.; Man, I. C.; Su, H. Y.; Rossmeisl, J.; and Norskov, J. K. *Chemcatchem* **3(10)**:(2011) 1607–1611

[9] Hu, Z. and Metiu, H. *The Journal of Physical Chemistry C* **115**:(2011) 17898–17909

[10] Hu, Z.; Li, B.; Sun, X. Y.; and Metiu, H. *The Journal of Physical Chemistry C* **115**:(2011) 3065–3074

[11] Andersin, J.; Nevalaita, J.; Honkala, K.; and Häkkinen, H. *Angewandte Chemie, International Edition* **52**:(2013) 1424–1427

[12] Metiu, H.; Chrétien, S.; Hu, Z.; Li, B.; and Sun, X. *The Journal of Physical Chemistry C* **116(19)**:(2012) 10439–10450

[13] McFarland, E. and Metiu, H. *Chemical Reviews* **xx**:(2013) xx

[14] Jerratsch, J. F.; Nilius, N.; Freund, H.-J.; Martinez, U.; Giordano, L.; and Pacchioni, G. *Phys. Rev. B* **80**:(2009) 245423

[15] Myrach, P.; Nilius, N.; Levchenko, S. V.; Gonchar, A.; Risse, T.; Dinse, K. P.; Boatner, L. A.; Frandsen, W.; Horn, R.; Freund, H. J.; Schlogl, R.; and Scheffler, M. *Chemcatchem* **2(7)**:(2010) 854–862

[16] Shao, X.; Prada, S.; Giordano, L.; Pacchioni, G.; Nilius, N.; and Freund, H.-J. *Angewandte Chemie International Edition* **50(48)**:(2011) 11525–11527. ISSN 1521-3773

[17] Stavale, F.; Shao, X.; Nilius, N.; Freund, H.-J.; Prada, S.; Giordano, L.; and Pacchioni, G. *Journal of the American Chemical Society* **134(28)**:(2012) 11380–11383

[18] Stavale, F.; Nilius, N.; and Freund, H.-J. *New Journal of Physics* **14(3)**:(2012) 033006

[19] Shao, X.; Nilius, N.; and Freund, H.-J. *Journal of the American Chemical Society* **134(5)**:(2012) 2532–2534

[20] Diebold, U. *Surface Science Reports* **48(5-8)**:(2003) 53–229

[21] McCarty, K. F. *Surface Science* **543(1-3)**:(2003) 185–206

[22] Lenard, P. *Annalen der Physik* **307(6)**:(1900) 359–375

[23] Lenard, P. *Annalen der Physik* **313(5)**:(1902) 149–198

[24] Einstein, A. *Annalen der Physik* **322(6)**:(1905) 132–148

[25] `http://www.fhi-berlin.mpg.de/acnew/groups/electronicstructure/pages/methods.html`. High Pressure XPS at FHI [Online; accessed 09-February-2013]

[26] `http://stm.lbl.gov/Salmeron_group/lab5.html`. High Pressure XPS at Berkeley [Online; accessed 09-February-2013]

[27] Jackson, S. and Hargreaves, J. *Metal Oxide Catalysis*. Wiley, 2008

[28] Lüth, H. *Solid Surfaces, Interfaces and Thin Films*. Springer-Verlag, 2010

[29] Cooper, J. and Zare, R. N. *Journal of Chemical Physics* **48(2)**:(1968) 942–&

[30] Jacobs, V. L. *Journal of Physics B-Atomic Molecular and Optical Physics* **5(12)**:(1972) 2257–2271

[31] Yeh, J. J. and Lindau, I. *Atomic Data and Nuclear Data Tables* **32(1)**:(1985) 1–155

[32] Scofield, J. H. *Journal of Electron Spectroscopy and Related Phenomena* **8(2)**:(1976) 129–137

[33] Vickerman, J. and Gilmore, I. *Surface Analysis: The Principal Techniques*. Wiley, 2009

[34] Van Hove, M. and Tong, S. *Surface Crystallography by LEED: Theory, Computation and Structural Results*. Springer London, Limited, 2011

[35] Atkins, P. W. *Molecular quantum mechanics*. Oxford University Press, Oxford, 2nd ed. edition, 1983

[36] Tersoff, J. and Hamann, D. R. *Physical Review B* **31(2)**:(1985) 805–813

[37] King, D. A. *Surface Science* **47(1)**:(1975) 384–402

[38] Redhead, P. A. *Vacuum* **12(4)**:(1962) 203–211

[39] Habenschaden, E. and Kuppers, J. *Surface Science* **138(1)**:(1984) L147–L150

[40] Okamoto, H. *Journal of Phase Equilibria and Diffusion* **32(5)**:(2011) 473–474

[41] Henrich, V. E. and Cox, P. *The Surface Science of Metal Oxides*. Cambridge University Press, 1996

[42] Shriver, D. and Atkins, P. *Inorganic Chemistry*. W. H. Freeman, 2006

[43] Smart, L. and Moore, E. *Solid State Chemistry: An Introduction, Third Edition*. Taylor & Francis, 2005

[44] West, A. *Basic solid state chemistry*. John Wiley & Sons, 1999

[45] Andersson, S.; Collen, B.; Kuylenstierna, U.; and Magneli, A. *Acta Chemica Scandinavica* **11(10)**:(1957) 1641–1652

[46] Murray, J. L. and Wriedt, H. A. *Journal of Phase Equilibria* **8(2)**:(1987) 148–165

[47] Zhang, H. Z. and Banfield, J. F. *Journal of Materials Chemistry* **8(9)**:(1998) 2073–2076

[48] Reyes-Coronado, D.; Rodriguez-Gattorno, G.; Espinosa-Pesqueira, M. E.; Cab, C.; de Coss, R.; and Oskam, G. *Nanotechnology* **19(14)**:(2008) 145605

[49] Gabrielsson, P. and Pedersen, H. G. *Handbook of Heterogeneous Catalysis*, chapter Flue Gases from Stationary Sources. Wiley-VCH Verlag GmbH & Co. KGaA, 2008

[50] Rosowski, F.; Storck, S.; and Zühlke, J. *Handbook of Heterogeneous Catalysis*, chapter Oxyfunctionalization of Alkyl Aromatics. Wiley-VCH Verlag GmbH & Co. KGaA, 2008

[51] Fujishima, A.; Rao, T. N.; and Tryk, D. A. *Journal of Photochemistry and Photobiology C: Photochemistry Reviews* **1(1)**:(2000) 1–21

[52] Carp, O.; Huisman, C. L.; and Reller, A. *Progress in Solid State Chemistry* **32(1-2)**:(2004) 33–177

[53] Takeuchi, M.; Kitano, M.; Matsuoka, M.; and Anpo, M. *Handbook of Heterogeneous Catalysis*, chapter Photocatalysis: Development of Highly Functional Titanium Oxide Photocatalysts. Wiley-VCH Verlag GmbH & Co. KGaA, 2008

[54] Oregan, B. and Gratzel, M. *Nature* **353(6346)**:(1991) 737–740

[55] Gratzel, M. *Journal of Photochemistry and Photobiology C-Photochemistry Reviews* **4(2)**:(2003) 145–153

[56] Su, R.; Bechstein, R.; So, L.; Vang, R. T.; Sillassen, M.; Esbjornsson, B.; Palmqvist, A.; and Besenbacher, F. *Journal of Physical Chemistry C* **115(49)**:(2011) 24287–24292

[57] Waldner, P. and Eriksson, G. *Calphad-Computer Coupling of Phase Diagrams and Thermochemistry* **23(2)**:(1999) 189–218

[58] He, J.; Behera, R. K.; Finnis, M. W.; Li, X.; Dickey, E. C.; Phillpot, S. R.; and Sinnott, S. B. *Acta Materialia* **55(13)**:(2007) 4325–4337

[59] Seebauer, E. and Kratzer, M. *Charged Semiconductor Defects*. Springer London, 2009

[60] Henderson, M. A. *Surface Science* **343(1-2)**:(1995) L1156–L1160

[61] Onishi, H. and Iwasawa, Y. *Physical Review Letters* **76(5)**:(1996) 791–794

[62] Li, M.; Hebenstreit, W.; and Diebold, U. *Surface Science* **414(1-2)**:(1998) L951–L956

[63] Li, M.; Hebenstreit, W.; Gross, L.; Diebold, U.; Henderson, M. A.; Jennison, D. R.; Schultz, P. A.; and Sears, M. P. *Surface Science* **437(1-2)**:(1999) 173–190

[64] Cabailh, G.; Torrelles, X.; Lindsay, R.; Bikondoa, O.; Joumard, I.; Zegenhagen, J.; and Thornton, G. *Physical Review B* **75(24)**:(2007) 241403

[65] Lindsay, R.; Wander, A.; Ernst, A.; Montanari, B.; Thornton, G.; and Harrison, N. M. *Physical Review Letters* **94(24)**:(2005) 246102

[66] Wendt, S.; Schaub, R.; Matthiesen, J.; Vestergaard, E. K.; Wahlstrom, E.; Rasmussen, M. D.; Thostrup, P.; Molina, L. M.; Laegsgaard, E.; Stensgaard, I.; Hammer, B.; and Besenbacher, F. *Surface Science* **598(1-3)**:(2005) 226–245

[67] Hugenschmidt, M. B.; Gamble, L.; and Campbell, C. T. *Surface Science* **302(3)**:(1994) 329–340

[68] Schaub, R.; Thostrup, P.; Lopez, N.; Laegsgaard, E.; Stensgaard, I.; Norskov, J. K.; and Besenbacher, F. *Physical Review Letters* **87(26)**:(2001) 266104

[69] Bikondoa, O.; Pang, C. L.; Ithnin, R.; Muryn, C. A.; Onishi, H.; and Thornton, G. *Nature Materials* **5(3)**:(2006) 189–192

[70] Moulder, J. F.; Stickle, W. F.; Sobol, P. E.; and Bomben, K. D. *Handbook of X-ray Photoelectron Spectroscopy*. Perkin-Elmer Corporation, Minnesota, USA, 1992

[71] Brewer, L. and Lamoreaux, R. H. *Bulletin of Alloy Phase Diagrams* **1(2)**:(1980) 85–89

[72] Bygden, J.; Sichen, D.; and Seetharaman, S. *Metallurgical and Materials Transactions B-Process Metallurgy and Materials Processing Science* **25(6)**:(1994) 885–891

[73] Brandt, B. G. and Skapski, A. C. *Acta Chemica Scandinavica* **21(3)**:(1967) 661–&

[74] Eyert, V.; Horny, R.; Hock, K. H.; and Horn, S. *Journal of Physics-Condensed Matter* **12(23)**:(2000) 4923–4946

[75] Bolzan, A. A.; Kennedy, B. J.; and Howard, C. J. *Australian Journal of Chemistry* **48(8)**:(1995) 1473–1477

[76] Brakken, H. *Zeitschrift Fur Kristallographie* **78(5/6)**:(1931) 484–488

[77] Wooster, N. *Zeitschrift Fur Kristallographie* **80(5/6)**:(1931) 504–512

[78] Andersson, G. and Magneli, A. *Acta Chemica Scandinavica* **4(5)**:(1950) 793–797

[79] Song, Z.; Cai, T. H.; Chang, Z. P.; Liu, G.; Rodriguez, J. A.; and Hrbek, J. *Journal of the American Chemical Society* **125(26)**:(2003) 8059–8066

[80] Biener, M. M.; Biener, J.; Schalek, R.; and Friend, C. M. *Journal of Chemical Physics* **121(23)**:(2004) 12010–12016

[81] Biener, M. M. and Friend, C. M. *Surface Science* **559(2-3)**:(2004) L173–L179

[82] Quek, S. Y.; Biener, M. M.; Biener, J.; Friend, C. M.; and Kaxiras, E. *Surface Science* **577(2-3)**:(2005) L71–L77

[83] Deng, X.; Quek, S. Y.; Biener, M. M.; Biener, J.; Kang, D. H.; Schalek, R.; Kaxiras, E.; and Friend, C. M. *Surface Science* **602(6)**:(2008) 1166–1174

[84] Sitepu, H. *Powder Diffraction* **24(4)**:(2009) 315–326

[85] Chase, M. W.; of Standards, N. I.; and (U.S.), T. *NIST-JANAF Thermochemical Tables*. Journal of Physical and Chemical Reference Data Monograph. American Chemical Society; American Institute of Physics for the National Institute of Standards and Technology, Washington, D.C., 4th edition, 1998

[86] Guimond, S. *Vanadium and Molybdenum Oxide Thin Films on Au(111): Growth and Surface Characterization*. Ph.D. thesis, Humboldt University Berlin, 2009

[87] Dai, W. and Ren, L. *Handbook of Heterogeneous Catalysis*, chapter Dehydrogenation of Alcohols: Formaldehyde. Wiley-VCH Verlag GmbH & Co. KGaA, 2008

[88] Routray, K.; Zhou, W.; Kiely, C. J.; Grunert, W.; and Wachs, I. E. *Journal of Catalysis* **275(1)**:(2010) 84–98

[89] Mol, J. C. and van Leeuwen, P. W. N. M. *Handbook of Heterogeneous Catalysis*, chapter Metathesis of Alkenes. Wiley-VCH Verlag GmbH & Co. KGaA, 2008

[90] Grasselli, R. K. and Burrington, J. D. *Handbook of Heterogeneous Catalysis*, chapter Oxidation of Low-Molecular-Weight Hydrocarbons. Wiley-VCH Verlag GmbH & Co. KGaA, 2008

[91] Grasselli, R. K.; Trifiró, F.; and Forni, L. *Handbook of Heterogeneous Catalysis*, chapter Ammoximation. Wiley-VCH Verlag GmbH & Co. KGaA, 2008

[92] Marinder, B. O. and Magneli, A. *Acta Chemica Scandinavica* **12(6)**:(1958) 1345–1347

[93] Jacob, K. T.; Shekhar, C.; and Waseday, Y. *Journal of the American Ceramic Society* **91(2)**:(2008) 563–568

[94] Ferroni, M.; Guidi, V.; Martinelli, G.; Roncarati, G.; Comini, E.; Sberveglieri, G.; Vomiero, A.; and Mea, G. D. *Journal of Vacuum Science & Technology B* **20(2)**:(2002) 523–530

[95] Simon, U.; Arndt, S.; Otremba, T.; Schlingmann, T.; Gorke, O.; Dinse, K. P.; Schomacker, R.; and Schubert, H. *Catalysis Communications* **18**:(2012) 132–136

[96] Zavyalova, U.; Geske, M.; Horn, R.; Weinberg, G.; Frandsen, W.; Schuster, M.; and Schlogl, R. *Chemcatchem* **3(6)**:(2011) 949–959

[97] Arndt, S.; Laugel, G.; Levchenko, S.; Horn, R.; Baerns, M.; Scheffler, M.; Schlogl, R.; and Schomacker, R. *Catalysis Reviews-Science and Engineering* **53(4)**:(2011) 424–514

[98] Lian, J. C.; Finazzi, E.; Di Valentin, C.; Risse, T.; Gao, H. J.; Pacchioni, G.; and Freund, H. J. *Chemical Physics Letters* **450(4-6)**:(2008) 308–311

[99] Kuo, Y.; Behrendt, F.; and Lerch, M. *Zeitschrift Fur Physikalische Chemie-International Journal of Research in Physical Chemistry & Chemical Physics* **221(8)**:(2007) 1017–1037

[100] Trionfetti, C.; Babich, I. V.; Seshan, K.; and Lefferts, L. *Applied Catalysis A-General* **310**:(2006) 105–113

[101] Shapovalov, V.; Fievez, T.; and Bell, A. T. *Journal of Physical Chemistry C* **116(35)**:(2012) 18728–18735

[102] Price, S. P.; Tong, X.; Ridge, C.; Shapovalov, V.; Hu, Z. P.; Kemper, P.; Metiu, H.; Bowers, M. T.; and Buratto, S. K. *Surface Science* **605(9-10)**:(2011) 972–976

[103] Gonzalez-Navarrete, P.; Gracia, L.; Calatayud, M.; and Andres, J. *Journal of Physical Chemistry C* **114(13)**:(2010) 6039–6046

[104] Jorgensen, B.; Kristensen, S. B.; Kunov-Kruse, A. J.; Fehrmann, R.; Christensen, C. H.; and Riisager, A. *Topics in Catalysis* **52(3)**:(2009) 253–257

[105] Vittadini, A.; Casarin, M.; and Selloni, A. *Journal of Physical Chemistry B* **109(5)**:(2005) 1652–1655

[106] Wang, Q. G. and Madix, R. J. *Surface Science* **496(1-2)**:(2002) 51–63

[107] Roduit, B.; Wokaun, A.; and Baiker, A. *Industrial & Engineering Chemistry Research* **37(12)**:(1998) 4577–4590

[108] Dumesic, J. A.; Topsoe, N. Y.; Topsoe, H.; Chen, Y.; and Slabiak, T. *Journal of Catalysis* **163(2)**:(1996) 409–417

[109] Topsoe, N. Y.; Dumesic, J. A.; and Topsoe, H. *Journal of Catalysis* **151(1)**:(1995) 241–252

[110] Haber, J.; Machej, T.; Serwicka, E. M.; and Wachs, I. E. *Catalysis Letters* **32(1-2)**:(1995) 101–114

[111] Topsoe, N. Y.; Dumesic, J. A.; and Topsoe, H. *Abstracts of Papers of the American Chemical Society* **207**:(1994) 10–PETR

[112] Uhlrich, J. J.; Sainio, J.; Lei, Y.; Edwards, D.; Davies, R.; Bowker, M.; Shaikhutdinov, S.; and Freund, H. J. *Surface Science* **605(15-16)**:(2011) 1550–1555

[113] O'Brien, M. G.; Beale, A. M.; Jacques, S. D. M.; and Weckhuysen, B. M. *Topics in Catalysis* **52(10)**:(2009) 1400–1409

[114] House, M. P.; Shannon, M. D.; and Bowker, M. *Catalysis Letters* **122(3-4)**:(2008) 210–213

[115] Domenichini, B.; Rizzi, G. A.; Kruger, P.; Della Negra, M.; Li, Z. S.; Petukhov, M.; Granozzi, G.; Moller, P. J.; and Bourgeois, S. *Physical Review B* **73(24)**:(2006) 245433

[116] Brox, B. and Olefjord, I. *Surface and Interface Analysis* **13(1)**:(1988) 3–6

[117] Scanlon, D. O.; Watson, G. W.; Payne, D. J.; Atkinson, G. R.; Egdell, R. G.; and Law, D. S. L. *Journal of Physical Chemistry C* **114(10)**:(2010) 4636–4645

[118] Grunert, W.; Stakheev, A. Y.; Feldhaus, R.; Anders, K.; Shpiro, E. S.; and Minachev, K. M. *Journal of Physical Chemistry* **95(3)**:(1991) 1323–1328

[119] Ozkar, S.; Ozin, G. A.; and Prokopowicz, R. A. *Chemistry of Materials* **4(6)**:(1992) 1380–1388

[120] Fleisch, T. H. and Mains, G. J. *Journal of Chemical Physics* **76(2)**:(1982) 780–786

[121] Yamada, M.; Yasumaru, J.; Houalla, M.; and Hercules, D. M. *Journal of Physical Chemistry* **95(18)**:(1991) 7037–7042

[122] Spevack, P. A. and Mcintyre, N. S. *Journal of Physical Chemistry* **96(22)**:(1992) 9029–9035

[123] Berkowitz, J.; Inghram, M. G.; and Chupka, W. A. *Journal of Chemical Physics* **26(4)**:(1957) 842–846

[124] Bertolini, J. C.; Massardier, J.; Delichere, P.; Tardy, B.; Imelik, B.; Jugnet, Y.; Duc, T. M.; Detemmerman, L.; Creemers, C.; Vanhove, H.; and Neyens, A. *Surface Science* **119(1)**:(1982) 95–106

[125] Gauthier, Y.; Joly, Y.; Baudoing, R.; and Rundgren, J. *Physical Review B* **31(10)**:(1985) 6216–6218

[126] Baudoing, R.; Gauthier, Y.; Lundberg, M.; and Rundgren, J. *Journal of Physics C-Solid State Physics* **19(16)**:(1986) 2825–2831

[127] Gauthier, Y.; Hoffmann, W.; and Wuttig, M. *Surface Science* **233(3)**:(1990) 239–247

[128] Heinz, K.; Doll, R.; and Kottcke, M. *Surface Review and Letters* **3(5-6)**:(1996) 1651–1661

[129] Gauthier, Y.; Baudoing-Savois, R.; Bugnard, J. M.; Hebenstreit, W.; Schmid, M.; and Varga, P. *Surface Science* **466(1-3)**:(2000) 155–166

[130] Domenichini, B.; Flank, A. M.; Lagarde, P.; and Bourgeois, S. *Surface Science* **560(1-3)**:(2004) 63–78

[131] Onishi, H. and Iwasawa, Y. *Surface Science* **357(1-3)**:(1996) 773–776

[132] Werfel, F. and Minni, E. *Journal of Physics C-Solid State Physics* **16(31)**:(1983) 6091–6100

[133] Beatham, N.; Cox, P. A.; Egdell, R. G.; and Orchard, A. F. *Chemical Physics Letters* **69(3)**:(1980) 479–482

[134] Campagna, M.; Wertheim, G. K.; Shanks, H. R.; Zumsteg, F.; and Banks, E. *Physical Review Letters* **34(12)**:(1975) 738–741

[135] Chazalviel, J. N.; Campagna, M.; Wertheim, G. K.; and Shanks, H. R. *Physical Review B* **16(2)**:(1977) 697–705

[136] Wertheim, G. K. *Chemical Physics Letters* **65(2)**:(1979) 377–379

[137] Egdell, R. G.; Innes, H.; and Hill, M. D. *Surface Science* **149(1)**:(1985) 33–47

[138] Chun, W. J.; Asakura, K.; and Iwasawa, Y. *Journal of Physical Chemistry B* **102(45)**:(1998) 9006–9014

[139] Li, Z. J.; Smith, R. S.; Kay, B. D.; and Dohnalek, Z. *Journal of Physical Chemistry C* **115(45)**:(2011) 22534–22539

[140] Asaduzzaman, A. M. and Kruger, P. *Physical Review B* **76(11)**:(2007) 115412

[141] Ervin, K. M. and DeTuro, V. F. *Journal of Physical Chemistry A* **106(42)**:(2002) 9947–9956

[142] Ruscic, B. and Berkowitz, J. *Journal of Physical Chemistry* **97(44)**:(1993) 11451–11455

[143] Ruscic, B. and Berkowitz, J. *Journal of Chemical Physics* **101(12)**:(1994) 10936–10946

[144] Blanksby, S. J. and Ellison, G. B. *Accounts of Chemical Research* **36(4)**:(2003) 255–263

[145] Henderson, M. A. *Surface Science* **355(1-3)**:(1996) 151–166

[146] Henderson, M. A. *Langmuir* **12(21)**:(1996) 5093–5098

[147] Henderson, M. A.; Otero-Tapia, S.; and Castro, M. E. *Faraday Discussions* **114**:(1999) 313–329

[148] Henderson, M. A. *Surface Science* **400(1-3)**:(1998) 203–219

[149] Henderson, M. A. *Surface Science Reports* **46(1-8)**:(2002) 1–308

[150] Bondarchuk, O.; Kim, Y. K.; White, J. M.; Kim, J.; Kay, B. D.; and Dohnalek, Z. *Journal of Physical Chemistry C* **111(29)**:(2007) 11059–11067

[151] Suzuki, S.; Fukui, K.; Onishi, H.; Sasaki, T.; and Iwasawa, Y. *Observation of Individual Adsorbed Pyridine, Ammonia, and Water on TiO_2(110) by Means of Scanning Tunneling Microscopy*, volume 132. Elsevier, 2001. pages 753–756

[152] Martinez, U.; Vilhelmsen, L. B.; Kristoffersen, H. H.; Stausholm-Moller, J.; and Hammer, B. *Physical Review B* **84(20)**:(2011) 205434

[153] Thompson, T. L.; Diwald, O.; and Yates, J. T. *Journal of Physical Chemistry B* **107(42)**:(2003) 11700–11704

[154] Henry, R. M.; Walker, B. W.; and Stair, P. C. *Surface Science* **155(2-3)**:(1985) 732–750

[155] Yin, X. L.; Han, H. M.; and Miyamoto, A. *Journal of Molecular Modeling* **7(7)**:(2001) 207–215

[156] Kuhlenbeck, H. and Freund, H. J. *Adsorption on Oxide Surfaces*, chapter 3.9. Numerical Data and Functional Relationships in Science and Technology. Springer-Verlag, 2006. page 332

[157] Thiel, P. A. and Madey, T. E. *Surface Science Reports* **7(6-8)**:(1987) 211–385

[158] Hwu, H. H. and Chen, J. G. *Surface Science* **536(1-3)**:(2003) 75–87

[159] Chen, D. A. and Friend, C. M. *Journal of the American Chemical Society* **120(20)**:(1998) 5017–5023

[160] Queeney, K. T. and Friend, C. M. *Journal of Chemical Physics* **109(14)**:(1998) 6067–6074

[161] Queeney, K. T. and Friend, C. M. *Journal of Physical Chemistry B* **102(26)**:(1998) 5178–5181

[162] Farfan-Arribas, E. and Madix, R. J. *Surface Science* **544(2-3)**:(2003) 241–260

[163] Ko, E. I. and Madix, R. J. *Surface Science* **112(3)**:(1981) 373–385

[164] Street, S. C.; Liu, G.; and Goodman, D. W. *Surface Science* **385(2-3)**:(1997) L971–L977

[165] Kim, H. Y.; Lee, H. M.; Pala, R. G. S.; and Metiu, H. *Journal of Physical Chemistry C* **113(36)**:(2009) 16083–16093

[166] Kim, Y. K.; Kay, B. D.; White, J. M.; and Dohnalek, Z. *Journal of Physical Chemistry C* **111(49)**:(2007) 18236–18242

List of Figures

List of Tables

Selbständigkeitserklärung

Ich erkläre, dass ich die vorliegende Arbeit selbständig und nur unter Verwendung der angegebenen Literatur und Hilfsmittel angefertigt habe.

Berlin, den 28.3.2013 Osman Karslıoğlu